ROCKING RESPONSE OF SLENDER FREESTANDING BUILDING CONTENTS

ROCKING RESPONSE OF SLENDER FREESTANDING BUILDING CONTENTS IN FIXED-BASE AND BASE-ISOLATED BUILDINGS

By SCOTT LINDE, B.Eng.

A Thesis Submitted to the School of Graduate Studies in Partial Fulfilment of the Requirements for the Degree of Master of Applied Science

Master of Applied Science (2016)
(Civil Engineering)

McMaster University
Hamilton, Ontario, Canada

TITLE:	Rocking Response of Slender Freestanding Building Contents in Fixed-Base and Base-Isolated Buildings
AUTHOR:	Scott Linde
SUPERVISORS:	Dr. Dimitrios Konstantinidis, Dr. Michael Tait
NUMBER OF PAGES:	123 pages (xvii, 106)

Lay Summary

During an earthquake slender building contents respond by rocking about their edges. Rocking causes damage to sensitive and brittle objects as well as safety hazards if it results in the overturning of heavy objects. One goal of this study was to define the rocking response of rigid contents in a conventional braced frame hospital. In general, larger and stockier objects were less likely to overturn. Also, overturning was more prevalent higher up in the building while the location of an object within a given story had little effect. Another objective was to determine the effectiveness of base isolation, a technique that decouples the motion of the building from the ground using flexible bearings, as a strategy to protect contents that are vulnerable to rocking during an earthquake. This was found to be quite effective at reducing both the occurrence of uplift (the initiation of rocking) as well as toppling.

Abstract

The primary seismic response mode of freestanding slender building contents is rocking. Rocking is one of the most damaging response modes due to large accelerations at impact and the possibility of toppling. This study investigates the rocking response of contents within fixed-base and base-isolated buildings so that better-informed decisions can be made, either at the design stage for new structures or during the performance evaluation for existing structures, to mitigate the effects of the destructive rocking behaviour and consequently minimize injury, economic loss, and downtime.

A 3D model of a hospital building was created in OpenSees and analyzed to obtain floor accelerations for a suite of 20 broadband ground motions. These motions were then used as input to compute the rocking responses of many building contents. The rocking responses were compared and contrasted to determine the effect of the block's size, slenderness, floor level, and placement within a level. The rocking response of contents in buildings isolated with lead plug and triple friction pendulum bearings were compared to the fixed-base building to determine the effectiveness of isolation as a means to control rocking. Fragility curves were also created for the fixed-base and isolated buildings.

The vertical component of the floor accelerations had little effect on the rocking response of contents. The significance of this is that the location of an object on a given story does not affect its rocking response. However, higher vertical accelerations did increase the likelihood of the object lifting off the floor. The rocking response of stocky contents increased from one story to the next, but as the slenderness increased this transition became less evident. Base isolation was found to be effective at reducing both the likelihood to uplift and overturn. The longer period systems provided superior protection despite the long period pulse like motion while the damping of the systems had little effect on the rocking response.

Acknowledgements

I would first of all like to thank my two supervisors, Dr. Konstantinidis and Dr. Tait, for their continued support and guidance over the last two years. I appreciate the time you took for both our scheduled and impromptu meetings and for all the advice and encouragement you shared along the way. I would also like to thank you for you detailed editorial work.

I also owe a large thank you to Farzad Nikfar for sharing his models with me as a starting point and his availability and willingness to constantly answer my OpenSees questions. I also would like to acknowledge the rest of the civil engineering graduate students for their comradery and assistance on various engineering problems.

Finally, I would like to thank all my family and friends for their constant support of this endeavour.

Table of Contents

Lay Summary iii
Abstract iv
Acknowledgements v
Table of Contents vi
List of Figures ix
List of Tables xi
List of Symbols xii
List of Abbreviations xvi
Co-Authorship xvii

Chapter 1: Introduction 1

1.1 Importance of nonstructural components 1
1.2 General review of the rocking response 2
1.2.1 Introduction 2
1.2.2 Criterion for the initiation of rocking 3
1.2.3 Derivation of rocking equation of motion 4
1.2.4 Frequency dependence on rocking amplitude 6
1.2.5 Coefficient of restitution 6
1.2.6 General assumptions 7
1.3 Rocking response of objects on an isolated base 7
1.4 Overturning criterion 9
1.5 Rocking fragilities 11
1.6 Impetus and research objectives 13
1.7 Structure of thesis 14
1.8 References 16

Chapter 2: Rocking Response of Unanchored Building Contents 22

Summary 22
2.1 Introduction 22
2.2 Building description 24
2.3 Structural model 26
2.4 Fundamental building properties 29
2.5 Ground motion selection and scaling 31
2.6 Building response 32
2.7 Review of the rocking block 34
2.8 Results and discussion 37

2.8.1 Introduction to rocking spectra and an example response 37
2.8.2 Probability of jumping 38
2.8.3 Effect of vertical acceleration 38
2.8.4 Effect of content placement on a particular floor 40
2.8.5 Effect of floor level 40
2.9 Analytical seismic fragility curves 43
2.9.1 Intensity measure 43
2.9.2 Demand parameter 44
2.9.3 Regression analysis 45
2.9.4 Probability of overturning 46
2.9.5 Fragility curves 47
2.10 Conclusions 49
2.11 References 51

Chapter 3: The Effectiveness of Base Isolation as a Strategy to Protect Freestanding Slender Building Contents against Rocking and Overturning 55

Summary 55
3.1 Introduction 55
3.2 Overview of the building designs 57
3.3 Isolation system design 58
3.3.1 Lead plug rubber bearings 59
3.3.2 Triple friction pendulum bearings 60
3.4 Modeling overview 63
3.4.1 Fixed base building 63
3.4.2 Base isolated superstructure 64
3.4.3 Lead plug rubber bearings 64
3.4.4 Triple friction pendulum bearings 65
3.5 Building periods 66
3.6 Ground motion selection and scaling 66
3.7 Structural response 67
3.8 Review of the dynamics of a rocking object 70
3.9 Effectiveness of seismic isolation in reducing uplift occurrences 71
3.10 Effectiveness of base isolation for reducing rocking responses 72
3.11 Comparison of the rocking response contents in buildings with different isolation systems 75
3.12 Variation in rocking response with floor height 77
3.13 Fragility analysis 78
3.13.1 Demand parameter 78

3.13.2 Univariate intensity measure analysis 79
3.13.3 Bivariate intensity measure analysis 82
3.14 Conclusions 84
3.15 References 86

Chapter 4: Conclusions and Recommendations 92

4.1 Summary 92
4.2 Rocking response of FB building contents 93
4.3 Rocking response of BI building contents 95
4.4 Recommendations and future study 96

Appendix A 99

Derivation of coefficients of friction 99
Derivation of vertical reaction force on rocking block 103

Appendix B 104

Member sizes 104

Appendix C 105

Ground motions 105

List of Figures

Figure 1-1. Overturned bookshelves 2
Figure 1-2. Overturned computer equipment 2
Figure 1-3. Rocking rigid block 5
Figure 2-1. Left: Elevation view of SCBF. Right: Plan view of modeled bay. 25
Figure 2-2. First story brace hysteresis. 27
Figure 2-3. Capacity curve of modeled frame. 30
Figure 2-4. Scaled ground response spectra for 20 selected earthquakes. 32
Figure 2-5. Floor plan locations where the acceleration time histories were recorded. 33
Figure 2-6. Mean building responses. 33
Figure 2-7. Left: Horizontal floor response spectra at each story. Right: Vertical floor response spectra at various locations on the roof. 34
Figure 2-8. Rocking rigid block. 35
Figure 2-9. Example rocking response of a fridge located near a column. 37
Figure 2-10. Percentage of the earthquakes for which jumping occurred. 38
Figure 2-11. Effect of the vertical acceleration component on the rocking response. 39
Figure 2-12. Rocking spectra at different locations on the roof. 40
Figure 2-13. Rocking spectra for all stories at the corner. 41
Figure 2-14. Slender ($\alpha = 10°$) rocking spectra with coefficient of restitution $e = 0.84$. 42
Figure 2-15. Height v. normalized rocking angle for select block sizes. 43
Figure 2-16. Safe rocking results showing linear relation between ln(IM) and ln(DP). . 45
Figure 2-17. Empirical CDF versus analytical lognormal CDF. 47
Figure 2-18. Fragility curves. 48
Figure 3-1. Left: Elevation view of FB SCBF. Right: BI OCBF 58
Figure 3-2. Left: Schematic of TFP bearing. Right: TFP backbone curve 61
Figure 3-3. Isolation system hysteresis 63
Figure 3-4. Left: Modeled isolator with one column element and two spring elements. Center: Lateral force-deformation. Right: Vertical force-deformation 65
Figure 3-5. Selected ground motion response spectra 67

Figure 3-6. Mean peak building responses for the FB and BI buildings. Left: Peak story drift. Center: Absolute peak floor velocities. Right: Absolute peak floor accelerations 68
Figure 3-7. Floor response spectra at the base for the BI and FB buildings 69
Figure 3-8. Rocking block 70
Figure 3-9. Percent of earthquakes that initiate uplift at different slenderness 72
Figure 3-10. Rocking Spectra for LP isolated building with 2.5 s period, 15% damping and the FB building. 73
Figure 3-11. Average rocking spectra for earthquakes that induced rocking for LP systems with 15% damping for α = 7.5 and 10° 74
Figure 3-12. Rocking response of contents at the roof of different systems 76
Figure 3-13. Boundary map of rocking responses at the base of the LP systems. 77
Figure 3-14. The rocking response v. height in building for two contents with α = 10°. Top: LP buildings. Bottom: TFP buildings. Left: R = 15 cm, Right: R = 75 cm. 78
Figure 3-15. Fragility curves for superstructures with 2.5 s periods. Left: LP systems. Right: TFP systems. 81
Figure 3-16. Bivariate fragility curves. Left: LP systems. Right: TFP systems. 83

List of Tables

Table 2-1. Orthotropic material properties for steel and concrete deck slab. 28
Table 2-2. Periods of the SCBF. 29
Table 2-3. Limit states 45
Table 3-1. Structural steel member schedule 58
Table 3-2. Effective period and damping used for both the LP and TFP isolators 59
Table 3-3. Properties of the LP and TFP isolators 62
Table 3-4. Periods of the frames 66
Table 3-5. Design and actual isolator displacements 67
Table 3-6. Fragility parameters for uplift and overturning 80
Table A-1. Fixed-base building member sizes 104
Table A-2. Base-isolated superstructure member sizes 104
Table A-3. Ground motions selected for time history analysis 105
Table A-4. Peak responses of selected ground motions 106

List of Symbols

α	Slenderness
β	Dispersion; Mean of the natural logarithm of the IM
γ	Ordinary least squares regression parameter
ζ	Assumed damping ratio in superstructure
$\zeta_{eff,D}$	Effective isolation damping ratio at DBE level displacement
η	Ratio of post yield to initial isolation system stiffness
θ	Rotation of rocking block
θ_o	Initial rotation of block
λ	Bivariate analysis parameter
μ	Mean of the natural logarithm of the IM
$\hat{\mu}$	μ which maximizes the likelihood function
μ_1	Coefficient of friction of inner TFP sliders
μ_2	Coefficient of friction of outer TFP sliders
μ_s	Static coefficient of friction
μ_x	Median of natural logarithm of the demand conditioned on the *IM*
ξ	Proficiency of proposed *IM*
ρ	Ordinary least squares regression parameter
σ_x	Standard deviation of X
Φ	Standard normal cumulative distribution function
a_1	Exponent for bivariate analysis
a_2	Exponent for bivariate analysis
A	Effective cross sectional area of slab
b	Half the base width of rocking block
b_s	Unit width of slab
c	Capacity value corresponding to limit state
C	Capacity; random variable
C_s	Base shear coefficient
d	Demand

d_s	Depth of slab
d_1	Inner slider displacement capacity of TFP
d_2	Outer slider displacement capacity of TFP
D	Demand; random variable
D_D	DBE level isolation system displacement
D_M	MCE level isolation system displacement
D_y	Yield displacement of isolation system
e	Coefficient of restitution
E	Effective elastic modulus of slab parallel to ribs
E_c	Elastic modulus of concrete
E_x	Elastic modulus of slab shell element perpendicular to ribs
E_y	Elastic modulus of slab shell element in vertical direction
E_z	Elastic modulus of slab shell element parallel to ribs
$f_{y,e}$	Expected yield strength
F_D	Analytical cumulative distribution
F_D^*	Empirical cumulative distribution
F_y	Vertical force at toe of rocking block
g	Gravity constant
G_c	Shear modulus of concrete
G_{xz}	Shear modulus of shell element in plane of slab
h	Height to center of mass of block
h_b	Height of isolation system
h_1	Half the height of inner TFP slider
h_2	Half the height of outer TFP slider
$I_{cr,x}$	Cracked moment of inertia of slab perpendicular to ribs
$I_{cr,z}$	Cracked moment of inertia of slab parallel to ribs
I_e	Importance factor
k_1	Initial isolation stiffness
k_2	Post yield isolation stiffness

k_c	Bearing compressive stiffness
k_t	Bearing tensile stiffness
k_{eff}	Effective stiffness of isolation system at DBE level displacement
L	Length of brace
L_1	Effective radius of inner TFP surfaces
L_2	Effective radius of outer TFP surfaces
m	Mass of block
n	Number of dynamic response analyses
p	Block frequency parameter
P_{ex}	Probability of exceedance given safe rocking
P_f	Conditional probability that an EDP will exceed a limit state given an IM
P_o	Probability of overturning
Q	Characteristic strength of bearing
r	Square of the coefficient of restitution
R	Distance from toe to block's center of mass
R_1	Radius of inner slider surfaces
R_2	Radius of outer surfaces
S_{D1}	Design spectral acceleration at 1s period
S_{DS}	Design spectral acceleration at short period
t	Uncracked depth of slab
T	Period of structure
T_D	Effective period of isolation system at DBE level displacement
T_{fv}	Period of free vibration of rocking block
u_h	Horizontal isolation system displacement
u_v	Vertical isolation system displacement
$\ddot{U}_g^x$	Horizontal acceleration at base of block
$\ddot{U}_g^y$	Vertical acceleration at base of block
$v_{s,30}$	Average shear wave velocity for top 30 m of soil
V	Base shear

W	Weight of building
X	Natural logarithm of the demand
$\mathbf{y}(t)$	ODE state vector
z	Binormal demand variable
Z	Lognormally distributed random variable

List of Abbreviations

AISC	American Institute of Steel Construction
ANSI	American National Standards Institute
ASCE	American Society of Civil Engineers
BI	Base-isolated
CDF	Cumulative distribution function
DP	Demand parameter
DBE	Design based earthquake
FB	Fixed base
IM	Intensity measure
LFRS	Lateral force resisting system
LP	Lead plug rubber bearing
LS	Limit state
MCE	Maximum considered earthquake
OCBF	Ordinary concentrically braced frame
ODE	Ordinary differential equation
PGA	Peak ground acceleration
PGD	Peak ground displacement
PGV	Peak ground velocity
SCBF	Special concentrically braced frame
SDI	Steel Deck Institute
TFP	Triple friction pendulum

Co-Authorship

Since this thesis has been organised as a sandwich thesis, several authors contributed to each of the main chapters. The body chapters of this thesis have been co-authored as follows.

Chapter 2: The Rocking Response of Nonstructural Rigid Contents in a SCBF

Authors: Linde S., Konstantinidis D., Tait M.

The hospital building was designed by F. Nikfar and S. Linde. Both the OpenSees and Matlab modeling were carried out by S. Linde. The analysis and discussion of the results were also done by S. Linde. The manuscript and figures were prepared by S. Linde. D. Konstantinidis and M. Tait gave advice, helped interpret the data, and piloted the direction of research. This chapter will be submitted to the Journal of Earthquake Engineering and Structural Dynamics.

Chapter 3: The Effectiveness of Base Isolation as a Strategy to Protect Contents against Rocking

Authors: Linde S., Konstantinidis D., Tait M.

The superstructures for the BI buildings were designed and modeled in OpenSees by F. Nikfar. The isolation system design and modeling was done by S. Linde. The Matlab analysis as well as the explanation and documentation of the results were also done by S. Linde. The manuscript was created by S. Linde under the supervision of Dr. Konstantinidis and Dr. Tait. This chapter will be submitted for publication in a peer reviewed journal.

Chapter 1: Introduction

1.1 Importance of nonstructural components

The majority of injury and overall losses in recent American earthquakes can be attributed to the damage and failure of nonstructural components [1-5]. Nonstructural components include anything that is not part of the structural system of the building. This encompasses everything from architectural, electrical, and plumbing systems to actual building contents such as furniture, fixtures and equipment. The failure of these components can be a significant safety hazard during an earthquake. Life safety hazards include damage of life-safety systems like fire protection piping and falling debris such as light fixtures and cladding [1]. Not only is it important to consider the seismic design of nonstructural components from a health perspective, it can also lead to significant savings [6]. Nonstructural components typically comprise at least 80-90% of the total value of a building and will experience damage at lower earthquake intensities than the structural system [7, 8]. Continued functionality is paramount for post-disaster buildings such as hospitals, fire stations, and government buildings. In recent earthquakes, including the 2001 Nisqually and 2010 Chile earthquakes, the failure of nonstructural components was the cause for loss of functionality in many of these critical facilities [9-13]. Despite this, the majority of seismic design research over the years has been on improving the performance of structural systems. While structural integrity is imperative for life safety, the performance of nonstructural components plays an equally important role in successful performance-based earthquake engineering. One of the reasons that this area has received a lower level of attention is the difficulty associated with predicting the response of nonstructural components. This is especially true for building contents, for which even the location of the object may be unknown or subject to change.

During an earthquake a content such as a piece of equipment can slide, rock, overturn, jump, and twist, or likely a combination of these responses. It is essential to first understand the response of these contents so that they can be properly designed. Slender rigid contents such as shelves, filing cabinets, emergency generators, and equipment typically respond by rocking about their edges. This dissertation focuses

exclusively on documenting the rocking response of rigid contents within archetypal buildings. Rocking is one of the most damaging response modes that a building content can undergo due to large accelerations at impact and the potential for overturning [14], both of which can cause severe damage or loss of functionality [1]. Toppling of large rigid contents such as fridges and storage racks can also pose a significant health risk to occupants [1]. Figure 1-1 and Figure 1-2 show overturned bookshelves and computer equipment from the 2001 Nisqually earthquake.

Figure 1-1. Overturned bookshelves [15]

Figure 1-2. Overturned computer equipment [16]

1.2 General review of the rocking response

1.2.1 Introduction

Ever since Housner published his seminal paper in 1963 on the dynamic rocking response of rigid blocks [17], the topic of rocking has received considerable attention. Many studies have been devoted to understanding the rocking response, perhaps intrigued by

the apparent simplicity of a problem with such complex behavior. Generally the blocks are subjected to trigonometric pulse-type or strong ground motion excitations for the purpose of determining the response of objects like classical columns [e.g. 18], electrical equipment [e.g. 19], or statues [e.g. 20] with a strong emphasis placed on the ability to predict uplift and overturning. A probabilistic approach is usually appropriate since the rocking system is both time dependant and extremely sensitive to small changes in its input parameters [21- 23].

1.2.2 Criterion for the initiation of rocking

By considering only in-plane motion, Shenton [24] identified criteria for the possible modes of response of a freestanding rigid object (slide, rock, and slide-rock) and derived initiation criteria for each. Sliding occurs when the horizontal inertial force exceeds the frictional force at the base of the content as shown in Equation (1.1). Rocking is initiated when the sum of the moments about one of the block's corners due to the horizontal inertial force exceeds the restoring moment due to its weight, given that there is a sufficient frictional force to prevent sliding. The horizontal acceleration needed to satisfy this condition is given in Equation (1.2).

$$\left|\ddot{U}_f^x\right| \geq \mu_s \left(g + \ddot{U}_f^y\right) \tag{1.1}$$

$$\left|\ddot{U}_f^x\right| \geq \left(g + \ddot{U}_f^y\right) \tan\alpha \tag{1.2}$$

where $\ddot{U}_f^x$ and $\ddot{U}_f^y$ are the horizontal and vertical floor accelerations respectively, μ_s is the static coefficient of friction, g is the gravitational constant, and α is the slenderness as shown in Figure 1-3. Note that uplift is only a function of the base excitation and the block's slenderness and therefore independent of size. The static coefficient of friction necessary for rocking to initiate is shown in Equation (1.3). Equation (1.4) gives the coefficient of friction needed to maintain pure rocking at every timestep. A derivation of Equations (1.3) and (1.4) is given in Appendix A. Slide-rock occurs when the static frictional force is large enough to prevent sliding but too small to sustain rocking. The presence of vertical motion affects both these coefficients of friction. An upward acceleration increases the normal force and decreases the required frictional coefficient

while and downward acceleration does the opposite. In general, the presence of vertical excitation may or may not increase the likelihood of sliding depending on the phase relationship between the horizontal and vertical motion.

$$\mu_s \geq \left| \frac{\left|\ddot{U}_f^x\right|\left(5-3\cos\left(2\alpha\right)\right)+3\left(\ddot{U}_f^y+g\right)\sin\left(2\alpha\right)}{3\left(\ddot{U}_f^y+g\right)\left(\cos\left(2\alpha\right)-1\right)+3\left|\ddot{U}_f^x\right|\sin\left(2\alpha\right)+8\ddot{U}_f^y+8g} \right| \tag{1.3}$$

$$\mu_s \geq \left| \frac{\ddot{U}_f^x\left(5-3\cos\left(2\left(\alpha-\left|\theta\right|\right)\right)\right)-3\mathrm{sgn}(\theta)\left(\ddot{U}_f^y+g\right)\sin\left(2\left(\alpha-\left|\theta\right|\right)\right)+8\mathrm{sgn}(\theta)R\dot{\theta}^2\sin\left(\alpha-\left|\theta\right|\right)}{3\left(\ddot{U}_f^y+g\right)\left(\cos\left(2\left(\alpha-\left|\theta\right|\right)\right)-1\right)-3\mathrm{sgn}(\theta)\ddot{U}_f^x\sin\left(2\left(\alpha-\left|\theta\right|\right)\right)-8R\dot{\theta}^2\cos\left(\alpha-\left|\theta\right|\right)+8\ddot{U}_f^y+8g} \right| \tag{1.4}$$

where θ is the block's angle of rotation and R is the distance from the pivot point to the center of mass as shown in Figure 1-3. It is also typical to assume during rocking analysis that the block translates laterally with zero angular velocity or rotational energy up until the point that it uplifts and begins to rock. However, there may be small initial movement (energy) in the block if either the base or block is not perfectly rigid and square, such as equipment with one leg slightly shorter than the others. Once rotational energy exists, even lower amplitude motion than is necessary to initiate rocking can cause resonance and add energy to the system to build up rocking, even resulting in overturning [25].

1.2.3 Derivation of rocking equation of motion

Since the equations of motions governing the rocking motion are central to this study a derivation of them was deemed appropriate. The kinetics equation for a rigid body rotating on a plane about a fixed point is given by

$$\mathbf{M}_O = I_O\ddot{\boldsymbol{\theta}} + \bar{\mathbf{p}}\times m\mathbf{a}_O \tag{1.5}$$

where $\mathbf{M}_O$ is the sum of the moments about the fixed point O, I_O is the moment of inertia of the rigid body about O, $\ddot{\boldsymbol{\theta}}$ is the angular acceleration, $\bar{\mathbf{p}}$ is a vector from O to the center of mass, m is the mass, and $\mathbf{a}_o$ is the acceleration at O. For a rectangular block, the moment of inertia about the corner is:

$$I_O = \frac{4}{3}mR^2 \tag{1.6}$$

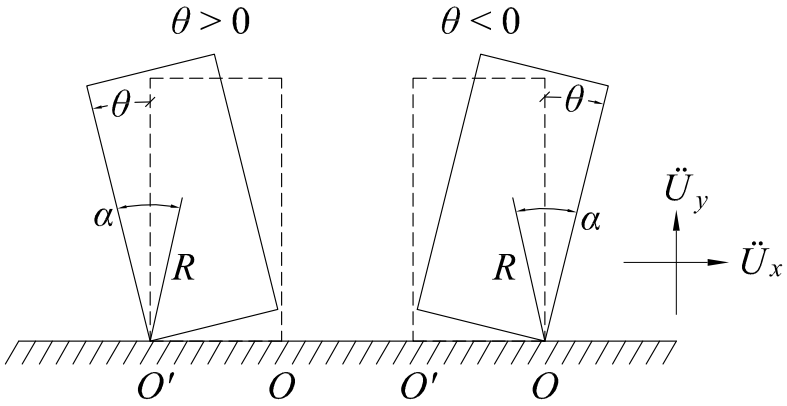

Figure 1-3. Rocking rigid block

For rocking of a rigid content such as shown in Figure 1-3 about its fixed corner *O*' ($\theta \geq 0$) Equation (1.5) becomes,

$$R\sin(\theta-\alpha)\mathbf{E}_x \times \left(-mg\mathbf{E}_y\right) = -\frac{4}{3}mR^2\ddot{\theta}\mathbf{E}_z + \left(R\sin(\theta-\alpha)\mathbf{E}_x + R\cos(\theta-\alpha)\mathbf{E}_y\right) \times m\left(\ddot{U}_g^x\mathbf{E}_x + \ddot{U}_g^y\mathbf{E}_y\right) \tag{1.6}$$

where $\mathbf{E_x}$, $\mathbf{E_y}$, and $\mathbf{E_z}$ are the unit vectors which constitute the standard basis in Euclidean space. Solving the cross products and rearranging,

$$-mgR\sin(\theta-\alpha)\mathbf{E}_z = -\frac{4}{3}mR^2\ddot{\theta}\mathbf{E}_z + m\left(R\sin(\theta-\alpha)\ddot{U}_g^y - R\cos(\theta-\alpha)\ddot{U}_g^x\right)\mathbf{E}_z \tag{1.7}$$

or,

$$\ddot{\theta} = \frac{3}{4R^2}\left(\left(g+\ddot{U}_g^y\right)R\sin(\theta-\alpha) - \ddot{U}_g^x R\cos(\theta-\alpha)\right) \tag{1.8}$$

Substituting in the frequency parameter,

$$p = \sqrt{\frac{3g}{4R}} \tag{1.9}$$

the equation of motion is obtained,

$$\ddot{\theta} = -p^2\left(\left(1+\frac{\ddot{U}_g^y}{g}\right)\sin(\alpha-\theta) + \frac{\ddot{U}_g^x}{g}\cos(\alpha-\theta)\right) \tag{1.10}$$

For rocking about the other corner *O* ($\theta < 0$) the same process can be applied to derive,

$$\ddot{\theta} = -p^2\left(\left(1+\frac{\ddot{U}_g^y}{g}\right)\sin\left(-\theta-\alpha\right)+\frac{\ddot{U}_g^x}{g}\cos\left(-\theta-\alpha\right)\right) \tag{1.11}$$

These can be combined to form the regular equation of motion given in Equation (1.12).

$$\ddot{\theta} = -p^2\left(\left(1+\frac{\ddot{U}_g^y}{g}\right)\sin\left(\mathrm{sgn}\left(\theta\right)\alpha-\theta\right)+\frac{\ddot{U}_g^x}{g}\cos\left(\mathrm{sgn}\left(\theta\right)\alpha-\theta\right)\right) \tag{1.12}$$

1.2.4 Frequency dependence on rocking amplitude

The frequency parameter, p, defined in Equation (1.9) is a not a direct measure of the natural frequency of a rocking block. It is about 2.7 rad/s for a refrigerator (R = 1 m) and about 5.4 rad/s for a desktop computer (R = 0.25 m). The frequency parameter is fixed for a given block even though the period of rocking is strongly dependant on the rocking amplitude. Housner [17] gave the period of free vibration, T, for an undamped block released from an initial angle θ_o as

$$T = \frac{4}{p}\cosh^{-1}\left(\frac{1}{1-\theta_o/\alpha}\right) \tag{1.13}$$

It is evident that an object with a larger frequency parameter will undergo shorter period oscillations when released from the same normalized initial rotation. Another way to visualize this is that p is the pendulum frequency of the block as if it were hanging by its rocking point [26].

1.2.5 Coefficient of restitution

The block is assumed to instantaneously transfer smoothly from rocking about one toe to the other. In order for this to occur, the angular momentum of the block directly before and after the impact must be conserved. For this to happen, the impact must be plastic, i.e., the block must lose energy every time it rocks. Energy is removed from the rocking system using the classical concept of a coefficient of restitution, e. This coefficient is a measure of the kinetic energy retained in the system after impact and is defined as the ratio of angular velocities immediately before and after impact

$$e = \frac{\dot{\theta}_2}{\dot{\theta}_1} \tag{1.14}$$

The maximum coefficient of restitution possible for which a block will undergo smooth rocking is given by [17]

$$e = 1 - \frac{3}{2}\sin^2\alpha \tag{1.15}$$

From this equation it is evident that stockier blocks, higher α, must lose more energy at each impact, i.e. have higher impact damping. Generally, using a smaller coefficient of restitution will result in a decrease in the rocking response. However, for a single record even a small change in the coefficient of restitution can cause a large increase or decrease in the rocking response [21, 27, 28].

1.2.6 General assumptions

Some common simplifications are usually made when studying the rocking motion of individual objects. Typically the rocking contents under consideration are assumed to be completely rigid which was shown to be accurate by Konstantinidis and Makris [29] for large laboratory equipment typically found in life science laboratories. Another limitation on most studies is that they only consider the rocking response of the object in a vertical plane subject to horizontal excitation only. The few studies that have analysed this problem in 3D, with varying levels of success, have noted that planar rocking is not always an accurate assumption even when only considering unidirectional excitation [30 – 33]. Another assumption that is generally made for the sake of generic results is that the rocking blocks under consideration are horizontally symmetric, that is, the center of mass is halfway between the rocking corners. The several studies that have examined non-symmetric blocks have shown that they are more prone to overturning than a similar symmetric block, though it depends on the excitation and dimensions [34 – 38].

1.3 Rocking response of objects on an isolated base

The most common method to prevent rocking is anchoring. However, some objects which are susceptible to rocking cannot be anchored because they are brittle and would break under the seismic forces or because anchoring would damage the content. In other cases, objects need to be mobile within a facility and therefore anchoring them inhibits their functionality [39]. In this case, base isolation of the individual object is the most popular

passive control technique used to mitigate the damaging effects of rocking. Research in this area has been mainly for protecting individual statues and art objects that have cultural significance and inestimable value [40 – 42]. The idea is that the isolation system is able to decouple the object from the motion of the ground or floor so that in an earthquake the object will experience lower seismic intensity levels and undergo smaller rotations, or perhaps not uplift at all. One of the ways that rocking on an isolated base differs from rocking at ground level is that the mass and motion of the base must be taken into account in the equations of motion. This modifies the energy in the system so that there is a jump in the velocity of the base and it becomes possible for the block to cease rocking at impact instead of rotating to the other toe [18]. The maximum coefficient of restitution is also smaller [41]. Chiozzi et al. [41] examined the response of monolithic pinnacles atop the masonry city gate in Ferrara, Italy. They used a FEM of the gate and concluded that the double concave curved steel sliders under consideration were effective at preventing rocking of the pinnacles under design earthquake level motions. Vestroni and Di Cintio [20] found multi-stage high damping laminated rubber bearings were successful at reducing the accelerations felt by statues and preventing rocking. A similar study done by Caliò and Marletta [42] concluded that viscous elastic isolation systems were effective at protecting art objects under impulsive base accelerations. Contento and Di Egidio [43] also investigated the benefits of base isolation using visco-elastic isolators for impulsive and seismic base excitations. They found that increasing the isolator period or damping increased the amplitude of the impulse needed for overturning, but decreased the difference between amplitude needed for uplift and overturning. Perhaps the most comprehensive study on the analysis of rigid blocks rocking on an isolated base was done by Vassiliou and Makris [18]. They used viscoelastic bearings and single and double concave sliding bearings and Ricker wavelet excitation. They concluded that while isolation increases the minimum ground acceleration required to cause overturning, it also depreciates from the property of blocks to remain more stable as the frequency of the record increases or the blocks get larger. For this reason large objects subjected to pulses with $\omega_{pulse}/p > 6$ had superior stability when not isolated.

1.4 Overturning criterion

Another area that has received a lot of attention for obvious reasons is the development of equations to predict whether or not a rigid object will overturn given a base acceleration time history. Kirkpatrick was the first to investigate this problem and derived Equation (1.16) using small angle approximations for predicting the minimum amplitude, a, of a half sin wave acceleration pulse with period T_g that would topple a rigid block [44].

$$a = g\alpha\sqrt{1+\frac{I_o}{mgR}\left(\frac{2\pi}{T_g}\right)^2} \tag{1.16}$$

Later, Housner [17] examined the response of a rocking block subjected to a series of impulses arranged so that the velocity time history is incrementally $\pm\Delta v$. This represents an idealized earthquake with a constant undamped velocity response spectrum. He equated the average energy built up during the record to the energy required to overturn the block. Equation (1.17) gives the slenderness for which 50% of the blocks will overturn given N pulses.

$$\alpha = \sqrt{\frac{mR^2}{I_o}\frac{1}{Rg}}\left(\Delta v\right)\sqrt{N} \tag{1.17}$$

These equations have since been shown to be unconservative and inaccurate [2, 19, 45]. However, much work has built upon these pioneering studies towards creating better predictions of overturning. Typically trigonometric pulse excitation is used in such studies since they afford a linearization of the equations of motion and can be representative of near source strong ground motions. Single pulses are used instead of continuous motion because they usually produce higher responses [46]. Rocking resonance under continuous harmonic motion is extremely unlikely since the effective frequency of the block depends on the rocking amplitude such that the motion would need precise time-varying frequency [26].

Some of these studies have been conducted to determine the maximum height of a block that will not overturn for a given base width and excitation. This technique allows designers to estimate an object's vulnerability and determine the need for anchoring.

Ishiyama [47, 48] proposed minimum level accelerations and velocities that are needed for overturning for a rigid block under harmonic motion

$$h = \max\left\{\frac{b}{A}g; C_1 g\left(\frac{b}{V}\right)^2\right\}; C_1 = 0.2133 \tag{1.18}$$

where A is the peak acceleration, V is the peak velocity, and b and h are half the block's width and height, respectively. Psycharis et al. [49] improved on this, arriving at

$$h = b\left(\frac{g}{A}\right)^{1.053}\left(\frac{\omega}{p}\right)^{1.263}\left(0.20 + 1.30r - 1.21r^2\right)^{1.053} \tag{1.19}$$

where r is the coefficient of restitution squared, $r = e^2$, and ω is the harmonic frequency. Recently Arredondo and E. Reinoso [46] revisited this problem and modified Ishiyama's model into Equation (1.20) for a rigid block under a variable amplitude sine pulse.

$$h = \max\left\{\frac{b}{A}g; e^{\beta_o} g\left(\frac{b}{V}\right)^2\right\}; \beta_o = 0.519\ln(\omega) + 0.329 \tag{1.20}$$

They subsequently used this equation to predict overturning during free field strong ground motions. The frequency of the record was taken as the break point between the constant acceleration and velocity regions on the velocity spectrum. The equation produced mostly good results although it tended to be conservative.

Two distinct modes of overturning were documented by Zhang and Makris [50] corresponding to toppling without impact and toppling after exhibiting one or more impacts. Consequently, for sinusoidal pulses, a range of acceleration amplitudes exists where blocks may undergo safe rocking whereas similar frequency pulses of lower amplitude may topple after several rocking cycles and pulses of higher amplitude will topple without impact. Another approach to the rocking problem is to solve the equations of motion directly for each these modes. Building of the work of Anooshehpoor et al. [51], Dimitrakopoulos and Dejong [52] developed a closed form solution that defines rocking for a finite duration single trigonometric pulse-type ground motion. They discovered that when expressed in correct dimensionless-orientationless groups the rocking response becomes self-similar so that the response of the linearized equation of

motion is directly determinable for slender blocks and rotations and must only be scaled by the intensity and frequency of the excitation. This makes it possible to finally create overturning spectra without numerous analyses. Unfortunately, to the author's knowledge, no accurate overturning prediction models have been created for rigid block motion under seismic excitation.

1.5 Rocking fragilities

Fragility curves are tools that can be used to assess the vulnerability of a building content to damage for a given level of floor motion intensity. A limited number of studies have published fragility curves for rocking or overturning of rigid contents. The following discussion outlines a few of these studies and their key contributions and conclusions. Dimitrakopoulos and Paraskeva [53] created fragility curves for rigid blocks rocking under near fault excitations. Synthetic ground motions derived using Mavroedis and Papageorgiou wavelets were used with and without high frequency content added. The rocking responses of a piece of electrical equipment were calculated for 3500 different ground motions. They examined 6 different intensity measures and concluded that the two dimensionless slenderness IMs given in Equation (1.21) gave the best fit, although neither was capable of producing very accurate predictions.

$$IM_1 = \frac{pPGV}{g\tan\alpha} \qquad IM_2 = \frac{PGA}{g\tan\alpha} \tag{1.21}$$

where PGV and PGA are the peak horizontal ground velocity and acceleration. Interestingly, they pointed out that for safe rocking results, the responses scale differently under high and low intensity ground motions with the threshold at a PGA of approximately $1.3g\tan\alpha$. They then combined the best frequency ratio intensity measure $\left(PGA/pPGV\right)$ with the best dimensionless slenderness one to form a bivariate intensity measure which was used to create superior overturning fragility curves. They found that the scatter in the data for the pulse-type motion was significantly less than when high frequency content was added. Also, for an equal PGV, the pure pulse-type motion was more likely to result in overturning than the one with high frequency content added [53].

Kafle et al. [54] investigated the use of peak displacement demand as an intensity measure. The peak displacement demand was taken as the highest value on the 5% damped displacement response spectrum for natural periods of up to 5 s. Several size and slenderness blocks were subjected to actual and synthetic strong ground motions. The demand parameter was taken as the displacement at the top of the block. They found that the peak displacement demand was better correlated to the likelihood of overturning than the peak velocity or peak acceleration demands. Fragility curves were then created for the individual size and slenderness blocks with larger and stockier blocks being less vulnerable to overturning.

In 2013 Psycharis et al. [55] assessed the seismic reliability of a classical column on the Parthenon Pronaos composed of 12 stacked drums. Synthetic near-fault ground motions with directivity pulses were created for a variety of epicenter distances and magnitudes. The two demand parameters that they investigated were the capital displacement and the residual displacement of the drums. The two intensity measures that they used were *PGA* and *PGV* with the *PGV* giving marginally less scatter in the data. They concluded that, counter-intuitively, the rocking response of the columns did not increase with the period of the pulse for very long periods (above about 4.0 s for the column) but actually decreased. They also found that for long-period pulses from high magnitude earthquakes the *PGA* from the high frequency content drives the overturning of the content and that larger *PGA*s are needed as the frequency of the high frequency component increases.

Some studies have defined the rocking problem as a stochastic process solved using diffusive Markov analyses. While a detailed explanation is outside the scope of this introduction, this method can be used to determine the seismic reliability of rocking contents. Using this technique several studies have treated toppling as the excursion of the total energy of the system past a threshold for the first time and produced reliability and fragility curves [56, 57]. However, these curves are given only for specific parameters and many simplifications are typically made in the process including modeling the ground

motion as an evolutionary process and the quasi-conservative averaging of the state space.

1.6 Impetus and research objectives

The seismic design of nonstructural components must also be included in the holistic process of performance based earthquake engineering in order to create resilient communities in which critical facilities such as hospitals can remain functional after moderate to severe earthquakes. Unfortunately, literature and experimental work on the response of hospital equipment and contents, especially in rocking, is scarce. Codes are often based on intuition and engineering experience rather than experimental and analytical research [58]. While the rocking response of slender rigid blocks has been extensively studied for the last five decades, surprisingly little research has been done in the area of rocking contents within buildings. Although the same equation of motion governs, the effect of the building's filtration of the ground motion is unknown. The general purpose of this thesis is to construct a qualitative and quantitative characterization of the rocking response of slender building contents throughout fixed-base (FB) and base-isolated (BI) buildings.

In Chapter 2 a FB building was modeled in 3D so that the effect of the content's location on the rocking response could be analyzed. The result of the content's location within a given story was studied by contrasting the response of contents throughout the story from near columns to the center of the bay. The effect of height within the building was also analysed for contents of various sizes and slenderness. The impact of the vertical floor acceleration on the response was determined by comparing the rocking responses calculated using vertical and horizontal base accelerations to those of horizontal only.

The goal of Chapter 3 is to better understand the effectiveness of base isolation systems at eliminating or reducing rocking. Many hospitals and museums are now being built using seismic isolation technology to reduce floor motion intensities and protect expensive equipment and invaluable art. However, it has been postulated that the long period motion of BI superstructures could act as a 'static' push on the contents and topple objects which may have remained upright in a comparable FB building. This study

determines if and under what circumstances this occurs. The effectiveness of the various base isolation systems is also compared for many size and slenderness contents.

One of the main outcomes of this study is the development of fragility curves for both FB and BI buildings. Fragility curves are tools that allow an engineer to quickly assess the vulnerability of an object during the design phase or during a retroactive risk analysis. The significance of this thesis is that it contributes toward the improved seismic design of slender building contents and equipment to mitigate the economic loss, injury and downtime succeeding an earthquake.

1.7 Structure of thesis

This thesis was prepared for McMaster University in agreement with the regulations of a sandwich type thesis. It is divided into 4 chapters. The first chapter covers the introduction and a general overview of rocking as well as the research objectives. The analytical studies done on the rocking response of contents in FB and BI buildings are detailed in chapters 2 and 3. The last chapter contains the final conclusions as well as limitations of their applicability and recommendations for future studies. Since the middle chapters were prepared separately as standalone documents there is brief overlap between chapters mainly in the introductions and conclusions.

Chapter 2 examines the response of contents in an archetypal special concentrically braced frame hospital located in Los Angeles. The hospital was subjected to 20 broadband DBE level ground motions and the floor responses were recorded at every story. An OpenSees model was created in 3D of one bay width by the length of the building and was used to determine the accelerations at various places throughout each story. These floor acceleration time histories were then used as input to calculate the rocking response of various size and slenderness contents. The response of the different contents in different locations are compared and contrasted. Finally, rocking fragility curves are presented.

A parallel study for BI buildings is detailed in Chapter 3. Several isolation systems with varying effective periods and damping were designed for a hospital in Los Angeles. Both triple friction pendulum and lead plug rubber bearings systems are investigated.

OpenSees models were again used to obtain the floor motion time histories, this time in 2D. The rocking responses at each level of the superstructures were calculated for a variety of size and slenderness blocks. The effectiveness of the isolation systems at preventing contents from rocking is examined by comparing them to the FB building. The different isolation systems are compared and contrasted with respect to their ability to supress rocking. Rocking fragility curves are created for contents in each BI superstructure.

1.8 References

1. Federal Emergency Management Agency (FEMA). Reducing the risks of nonstructural earthquake damage – A practical guide, Fourth edition. *FEMA E-74* 2011.
2. Soong T. Seismic performance of nonstructural elements during the Loma Prieta earthquake. *Report NIST SP 796, Proceedings of the 22nd Joint Meeting U.S.-Japan Cooperative Program in Natural Resources Panel on Wind and Seismic Effects, National. Institute of Standards and Technology*, Gaithersburg, Maryland, 331-336, 1990.
3. Soong T, Chen G, Wu Z, Zhang R, Grigoriu M. Assessment of the 1991 NEHRP provisions for nonstructural components and recommended revisions. *Report NCEER-93-0003, National Center for Earthquake Engineering Research*, Buffalo, N.Y. 1993.
4. Reitherman R, Sabol T. Northridge earthquake of January 17, 1994: reconnaissance report -nonstructural damage. *Earthquake Spectra, EERI* 1995; **11** (Supp):453-514.
5. Phipps M. The impact of nonstructural damage on building performance: reflections on the 1994 Northridge earthquake. *Report UCB/EERC- 97/05, The EERC-CUREE Symposium in Honor of Vitelmo V. Bertero, Earthquake Engineering Research Center*, University of California, Berkeley, California, 173-178. 1997.
6. Kircher C.A. It makes dollars and sense to improve nonstructural system performance. *Proceedings of ATC 29-2 Seminar on Seismic Design, Performance and Retrofit of Nonstructural Components in Critical Facilities, Applied Technology Council*, Newport Beach, CA, 2003.
7. Taghavi S, Miranda E. Response assessment of nonstructural building elements. *Report No. PEER-2003/05, Pacific Earthquake Engineering Research Center*, University of California, Berkeley, 2003.
8. Comerio M. PEER testbed study on a laboratory building: exercising seismic performance assessment. *Report No. PEER 2005-12 Pacific Earthquake Engineering Research Center*, University of California, Berkeley, CA, 2005.

9. Filiatrault A, Uang C, Folz B, Christopoulos C, Gatto K. Reconnaissance report of the February 28, 2001 Nisqually (Seattle-Olympia) earthquake. *Report No SSRP 2000-15 Structural Systems Research Project, Department of Structural Engineering*, University California, San Diego, La Jolla, CA, 2001.
10. American Society of Civil Engineers (ASCE). Minimum design loads for buildings and other structures*, ASCE 7-10*, Reston, VA, 2010.
11. Myrtle R, Masri S, Nigbor M, Caffrey J. Classification and prioritization of essential systems in hospitals under extreme events. *Earthquake Spectra* 2005; **21**(3): 779–802.
12. Mosqueda G, Retamales R, Filiatrault A, Reinhorn A. Testing facility for experimental evaluation of non-structural components under full-scale floor motions. *The Structural Design of Tall and Special Buildings* 2008; **18**(4): 387–404.
13. Miranda E, Mosqueda G, Retamales R, Pekcan G. Performance of nonstructural components during the 27 February 2010 Chile earthquake. *Earthquake Spectra* 2012; 28(S1): S453-S471.
14. Priestley M.J.N, Evison R.J, Carr A.J. Seismic response of structures free to rock on their foundations. *Bulletin of the New Zealand National Society for Earthquake Engineering* 1978; **11**(3):141–150.
15. Sharifov S. Non-structural mitigation. *Youtube.ca* 2011.
16. Creative Construction Solutions. Earthquake engineering and seismic services from CCS. Chesterfield MO, 2016.
17. Housner G. The behavior of inverted pendulum structures during earthquakes. *Bulletin of the Seismological Society of America* 1963; **53**:403–417.
18. Vassiliou M, Makris N. Analysis of the rocking response of rigid blocks standing free on a seismically isolated base. *Earthquake Engineering and Structural Dynamics* 2012; **41**: 177–196.
19. Makris N, Roussos Y. Rocking response and overturning of equipment under horizontal pulse-type motions. *Report No. PEER 1998-05, Pacific Earthquake Engineering Research Center*, University of California, Berkeley, California, 1998.

20. Vestroni F, Di Cinto S. Base isolation for seismic protection of statues. *Twelfth World Conference on Earthquake Engineering*, New Zealand, 2000.
21. Yim C, Chopra A, Penzien J. Rocking response of rigid blocks to earthquakes. *Earthquake Engineering and Structural Dynamics* 1980; **8**:565–587.
22. Makris N, Roussos Y. Rocking response of rigid blocks under near-source ground motions. *Géotechnique* 2000; **50**(3): 243–262.
23. Makris N, Konstantinidis D. The Rocking spectrum and the limitations of practical design methodologies. *Earthquake Engineering and Structural Dynamics* 2003; **32**(2): 265–289.
24. Shenton H. Criteria for initiation of slide, rock, and slide-rock rigid-body modes. *Journal of Engineering Mechanics* 1995;**122**(7): 690-693.
25. Dejong M. Amplification of rocking due to horizontal ground motion. *Earthquake Spectra EERI* 2012; **28**(4): 1405-1421.
26. Dimitrakopoulos E, DeJong M. Overturning of retrofitted rocking structures under pulse-type excitations. *Journal of Engineering Mechanics, ASCE* 2012; **138**: 963-972.
27. Aslam M, Fodden W, Scalise D. Earthquake rocking response of rigid blocks. *Journal of Structural Engineering Division (ASCE)* 1980; **106**: 377-392.
28. Spanos P, ASCE M, Koh A. Rocking of rigid blocks due to harmonic shaking. *Journal of Engineering Mechanics* 1984; **110**(11): 1627-1642.
29. Konstantinidis D, Makris N. Experimental and analytical studies on the seismic response of freestanding and anchored laboratory equipment. *Report No. PEER 2005/07*, Pacific Earthquake Engineering Research Center, University of California, Berkeley, CA. 2005.
30. Chatzis M. The dynamics of rigid bodies on moving deformable support media. Phd. Columbia University, New York, New York, 2012.
31. Yanheng L, Baoping S. Response of 3D free axisymmetrical rigid objects under seismic excitations. Phd. Graduate University of Chinese Academy of Sciences, Beijing, China.

32. Konstantinidis D, Makris N. The dynamics of a rocking block in three dimensions. In proceedings of the 8th HSTAM International Congress on Mechanics, Patras, Greece, July 5-7, 2007.
33. Di Egidio A, Alaggio R, Contento A, Tursini M, Della Loggia E. Experimental characterization of the overturning of three-dimensional square based rigid block. *International Journal of Non-linear Mechanics* 2014; 69: 137–145.
34. Contento A, Di Egidio A. Investigations into the benefits of base isolation for non-symmetric rigid blocks. *Earthquake Engineering and Structural Dynamics* 2009; **38** (**7**): 849–866.
35. Boroscheck R, Romo D. Overturning criteria for non-anchored non-symmetric rigid bodies, *Proceedings of the 13th World Conference on Earthquake Engineering*, Vancouver, Canada, 2004.
36. Purvance M, Anooshehpoor A, Brune J. Freestanding block overturning fragilities: numerical simulation and experimental validation, *Earthquake Engineering Structural Dynamics* 2008; **37**(5), 791–808.
37. Fielder W, Virgin L, Plaut R. Experiments and simulation of overturning of an asymmetric rocking block on an oscillating foundation, *European Journal of Mechanics A/Solids* 1997; **16**(5): 905–923.
38. Wittich C, Hutchinson T. Shake table tests of stiff, unattached, asymmetric structures. *Earthquake Engineering and Structural Dynamics* 2015; **44**(14):2425-2443.
39. Dar A, Konstantinidis D, El-Dakhakhni W.W. Evaluation of ASCE 43-05 seismic design criteria for rocking objects in nuclear facilities. *Journal of Structural Engineering*. 2016: (in press).
40. Roussis P, Pavlou E, Pisiara E. Base Isolation technology for earthquake protection of art objects. *The 14th World Conference on Earthquake Engineering*, Beijing, China, 2008;
41. Chiozzi A, Simoni M, Tralli A. Rocking and overturning prevention for non-structural monolithic objects under seismic excitations through base isolation: a case

study in ferrara (Italy). *Proceeding of the 5th European Conference in Civil Engineering, ECCE 2014*, Florence, Italy, 2014.

42. Caliò I, Marletta M. Passive control of the seismic response of art objects. *Engineering Structures* 2003; 25:1009–1018.
43. Contento A, Di Egidio A. Investigations into the benefits of base isolation for non-symmetric rigid blocks. *Earthquake Engineering and Structural Dynamics* 2009; **38**: 849-866
44. Kirkpatrick P. Seismic measurements by the overthrow of columns. *Bulletin of the Seismological Society of America* 1927; **17** (2): 95-109.
45. Shi B, Anooshehpoor A, Zeng Y, Brune J. Rocking and overturning of precariously balanced rocks by earthquake. *Bulletin of the Seismological Soc. of America* 1996; **86**(5): 1364-71.
46. Arredondo C., Reinoso E. Influence of frequency content and peak intensities in the rocking seismic response of rigid bodies. *Journal of Earthquake Engineering* 2008; **12**(4):517-533.
47. Ishiyama, Y. Motions of rigid bodies and criteria for overturning by earthquake excitations. *Earthquake Engineering and Structural Dynamics* 1982; **10**(5):635 - 650.
48. Ishiyama, Y. Motions of rigid bodies and criteria for overturning by earthquake excitations. *Bulletin of the New Zealand Society for Earthquake Engineering* 1984*;* **17**(1), 24–37.
49. Psycharis N, Papastamatiou D, Alexandris A. Parametric investigation of the overturning of rigid blocks under dynamic loading. *12th European Conference on Earthquake Engineering,* London, U.K., 2002.
50. Zhang J, Makris N. Rocking response of free-standing blocks under cycloidal pulses. *Journal of Engineering Mechanics* 2001; **127**(5): 473-483.
51. Anooshehpoor A, Heaton T, Shi B, Brune J. Estimates of the ground accelerations at point Reyes station during the 1906 San Francisco earthquake. *Bulletin of the Seismological Society of America* 1999; **89**(4): 845–853.

52. Dimitrakopoulos E, DeJong M. Revisiting the rocking block: closed-form solutions and similarity laws. *Proceedings of the Royal Society of London* A Mathematical Physical and Engineering Sciences 2012; 468(2144): 2294–2318.
53. Dimitrakopoulos E, Paraskeva T. Dimensionless fragility curves for rocking response to near-fault excitations. *Earthquake Engineering and Structural Dynamics* 2015; **44**(12): 2015-2033.
54. Kafle B, Lam N, Gad E, Wilson J. Displacement controlled rocking behavior of rigid objects. J*ournal of Earthquake Engineering and Structural Dynamics* 2011; ***40****(15):1653:1669.*
55. Psycharis I, Fragiadakis M, Stefanou I. Seismic reliability assessment of classical columns subjected to near-fault ground motions. *Journal of Earthquake Engineering and Structural Dynamics* 2013; **42**(14): 2061:2079.
56. Zhu Z. Soon T. Toppling fragility of unrestrained equipment. *Earthquake Spectra* 1998; **14**(4)**:** 695–711.
57. Cai G, Yu J, Lin Y. Toppling of rigid block under evolutionary random base excitations. *Journal of Engineering Mechanics* 1995; **121**(8): 924-929.
58. Filiatrault A, Sullivan T. Performance-based seismic design of nonstructural building components: The next frontier of earthquake engineering. *Earthquake Engineering and Engineering Vibration* 2014; **13**(Sup. 1): 17-46.

Chapter 2: Rocking Response of Unanchored Building Contents

Summary

This paper investigates the rocking response of unanchored slender building contents. Although the rocking response of rigid blocks subjected to recorded ground motions has been studied extensively, the rocking response of contents located at various floor levels within a building has not been studied to the same extent. First, a four-story special concentrically braced frame (SCBF) was designed and modeled in OpenSees. Nonlinear time history analyses of the building model to a suite of 20 ground motions provided the horizontal and vertical floor accelerations at several locations on each story. These floor accelerations were then used to determine the rocking responses of contents with various size and slenderness values. The effect of the vertical component on the rocking response was examined and found to be insignificant. This means that the location of an object throughout a given story does not affect its response. The stockier blocks had increasing rocking responses higher up the building, as would be expected due to the larger floor accelerations. However, this result was less distinct for blocks of medium slenderness. Interestingly for slender blocks, variation in the height of the contents within the building had little effect on their rocking response. Finally, fragility curves were created using the normalized peak angle of rotation as the demand parameter and a physically motivated intensity measure based on the *PFV*, and block size and slenderness.

2.1 Introduction

The majority of the overall economic and life loss during most earthquakes can be attributed to the failure and damage of nonstructural components [1]. Nonstructural components are anything that is not included in the structural system of the building. This encompasses everything from ceiling tiles and sprinkler systems to the actual contents of the building, such as equipment and furniture. These nonstructural components normally comprise at least 80% of the total value of a building [2, 3]. After a seismic event a building may be structurally sound, but the failure of nonstructural components can render it unusable or even necessitate its demolition. Also, nonstructural damage can

occur at lower levels of shaking than structural damage and can lead to extensive downtime in essential facilities that are often at their greatest demand immediately following an earthquake [4].

One of the factors inhibiting the seismic design of building contents is that predicting their damage is very difficult because during an earthquake they can slide, twist, rock, bounce, impact walls or other objects, or even overturn [5]. Freestanding slender objects are prone to rocking. Rocking can lead to high internal accelerations that develop upon impact at the base, or even overturning, potentially resulting in damage or safety hazards [6]. Quantifying the response of these components is critical to making informed decisions during the design process in new buildings or during the seismic risk assessments of existing buildings.

The rocking response of rigid objects has been studied extensively since Housner's seminal paper [7] on the subject. These studies have been carried out using analytical pulse excitation and recorded ground motions for a variety of items, including ancient columns, electrical equipment, and art objects. However, the rocking response of an object located at some floor level in a building can be very different from that on the ground. One study which did examine the rocking response of building contents was done by Kamil and Tung [8]. They used a 5 story shear building with uniform story stiffness and floor mass to determine the accuracy of the energy balance equation proposed by Housner [7]. 72 rigid bodies with various size and slenderness were located at the different stories and the base was subjected to 200 artificial ground motions. The ground motions were scaled up until 50% of the blocks overturned. They found that the maximum of the resulting average pseudo-velocity spectrum was accurately predicted by Housner's equation at every story. They postulated that because in the low frequency range, the pseudo velocity response spectra is higher at the ground level than any floor, any block which is stable on the ground should be stable at any floor above it, especially for a stiff structure. They did not directly compare the response at different stories under the same base excitation.

The majority of work has also only considered the horizontal excitation. Past studies that did include the vertical component have reported varying conclusions concerning its significance. Makris and Zhang [9] showed that including the vertical component has negligible effect on the scaling factor required for a horizontal acceleration record to overturn a given block. In this study the vertical component was scaled with the same factor as the horizontal component. Yim et al. [10] found that inclusion of the vertical accelerations do significantly affect the rocking response but not in a predictable pattern. Dimentberg et al. [11] concluded that the presence of vertical motion, at a scale of 50% of the horizontal motion, increases the overturning probability by 30–40%. Shi et al. [12] found that the vertical component did affect the response at various levels of ground excitation but not significantly.

This paper investigates the rocking response of equipment and contents in a four-story hospital building designed for a location in Los Angeles. The rocking response of various contents is determined following a two-stage cascading analysis approach. In the first stage, a suite of 20 ground motions is selected and used to carry out nonlinear time history analysis of a 3D model of the building in OpenSees [13]. This analysis produces floor motions, which are then used in the second analysis stage as input to determine the planar rocking response of contents of different size and slenderness throughout the building. The rocking response of contents placed at various locations on each floor, where they are subjected to different vertical accelerations, is investigated. The likelihood of contents lifting off the floor due to the vertical excitations is also examined. The rocking response of contents located at different stories is evaluated and the effect of the content's height within the building is determined. Finally, fragility curves are provided to aid in the seismic design of nonstructural components that are susceptible to rocking. They predict the expected degree of rocking or overturning for a specific object given a level of floor excitation.

2.2 Building description

The hospital building assumed for the purpose of this study is located in Los Angeles (34.02197˚N, 118.28587˚W) and was designed as an essential facility on site class C soil

with an S_{DS} and S_{D1} of 1.23 and 0.56 [14]. The building is six seven-meter bays in one direction and four eight-meter bays in the orthogonal direction for a total footprint of 1344 m^2. All four stories are 4.5 m tall. It was designed as a special concentrically braced frame (SCBF) in accordance with ASCE 7-10 [15]. The steel members were designed in compliance with AISC 360-10 [16]. Elevation and plan views of one of the modeled bays are shown in Figure 2-1. Member sizes can be found in Appendix B.

The lateral force resisting system consisted of HSS bracing in the center two exterior bays of all four sides. The chevron bracing was designed using the equivalent lateral force procedure with a force reduction factor of 6 and a drift limit of 1.5%. Chevron bracing can lead to a soft story formation when the compression brace buckles if the beam forms a plastic hinge at the brace connection point. Zipper columns were used to avoid the need for excessively large beams. Zipper columns prevent the onset of a soft story and distribute the yielding over several stories [17, 18]. These columns were designed according to the static design method proposed by Kim et al. [19].

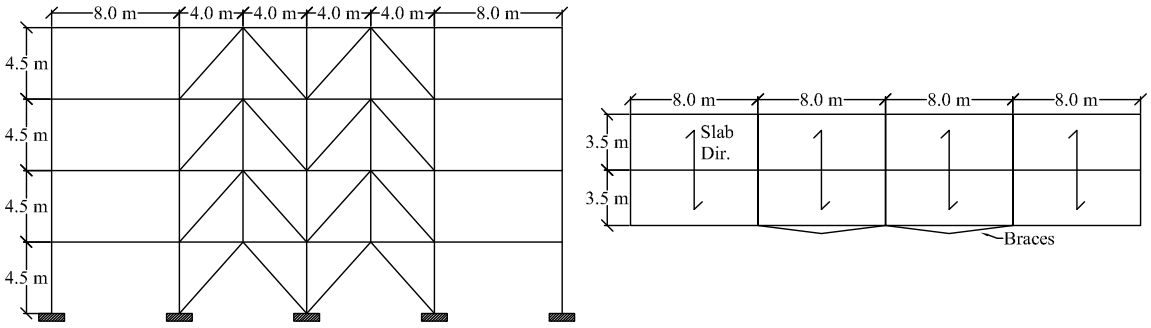

Figure 2-1. Left: Elevation view of SCBF. Right: Plan view of modeled bay.

A one-way slab orientated in the direction of the shorter 3.5 meter span was used at each story. Double span slabs were used making it appropriate to model one full bay width. A ribbed steel and concrete deck was used with 18 gauge (1.2 mm) steel decking and a 125 mm thick concrete slab. All the floors were assumed to be equally loaded with a dead load of 4.0 kPa and a live load of 2.5 kPa. A cladding load of 0.96 kPa was also applied to the exterior.

2.3 Structural model

A 3D model of one bay width of this hospital was created in OpenSees [13]. OpenSees is a software environment for modeling earthquake simulation of structural systems that was used in this study to run seismic time history analysis on the SCBF. The frame was modeled using the expected properties of the members and their materials. The gravity loads were applied as static loads on the column nodes and were taken as the force of gravity acting on the mass tributary to the respective columns. The remainder of the gravity load for each story was applied on a leaning column to account for P-delta effects.

The seismic mass applied to the frame was taken as the mass attributed to the full dead and live gravity loads, as in [20]. Half the horizontal mass of the building was tributary to the braced frame on each side since the building is only braced at the exterior of the building. The mass on the slab was applied as a mass density and acted in all translational directions. The mass due to cladding was applied in the horizontal and vertical directions to the exterior column nodes. The remainder of the horizontal mass was lumped at each story on the leaning column. The columns in the unbraced frame also had their tributary vertical mass associated with the half bay width that was not modeled applied at each story.

All the members except the braces were structural W-sections and modeled using force based nonlinearBeamColumn elements. These elements used distributed plasticity and were comprised of 16 fibers along the length of the web and flanges and 4 fibers across the thickness. The steel was modeled using the uniaxial isotropic Steel02 material with the expected yield strength of $f_{y,e}$ = 379 MPa and 3% strain-hardening [13]. The torsional stiffnesses of the beams and columns were then aggregated to the fiber sections.

A different square HSS section was used for the braces at each level of the building. The braces were modeled using force based nonlinearBeamColumn elements with seven integration points and a corotational geometric transformation. Both the flanges and webs of the HSS sections were divided into 16 fibers along their length and 4 fibers across their thickness. The same material was used as for the other members except with an expected yield strength of $f_{y,e}$ = 345 MPa. The braces were given an initial camber of L/500 (12

mm) at the center by aligning their elements along a half sinusoidal curve, as recommended by Hsiao et al. [21]. Each brace comprised was of 6 elements with the center four elements being $L/16$ in length to accurately capture the buckling. Figure 2-2 shows the hysteresis of a first story brace. The braces were fixed to the column and mid-beam nodes in the translational and out of plane rotational degrees of freedom.

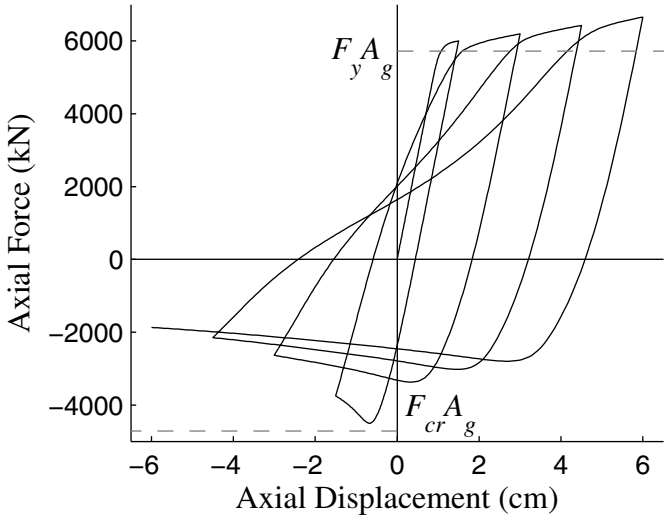

Figure 2-2. First story brace hysteresis.

The in plane rotation was modeled as a gusset plate according the moment-rotation relation given by Hsiao et al. using a zero length rotational spring element [21]. The braces were constrained to buckle entirely in the braced frame plane. The HSS braces were fairly stocky (L/r = 51 – 92) resulting in the 'full' hysteresis ensuring high-energy dissipation during an earthquake.

The slab was modeled in OpenSees using ShellMITC4 elements. The slab was divided into square elements using 8 and 32 elements in the out of plane direction and in plane directions, respectively. The translational degrees of freedom of the slab were fixed at every column, but the rotational degrees of freedom were not restrained (i.e. they were free to rotate). The deck was modeled using an elastic orthotropic material with a constant thickness. The material properties and thickness of the shell element were selected to match the orthotropic properties of the corrugated deck slab using the equivalent orthotropic material modeling method [22]. This method works by equating the bending

stiffness of the actual slab to that of the model in the longitudinal and perpendicular directions as well as the axial stiffnesses in the longitudinal direction and the shear stiffnesses in the slab's plane. These conditions are shown in Equations (2.1) – (2.4). The stiffnesses were calculated in accordance with ANSI/SDI C-2011 using the cracked concrete section properties [23]. The elastic and shear moduli of the concrete were taken as 17.3 and 7.52 GPa respectively. The Poison's ratio values are assumed to be zero, which neglects the coupled effects in different directions and is consistent with literature for cracked concrete [24, 25]. The out of plane elastic modulus, E_y, and the two out of plane shear modulus's, G_{xy} and G_{yz}, are taken as relatively small in relation to the other directions [22]. The four equations are solved for the four unknowns; d_s, E_z, E_x, and G_{xz}, where d_s and b_s are the depth and unit width of the slab respectively. The depth of the slab was taken as 129 mm and the equivalent orthotropic material properties are shown in Table 2-1.

$$E_z \frac{b_s d_s^3}{12} = E_c I_{cr,z} \quad E_x \frac{b_s d_s^3}{12} = E_c I_{cr,x} \quad E_z b_s d_s = EA \quad G_{xz} d_s = Gt \quad (2.1 - 2.4)$$

where,

Z – Parallel to ribs, In the braced frame plane

X – Perpendicular to ribs, Out of the brace frame plane

Y – Vertical direction

Table 2-1. Orthotropic material properties for steel and concrete deck slab.

Elastic Modulus	Shear Modulus
E_x = 6.53 GPa	G_{xy} = 0.75 GPa
E_y = 1.73 GPa	G_{xz} = 2.51 GPa
E_z = 8.57 GPa	G_{yz} = 0.75 GPa

There are several simplifications in this model, including that the deck slab is assumed to be purely elastic with the same bending stiffness under both hogging and sagging moments. It also assumes that the concrete slab is already fully cracked at the start of the earthquake due to gravity loading. However, in lieu of a more sophisticated

and computationally expensive model, equivalent stiffness methods are capable of accurately modeling orthotropic decks under dynamic loading [22, 26].

The girders, beams and joists were fixed to the slab along their lengths. The beams in the braced frame plane were allowed to rotate independently of the slab at the columns. The bases of all ten columns were fully fixed in all 6 degrees of freedom. The entire plane containing the unbraced frame was also constrained in the out of plane direction to ensure the frame only responded in the horizontal direction of excitation and vertically. The leaning column was also constrained against motion in the out-of-plane direction. In order to avoid torsion in the model, as only one side is braced, the rotational and in-plane horizontal translational degrees of freedom of the corresponding columns nodes in each plane were equated at each level.

Five percent Rayleigh damping was applied at the first vertical and horizontal modes. The time step used in analysis was taken as a tenth of the time step of the ground motion record. This small time step was used to minimize fictitious spikes in the floor acceleration due to system nonlinearities. These exaggerated floor acceleration spikes occurred in the SCBF when the braces first buckled in compression but were virtually eliminated by the use of a small time step.

2.4 Fundamental building properties

The periods of the modeled frame as calculated using elastic eigenvalue analysis are shown in Table 2-2. Horizontal modes are defined as modes that react primarily in the lateral direction and are in good agreement with the periods and mode shapes of an eigenvalue analysis using only horizontally activated mass.

Table 2-2. Periods of the SCBF.

Horizontal		**Vertical**	
Period	Mode	Periods	Modes
0.46 s	13	0.60 – 0.47 s	1 - 12
0.21 s	38	0.41 – 0.22 s	14 - 37
0.13 s	74	0.21 – 0.15 s	39 - 73

The first 12 modes are full-bay by full-bay deflections of the slabs. The first period of the slab is somewhat large, at 0.6 s, which is a result of using the mass accredited to the full dead and live loads and the cracked section properties of the slab. The primary horizontal period of the building is 0.46 s, which is close to the code predicted period of 0.43 s [15].

A static pushover test was performed using an inverted triangle force distribution over the height of the building to represent the first mode. The resulting capacity curve is shown in Figure 2-3. The base shear coefficient is defined as $C_S = V/W$, where V is the base shear and W is the total weight of the structure, 37500 KN. The design base shear coefficient, $C_{S,Design}$, was computed from ASCE 7-10 as:

$$C_{S,Design} = \frac{S_{DS}}{\left(\frac{R}{I_e}\right)} < \frac{S_{D1}}{T\left(\frac{R}{I_e}\right)} = 0.29 \tag{2.5}$$

where R is the force reduction factor, I is the importance factor, and T is the natural period. The observed base shear coefficient before any brace buckles is 0.58 giving a system overstrength factor of 2 at yield.

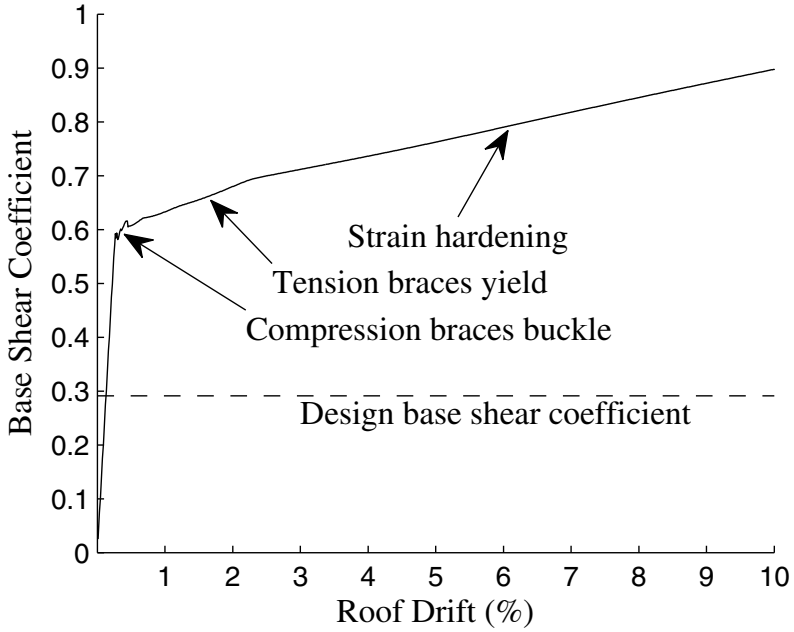

Figure 2-3. Capacity curve of modeled frame.

The capacity curve shows the strength loss due to buckling of the braces, which is quickly recovered. The second story braces buckle first at 0.27% roof drift. They are immediately followed by the buckling of the rest of the stories in the order: third story (0.30%), fourth story (0.36%), and first story (0.46%). The zipper columns distribute the unbalanced vertical forces at the center of the beam causing compression in the braces at the level above leading to their buckling. This rapidly progresses up the structure and is the reason for the name 'zipper' column. The second story braces yield in tension at 0.40% roof drift, shortly before the first story braces buckle, followed by the third story (0.65%), first story (1.15%) and fourth story (2.20%). The capacity curve continues to gain strength even after all the braces have yielded due to the assumed 3% strain-hardening in the members which exceeds any P-delta effects out to 10% roof drift. It should be noted that the curve is not accurate out to such large drifts as the model does not take into account any stiffness degradation in the members. Also, during a seismic event the order of yielding is expected to differ due to the dynamic distribution of forces.

2.5 Ground motion selection and scaling

A suite of 20 ground motions was selected for the time history analysis. All the records were selected from Baker's broadband suite set 1a [27]. This suite consists of 40 unscaled ground motions, all of which include fault normal, fault parallel and vertical components. Baker selected these motions to match the target spectrum and log variance predicted by Boore and Atkinson's ground motion prediction equation [28] for a magnitude 7 strike-slip earthquake at 10 km on a soil site. The site location had a soil class C (v_{s30} = 365 – 760 m/s) while the earthquakes selected had shear wave velocities from 200 – 400 m/s. A disaggregation of the seismic hazard at the hospital site for the spectral period of the fixed-base building shows that the vast majority of the contribution is from magnitude 6.5 – 7.5 earthquakes at 5 – 15 km [29]. Overall, this makes Baker's set 1a an ideal suite to select ground motions for time history analysis from. A table of the ground motions selected and their characteristics is given in Appendix C.

The individual response spectra for all 80 horizontal ground motion components were then computed and scaled to the design spectrum to minimize the sum of the square of the

difference between them over a period range of 0 to 4 s. The twenty horizontal components with the least minimum residual error were selected for time history analysis. A maximum of one horizontal component per record was used. The horizontal response spectra of the resulting suite as well as the mean and design spectrum are shown in Figure 2-4 (left). The vertical components were scaled with the same factor as the corresponding horizontal components. The vertical response spectra are shown in Figure 2-4 (right).

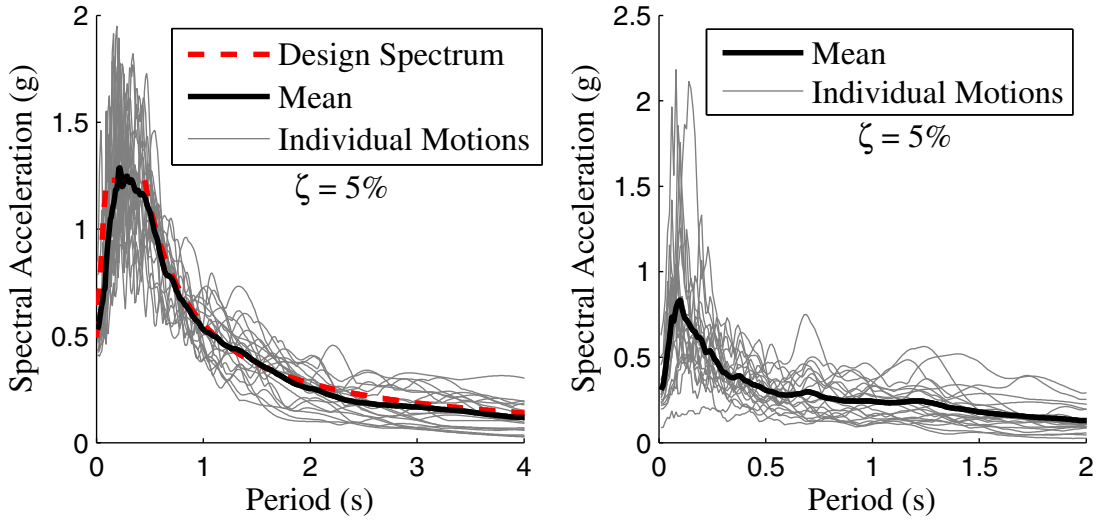

Figure 2-4. Scaled ground response spectra for 20 selected earthquakes.
Left: Horizontal Spectra. Right: Vertical Spectra.

2.6 Building response

The 20 ground motions were then used to determine the floor accelerations at various locations on each level. The vertical accelerations in the unbraced bays were found to be the most critical, because the vertical displacement of the slab in the braced bays was restrained along the one edge by the zipper columns and braces, and thus these locations were examined in further detail. Figure 2-5 shows a floor plan of the one bay width that was modeled depicting the 5 locations where the accelerations were recorded.

Figure 2-6 shows the mean responses of the frame for the 20 ground motions. The mean maximum interstory drift was largest between the second and third stories as expected from the pushover analysis. The second story braces buckled first in the majority of the analysis leading to larger interstory drifts. However, the zipper columns

prevented excessive drift from accumulating at this level and assisted in distributing the ductility demand to the first and third stories.

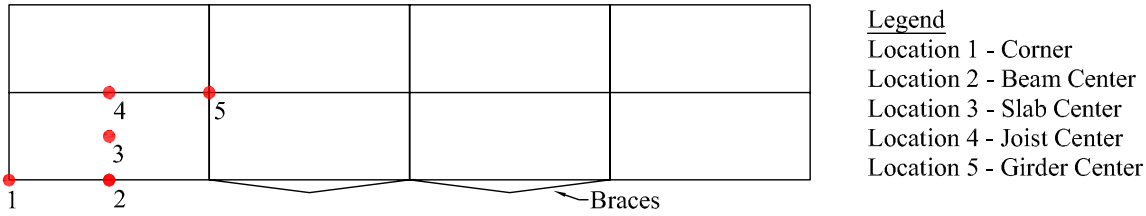

Figure 2-5. Floor plan locations where the acceleration time histories were recorded.

The mean horizontal absolute peak floor velocity (*PFV*) increases nearly linearly with building height from a mean of 0.55 m/s at the ground to 1.01 m/s at the roof. The mean absolute peak floor acceleration (*PFA*) also increases with building height to a maximum of 10.2 m/s^2 at the roof. The mean vertical *PFA*s increased with building height as well. The center of the bay (location 4) had the largest vertical *PFA* at each story level followed by the center of the slab (location 3), the midspan of the beams in either direction (locations 2 and 5), and the corner (location 1). This distribution was expected based on the primary vertical mode shape displacements of the slab. The vertical accelerations were amplified from the corner near the column to the center of the bay by a factor of 2.0 which is consistent with the experimental findings of a base-isolated hospital tested using the E-Defense shake table which recorded increases between 1.8 and 2.6 [30].

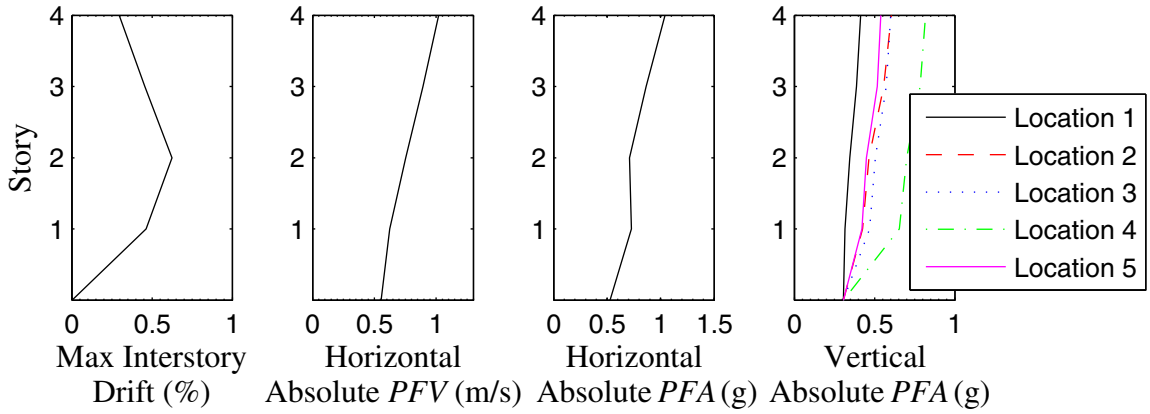

Figure 2-6. Mean building responses.

The mean horizontal floor spectra for each floor are shown in Figure 2-7 (left). The peaks are located at a slightly longer period than the natural period, 0.46 s, due to period elongation from yielding. Figure 2-7 (right) shows the vertical response spectra at the roof for the various floor locations. The spectra at the other stories have similar shapes with lower spectral accelerations. Locations 3, 4, and 5 have peaks at the primary vertical periods, 0.47 - 0.60 s. However, all the locations have a higher spectral acceleration at around 0.1 s which corresponds to the mean peak spectral acceleration of the vertical component of the ground excitations.

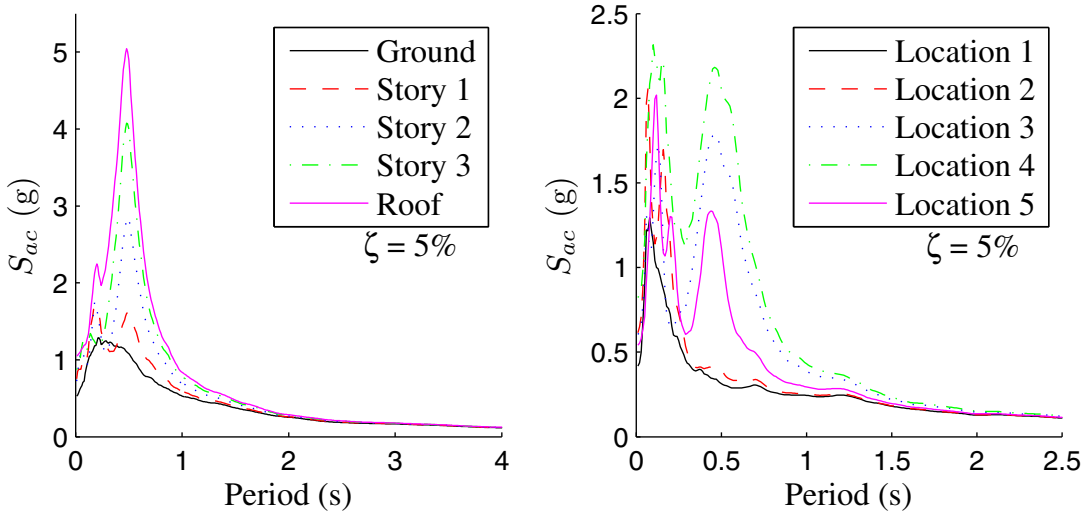

Figure 2-7. Left: Horizontal floor response spectra at each story. Right: Vertical floor response spectra at various locations on the roof.

2.7 Review of the rocking block

A building content, as shown in Figure 2-8, will enter into rocking motion about its corners given sufficient base acceleration and adequate friction to prevent sliding.

$$\left|\ddot{U}_f^x\right| \geq \left(g + \ddot{U}_f^y\right)\tan\alpha \tag{2.6}$$

where $\ddot{U}_f^x$ and $\ddot{U}_f^y$ are the horizontal and vertical floor accelerations respectively, g is the gravitational constant, and α is the slenderness of the block as shown in Figure 2-8. The equation of motion for a rigid rocking block under horizontal excitation was first derived by Housner in 1963 [7]. It has since been extended to include vertical base excitation as shown compactly in Equation (2.7) [10-12]. The nonstructural contents under

consideration in this paper are treated as essentially rigid objects that do not deform during the rocking motion. This assumption was shown to be accurate by Konstantinidis in a set of shake-table tests on various types of laboratory equipment [31]. This study also only considers pure planar rocking and the dynamic interaction between the blocks and building is neglected due to the assumed difference in masses.

$$\ddot{\theta} = -p^2 \left\{ \left(\frac{\ddot{U}_f^y}{g} + 1 \right) \sin\left(\mathrm{sgn}(\theta)\alpha - \theta\right) + \frac{\ddot{U}_f^x}{g} \cos\left(\mathrm{sgn}(\theta)\alpha - \theta\right) \right\} \tag{2.7}$$

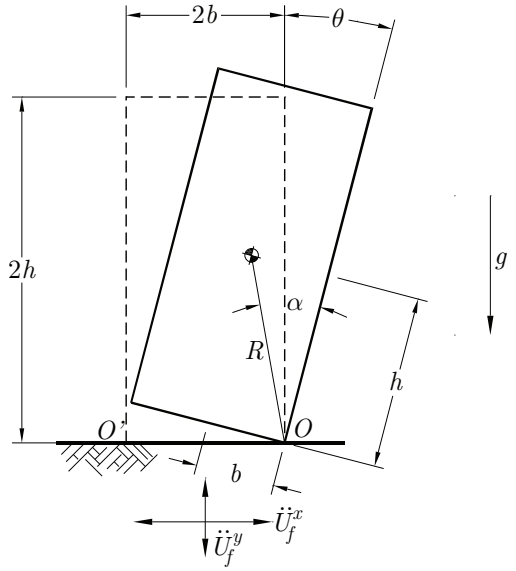

Figure 2-8. Rocking rigid block.

The frequency parameter, $p = \sqrt{3g/4R}$ where $R = \sqrt{h^2 + b^2}$, is constant for a given block and describes the block's dynamic characteristics. The period of vibration of a block is not constant but depends on the vibration amplitude. However, under free vibration, a larger block having a lower *p* will oscillate slower than a smaller block with the same slenderness given the same initial conditions. The slenderness of the block has a large impact on the rocking motion with stockier blocks being significantly more stable [6]. However, the relationship between slenderness and stability is highly nonlinear and under certain conditions slender blocks can survive motions that topple stockier blocks. Housner discovered a scale effect in which larger blocks with the same slenderness ratio were more stable than smaller blocks [7]. Also, the same block, which remains stable

under an intense pulse of short duration, may tip under a longer pulse of lower acceleration amplitude [32].

In order for the block to smoothly translate from pivoting on either edge the angular momentum must be conserved. This requires that the rocking block lose energy every time it makes contact with the base. This loss is defined through the classical concept of a coefficient of restitution, *e*, taken as the ratio of angular velocities immediately before and after the impact,

$$e = \frac{\dot{\theta}_2}{\dot{\theta}_1} \tag{2.8}$$

The maximum coefficient of restitution, corresponding to the minimum energy loss, that meets this requirement, is [7]:

$$e = 1 - \frac{3}{2}\sin^2\alpha \tag{2.9}$$

The ordinary differential equation of motion for the rocking block is solved by integration in Matlab [33] using the ODE solvers. The state vector, $y(t)$, and time derivative vector, $\dot{y}(t)$, are shown in Equations (2.10) and (2.11) respectively.

$$\mathrm{y}(t) = \begin{pmatrix} \theta(t) \\ \dot{\theta}(t) \end{pmatrix} \tag{2.10}$$

$$\dot{\mathrm{y}}(t) = \begin{pmatrix} \dot{\theta}(t) \\ -p^2\left\{\left(1+\frac{\ddot{U}_f^y(t)}{g}\right)\sin\left(\mathrm{sgn}\left(\theta(t)\right)\alpha-\theta(t)\right)+\frac{\ddot{U}_f^x(t)}{g}\cos\left(\mathrm{sgn}\left(\theta(t)\right)\alpha-\theta(t)\right)\right\} \end{pmatrix} \tag{2.11}$$

The inclusion of vertical ground accelerations enables the possibility that the block may lift off of the surface on which it is rocking, rendering the rocking equations of motion invalid. In order to detect this potential scenario, the vertical force at the rocking edge of the rigid block is determined at every time step. The vertical normal force, F_y, is given by

$$F_y = m\left\{\mathrm{sgn}(\theta)R\ddot{\theta}\sin\left(\alpha-|\theta|\right)-R\dot{\theta}^2\cos\left(\alpha-|\theta|\right)+\ddot{U}_f^y+g\right\} \tag{2.12}$$

where m is the mass of the block. If this becomes negative, the block jumps, and the analysis is stopped. A derivation of this reaction force is shown in Appendix A.

2.8 Results and discussion

2.8.1 Introduction to rocking spectra and an example response

The rocking time histories were determined for objects at each floor location for all the stories using Matlab. Rocking time histories were found for 120 different blocks ranging from R = 7.5 cm – 11.9 m and with slenderness of 10° (ex. bookcase), 15° (ex. upright desktop computer), and 20° (ex. 4 drawer filing cabinet). The rocking time histories for a common refrigerator ($2b$ = 0.6 m, $2h$ = 1.8 m, α = 18.4°, p = 2.8 rad/s) subject to the floor accelerations at the corner of the building under the 1979 Imperial Valley Brawley Airport fault parallel record are shown in Figure 2-9. Interestingly, the fridge on the third story overturns, while the fridge on the roof does not. This is a product of the high nonlinearity involved in both the building and rocking responses. Also clearly visible is that the rocking frequency is not constant but depends heavily on the rocking amplitude.

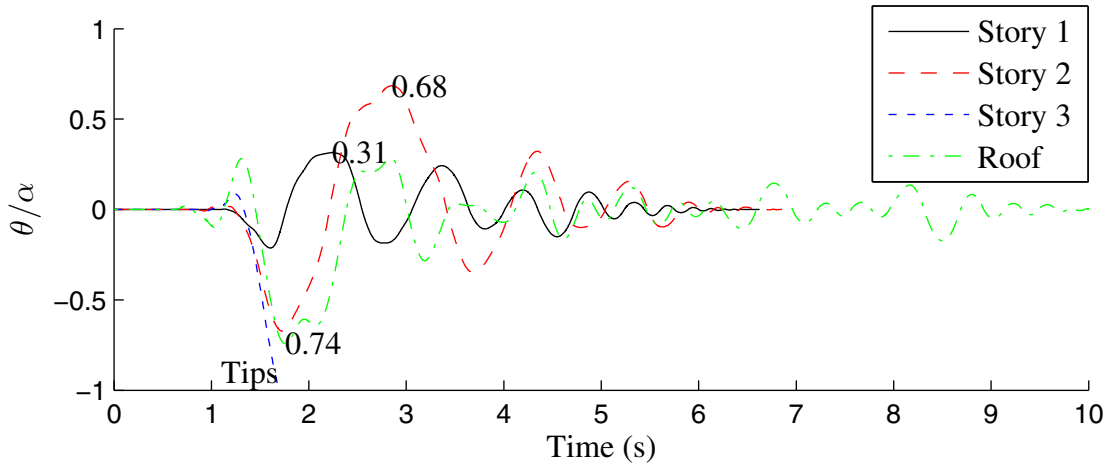

Figure 2-9. Example rocking response of a fridge located near a column.

Typically only the maximum value of rotation from the rocking time history is of interest. When many analyses are done with the same time history for many different size and slenderness blocks, the results are often shown as a rocking spectrum. A rocking spectrum plots the block's size in the form of $2\pi/p$ as the independent variable versus the maximum angle of rotation normalized by the slenderness of the block as the dependent

variable. Different slenderness values are shown as separate lines. The maximum angle of rotation for blocks that tip is taken as α to avoid skewing the mean when the rocking spectra for the 20 ground motions are averaged out for a given location in the building.

2.8.2 Probability of jumping

As expected, occurrences of jumping were more prevalent at the higher stories because of the higher vertical floor accelerations. The frequency parameter, and therefore size, did not have an effect on the probability of jumping. The percentage of earthquakes that caused jumping in each location is shown in Figure 2-10. There were no instances of jumping at the corner or anywhere on the ground. Jumping was most likely at the floor locations with the highest vertical *PFAs* as shown in Figure 2-6 (right). The slenderness of the block did not matter for most instances although where there were differences the stockier blocks tended to be more prone to jump. The few jumping results make it difficult to draw any definitive conclusions on this. Any analysis that resulted in jumping was omitted from the following rocking results. The implication of this is that the following rocking spectra in areas of high vertical acceleration are based on slightly fewer analyses.

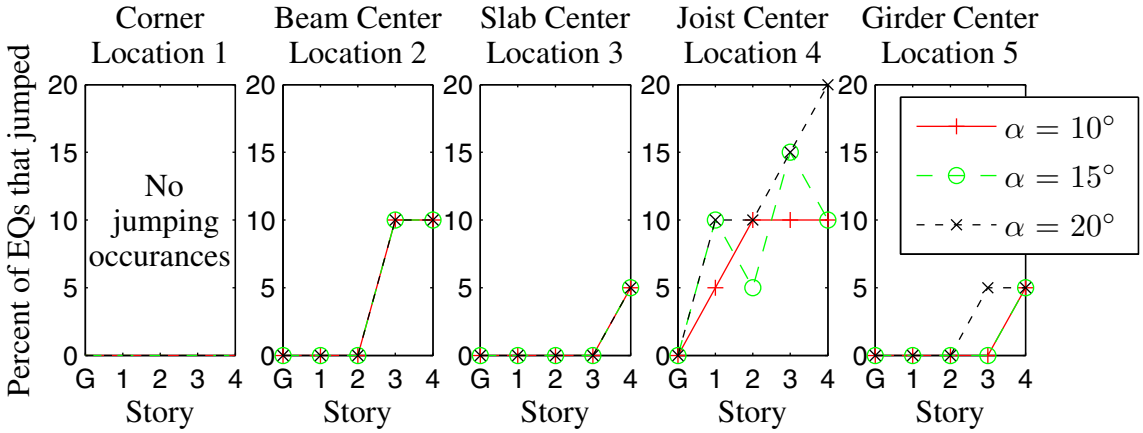

Figure 2-10. Percentage of the earthquakes for which jumping occurred.

2.8.3 Effect of vertical acceleration

One objective of this study was to determine how the vertical floor accelerations contributed to the rocking response. To analyze this effect, rocking spectra were created in Matlab using only the horizontal floor accelerations. These were then compared to the

original rocking spectra which were calculated using the vertical component as well. This comparison is shown in Figure 2-11 for the rocking spectra at location 4 (center of the joist) for the ground, second story, and the roof. The joist was selected as it had the highest vertical *PFA* as well as the highest vertical floor response spectra as shown in Figures 6 and 7. These graphs show that the vertical acceleration has minimal effect on the rocking response regardless of size, slenderness or story. The vertical accelerations at the center of the joist were substantial, even producing jumping in a few cases, and yet did not affect the magnitude of rocking response that the contents. All the other floor locations had even less difference in the spectra. Although this has been noted in literature before, the result is still counterintuitive. Shi et al. [12] explained this phenomenon using the equation of motion given in Equation (2.7). They postulated that the reason that vertical acceleration is not significant for slender blocks is that in the equation of motion the horizontal and vertical ground acceleration components are respectively multiplied by the *sine* and *cosine* of the difference between the slenderness, α, and the rocking angle θ [12]. This results in the horizontal excitation having a much larger influence on the angular acceleration of the block and therefore its rocking response.

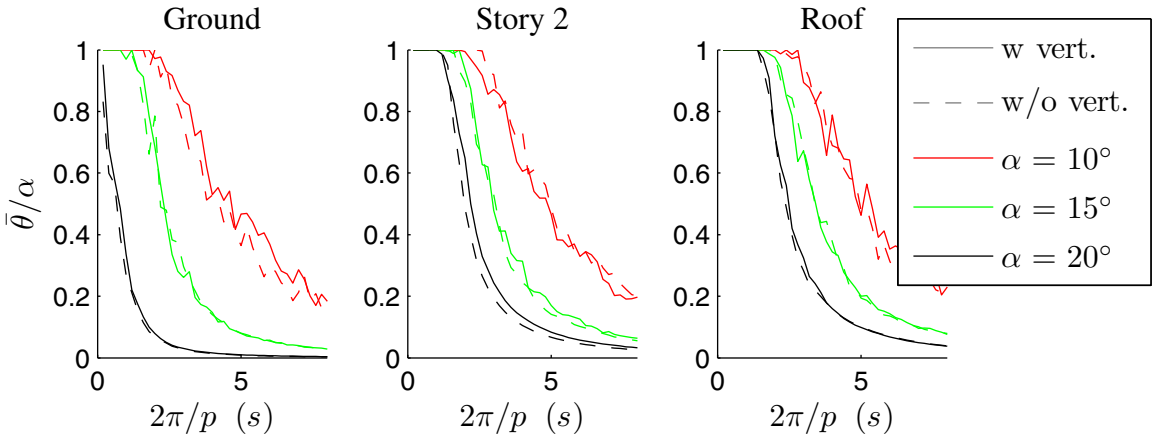

Figure 2-11. Effect of the vertical acceleration component on the rocking response.

Notably, locations where the highest vertical accelerations occurred, i.e. the roof, corresponded to locations of highest horizontal accelerations as well (i.e. horizontal

accelerations continued to dominate). Where the horizontal accelerations remained the same at a given story and the vertical accelerations increased towards the center of the bay the effect of the vertical acceleration on the rocking response was found to increase. Overall though, even in the most extreme cases the differences in the rocking spectra when including vertical accelerations or not is negligible.

2.8.4 Effect of content placement on a particular floor

Figure 2-12 shows the average rocking spectra for the 20 ground motions at the roof for the different floor locations. It can be observed that the location of a block on the floor does not affect its rocking response. The result was similar for the other stories.

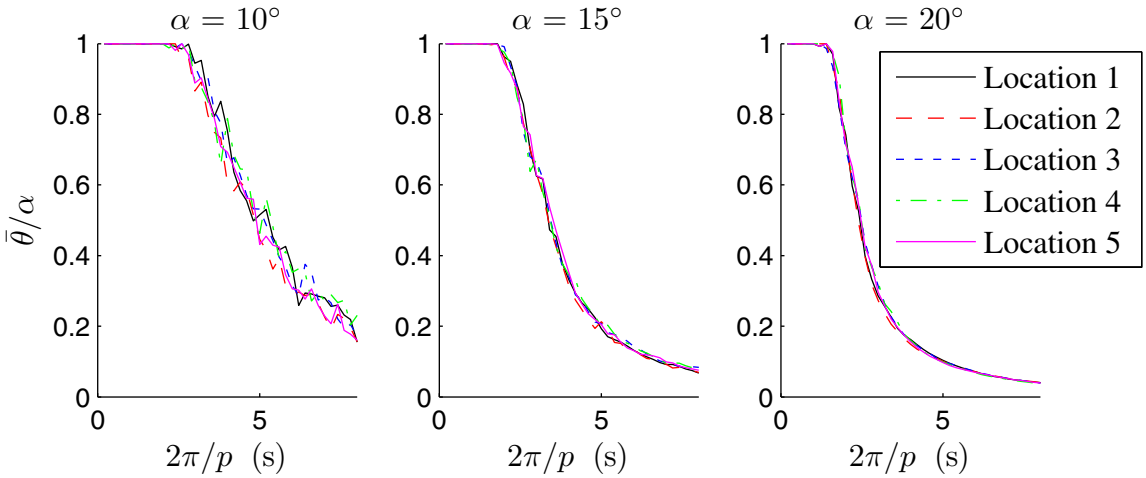

Figure 2-12. Rocking spectra at different locations on the roof.

This is expected from the previous section, which showed that vertical accelerations had minimal effect on the rocking response. An important conclusion is that it is not necessary to know the location of a piece of equipment on a particular floor level or the vertical accelerations at that level to be able to accurately predict the content's rocking response.

2.8.5 Effect of floor level

Also of interest is the difference in the rocking response from one story to another. Since the placement on the floor had minimal effect on the rocking spectra the analysis is determined using the results at the corner of the building. The floor accelerations increase

higher up the building which is expected to increase the rocking response. This was the situation for stockier blocks (α = 20°) as shown in Figure 2-13 (right). The rocking response increased with increased height within the building. The largest difference between stories was between the ground and the first story. The difference between adjacent stories decreases up the building ending in minimal difference between the third story and the roof. However, transitioning from stocky contents to more slender contents this result becomes less evident. At a slenderness of 15°, Figure 2-13 (center), the rocking response still increases from one floor to the next but the differences are less pronounced. For slender blocks with α = 10°, Figure 2-13 (left), the relative height of the content in the building has little impact on the rocking response. This result is generally consistent for each individual motion as well.

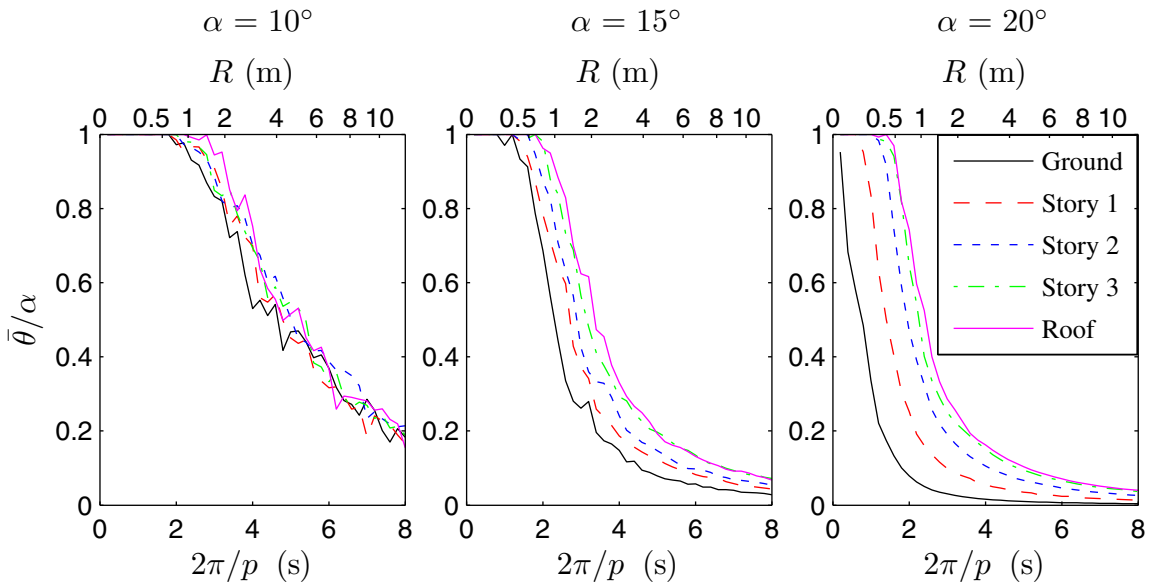

Figure 2-13. Rocking spectra for all stories at the corner.

The shape of the rocking spectra also changes for contents with different slenderness values. The slender rocking spectra have a fairly linear decrease in the rocking response with increasing block size whereas the spectrum for stockier blocks exhibits a size zone where the rocking response rapidly decreases for increasing sizes. This zone aligns with the typical size of building contents or equipment which may be susceptible to rocking, e.g. varying from R = 0.1−2 m ($2\pi/p \cong$ 0.75−3.5 s). The other values are given to show

the full spectra and for the benefit of extreme cases. This means that a slight change in size for typical building size contents is expected to have a larger impact on stockier objects. The average and individual rocking spectra for the stockier blocks are also smoother meaning that the rocking response is more sensitive to small input changes for slender blocks. However, this is due in part to the fact that the maximum coefficient of restitution is used in the analysis. In rocking spectra this coefficient is analogous to damping for response spectra [34]. The slender blocks have a higher maximum coefficient of restitution, see Equation (2.9), and thus less 'damping'. Figure 2-14 shows the average slender spectra (α = 10°) for a coefficient of restitution of 0.84, similar to the maximum for the stocky blocks. The rocking response is reduced as expected and the jaggedness of the spectra has almost disappeared. However, there is still no substantial difference between stories 2 through the roof although the first story response is noticeably lower.

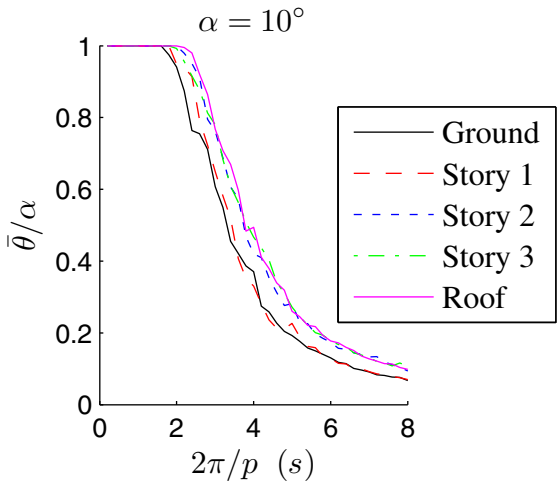

Figure 2-14. Slender (α = 10°) rocking spectra with coefficient of restitution e = 0.84.

Figure 2-15 shows the average maximum angle of rotation plotted against the building height for contents with slenderness α = 10°, 15° and 20° and size R = 0.5, 1 and 2 m. This figure confirms the previous conclusion with the slender lines being nearly vertical, i.e. the placement of the content up the height of the building has little effect on its peak rocking response. Smaller blocks have a large difference between slendernesses at the

ground but very similar at the roof, where they usually overturn. The small stocky blocks had the largest increase in response over the building height. There is a small difference between the responses of the stocky blocks at the ground, but the difference increases with height, whereas for the slender and semi-slender blocks the difference between sizes was fairly uniform over the stories for the sizes plotted.

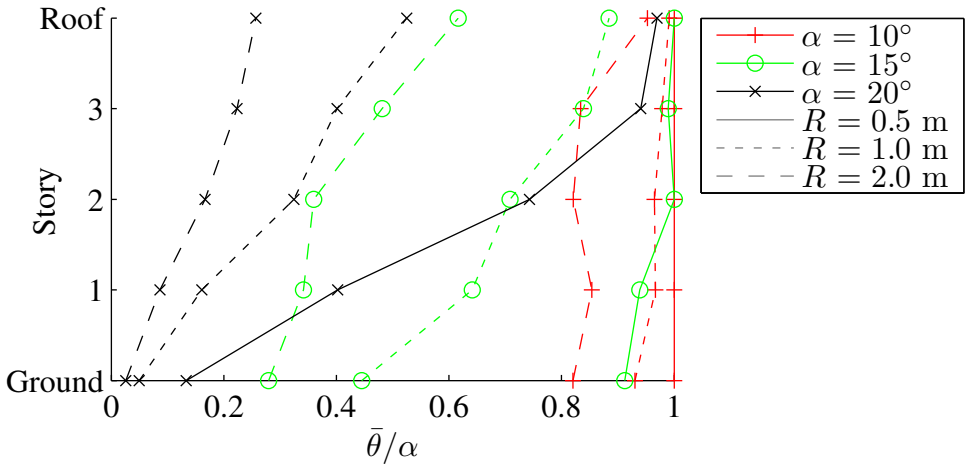

Figure 2-15. Height v. normalized rocking angle for select block sizes.

2.9 Analytical seismic fragility curves

A fragility curve is a seismic risk assessment tool which is used to relate a building component's probability of failure to a level of shaking. More specifically, it is the probability that a demand parameter (*DP*) will exceed a certain limit state (*LS*), *c*, for a given intensity measure (*IM*). Here the demand variable of interest is the rocking response and the intensity on which it is conditioned is the floor motion.

2.9.1 Intensity measure

The rocking response of a rigid block is controlled not only by the intensity of the floor motion but also by its slenderness and size. Thus, an appropriate *IM* should include all these parameters. A convenient dimensionless *IM* as proposed by Dimitrakopoulos and Paraskeva [35] is

$$IM = \frac{pPGV}{g\tan(\alpha)} \tag{2.13}$$

They found this to be the most proficient univariate *IM* from a number of options that they investigated under both pulse-type motions and records that had synthetic high frequency components combined with the pulses. This study uses the *PFV* in lieu of the *PGV*. This *IM* contains all the governing parameters and allows for the development of universal fragility curves. The intensity measure is based on the absolute *PFV* and not the *PFA*. This is in line with previous literature that has shown that the peak rocking response is primarily governed by the velocity characteristics of the excitation, and not the acceleration [35 - 37].

2.9.2 Demand parameter

The *DP* is simply taken as the maximum absolute value of rotation scaled by the slenderness, $DP = |\theta| / \alpha$. This *DP* is dimensionless, typically used in rocking fragility analysis, and has a straightforward physical meaning. *DP* values of greater than 0 indicate the initiation of rocking while values greater than 1 show overturning. Although several studies have pointed out that it is possible for $|\theta|$ to exceed α without overturning [38, 39], this situation is uncommon and represents an unstable block. Values between 0 and 1 indicate safe rocking where the content rocks and then returns to its initial position. This *DP* consequently lends itself to meaningful *LS*s as shown in Table 2-3. The initiation of rocking was not included as a *LS* because it can be calculated deterministically using the *PFA* with Equation (2.6). Also, this threshold is not dependent on the size of the block or the *PFV* and therefore does not correlate well with the intensity measure used. The first *LS* was taken as 0.1, which is indicative of minor rocking and potential local damage [35]. The second *LS* was taken as the value for which the rate of change of the period of free vibration, T_{fv}, in Housner's equation of rocking motion, Equation (2.14), begins to increase. This is the inflection point of Housner's equation for the apparent period plotted against θ_0/α and was solved by finding the root of the second derivative as shown in Equation (2.15). The third *LS* was taken as overturning.

$$T_{fv} = \frac{4}{p}\cosh^{-1}\left(\frac{1}{1-\theta_0/\alpha}\right) \tag{2.14}$$

$$\text{At inflection point}: \frac{\partial^2 T_{fv}}{\partial\left(\theta_0/\alpha\right)^2} = 0 \qquad \frac{\theta_0}{\alpha} = 1 - \frac{\sqrt{2}}{2} \approx 0.3 \tag{2.15}$$

Table 2-3. Limit states

Limit State	*DP* Threshold Value	Meaning
LS_1	$\lvert\theta\rvert/\alpha = 0.1$	Minor Rocking
LS_2	$\lvert\theta\rvert/\alpha = 0.3$	Inflection Point
LS_3	$\lvert\theta\rvert/\alpha = 1.0$	Overturning

2.9.3 Regression analysis

The *DP* and the *IM* were both assumed to be random variables with lognormal distributions. The other typical assumption that was made is that the *DP* and the *IM* follow the relation shown in Equation (2.16) where *Z* is a lognormally distributed random variable.

$$DP = \rho IM^{\gamma} Z \tag{2.16}$$

Consequently, when plotted on the ln(*DP*) versus ln(*IM*) plane, this relation becomes linear (Equation (2.17)) and ρ and γ can be estimated using ordinary least squares regression. Only the safe rocking results were used in this analysis. Figure 2-16 shows the safe rocking results for all the stories plotted on this plane with the line of best fit.

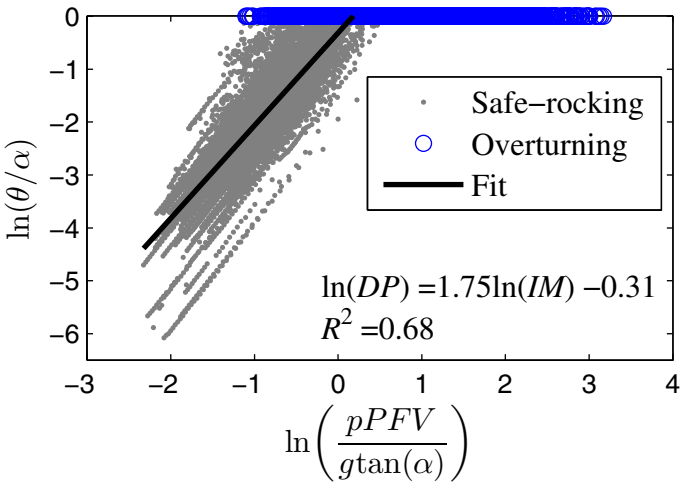

Figure 2-16. Safe rocking results showing linear relation between ln(*IM*) and ln(*DP*).

The overturning results have also been plotted, however this data was not used in this analysis. The relation between ln(*DP*) and ln(*IM*) is found to be linear with an R^2 of 0.68 and regression parameters of $\rho = 0.73$ and $\gamma = 1.75$.

$$X = \ln(DP) = \ln(\rho) + \gamma \ln(IM) + \ln(Z) \tag{2.17}$$

The cumulative distribution function of the *DP* can be written as shown in Equation (2.18) where Φ is the cumulative distribution function of a standard normal random variable, μ_x is the median of the natural logarithm of the demand as a function of the *IM*, and σ_x is the logarithmic standard deviation of the demand conditioned on the *IM*. The median and approximation of the dispersion are shown in Equations (2.19) and (2.20), respectively.

$$F_D(d) = \Phi\left(\frac{\ln(d) - \mu_X}{\sigma_X}\right) \tag{2.18}$$

$$\mu_X = \rho IM^{\gamma} \tag{2.19}$$

$$\sigma_X = \sqrt{\frac{1}{n-1}\sum_{i=1}^{n}\left[\ln\left(\frac{d_i}{\rho IM_i^{\gamma}}\right)\right]^2} \tag{2.20}$$

Figure 2-17 compares the analytical cumulative distribution curve, $F_D(d)$, to the empirical one, $F_D^*(d) = i/n$. The agreement between the two curves confirms that the lognormal distribution assumption employed is applicable.

2.9.4 Probability of overturning

The probability of overturning cannot be determined using the previous linear regression method because it is a binary response (i.e. the block either tips or not) which is best described with a categorical response variable. A maximum likelihood estimation method is used to calculate the parameters $\hat{\mu}$ and $\hat{\beta}$ which describe the lognormal CDF of the categorical variable as given in Equation (2.21). The likelihood, as determined by Equation (2.22) for parameters μ and β is a measure of how well the analytical distribution matches the empirical one, where *d* is a vector of the intensity measures and *z* is a corresponding vector with values of 1 for overturning and 0 otherwise. The likelihood

function is maximized in Matlab to obtain the optimized parameters $\hat{\mu}$ and $\hat{\beta}$ that give the highest probability of producing the observed data [40].

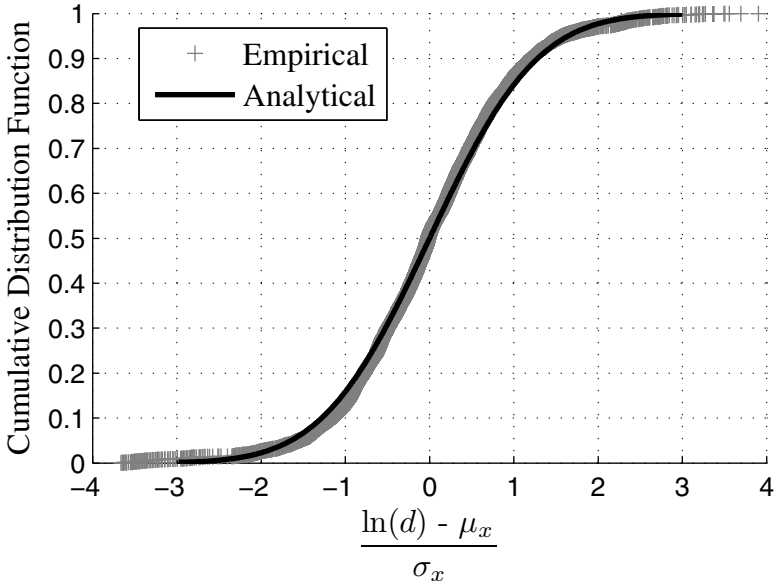

Figure 2-17. Empirical CDF versus analytical lognormal CDF.

$$F_D(d) = \Phi\left(\frac{\ln(d) - \hat{\mu}}{\hat{\beta}}\right) \tag{2.21}$$

$$L(\mu, \beta) = \prod_{j=1}^{n} \Phi\left(\frac{\ln(d_j) - \mu}{\beta}\right)^{z_j} \left(1 - \Phi\left(\frac{\ln(d_j) - \mu}{\beta}\right)^{1-z_j}\right) \tag{2.22}$$

2.9.5 Fragility curves

The fragility curves show the probability of exceeding a level of rocking throughout the building for any given *IM* and are defined using the lognormal CDFs derived earlier. Equations (2.23) and (2.24) show the probability of overturning, P_o, and the probability of a safe-rocking block exceeding a specific *LS*, P_{ex}, respectively.

$$P_o\left(D > C = overturn \mid IM\right) = \Phi\left(\frac{\ln(IM) - \hat{\mu}}{\hat{\beta}}\right) \tag{2.23}$$

$$P_{ex}\left(D > C = c \mid IM\right) = 1 - \Phi\left(\frac{1}{\sigma_X} \ln\left(\frac{c}{\rho IM^{\gamma}}\right)\right) \tag{2.24}$$

The probability of any rocking block exceeding a given *LS* is calculated as the union of the probability of overturning and the probability the block exceeds the *LS* given that it does not overturn. This is defined as P_f, which is expressed as

$$P_f = P_o + P_{ex} - P_o P_{ex} \tag{2.25}$$

The sequential fragility curves for *LS*s of c = 0.1, 0.3, 1 are shown in Figure 2-18. The data points on the figure show the probability of exceeding the *LS* for a specific interval strip of *IM* values as calculated by the number of simulations that exceed the limit divided by the total number of simulations in that *IM* interval. The close agreement of the empirical data points validates the fragility curves.

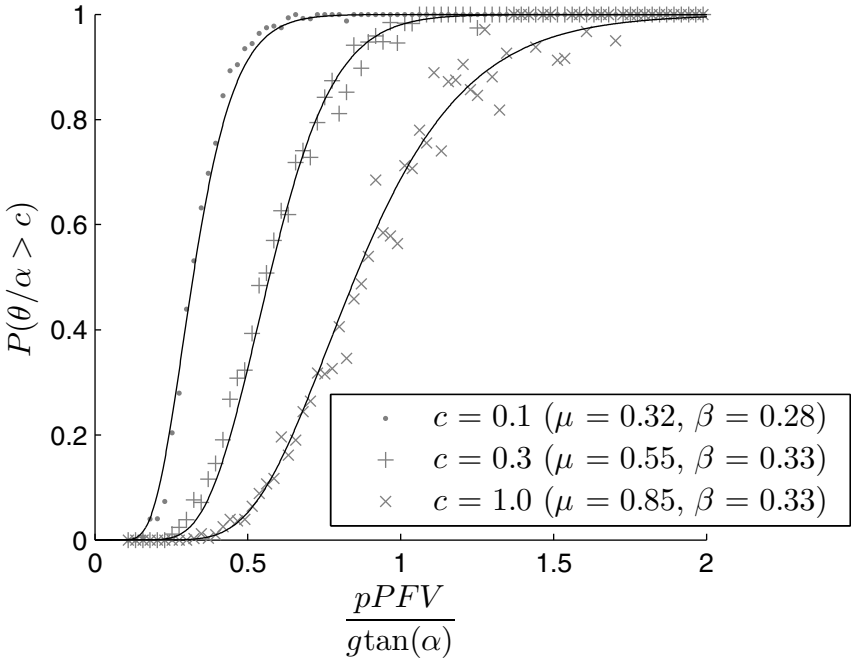

Figure 2-18. Fragility curves.

As an example, consider a hospital filing cabinet (R = 0.75 m, p = 3.13 rad/s, α = 15°) full of important patient data located on a floor where the *PFA* and *PFV* are estimated to be 3.0 m/s^2 and 0.4 m/s respectively. Considering only the horizontal excitation, the *PFA* exceeds the uplift threshold acceleration given by Equation (2.6), 2.6 m/s^2, meaning that rocking will initiate. The *IM* is calculated as 0.48 and the fragility curves can be used to

determine an 89% chance of minor uplift, 28% chance of exceeding the inflection point, and a 4% chance of overturning.

2.10 Conclusions

This paper examined the rocking response of slender building contents. This was done following a two stage cascading analysis approach. In the first stage a four story SCBF hospital was modeled in 3D in OpenSees and subjected to 20 broadband ground motions to obtain floor acceleration time histories at different locations on each story. These excitations were then used in the second stage to determine the rocking response of a wide variety of size and slenderness rigid blocks. The rocking results were subsequently analyzed and responses between the different locations were compared and contrasted. Fragility curves were created that show the probability of a block exceeding certain *LS*s for a given floor motion intensity level. These curves can be used to estimate the rocking response of a block given its dimensions and the *PFV*.

The applicability of the results is somewhat limited because of assumptions made during both stages of the analysis. First, only one specific building, a four story SCBF, was examined. This building can be viewed as an archetype whose response is representative of a typical braced frame. This model was then subjected to horizontal excitation in only one direction with the symmetric contents constrained to rocking in a plane. Only pure rocking motion was considered which assumes that there is sufficient friction to prevent sliding and that the transitions during impact are smooth. In reality, contents might move in all directions in any combination of response modes including rocking, sliding, twisting and bouncing. The theoretical maximum coefficient of restitution was also used whereas the actual coefficient of restitution is dependent on the material composition of the floor and the content itself. In this regards, the results presented can be taken as an upper bound estimate of the rocking response.

One of the main conclusions of this paper is that even at locations with high vertical accelerations, such as at the center of the bay on the roof, the effect of the vertical acceleration component on the rocking response is minimal. The consequence of this is that the rocking response does not depend on the location of an object within a given

story. The inclusion of the vertical ground acceleration component also introduced the ability of the rocking block to lift off the floor. The number of lift off or jumping occurrences was highest at the locations with the largest vertical accelerations as anticipated. Neither the content size nor slenderness had a significant effect on its tendency to jump.

As expected the rocking response does increase with the content's location, in terms of height within the building, for stocky (α = 20°) blocks. However, the difference in the rocking response between adjacent stories decreased towards the top of the building. Smaller stocky blocks experienced a larger increase in the rocking response as the content's height within the building increased. Interestingly, for slender blocks (α = 10°) the position of the content, in terms of story level, had little discernable effect on the rocking spectra. For blocks with an in-between slenderness (α = 15°) the content's height within the building mattered but the differences were smaller than for the stocky blocks. However, given the high nonlinearity in both the building model and the rocking response, further analysis should be done to verify this phenomenon for other buildings.

2.11 References

1. CSA. Seismic risk reduction of operational and functional components (OFCs) of buildings. *CSA S832-06 Canadian Standards Association*. Mississauga, ON, 2011.
2. Applied Technology Council (ATC). Reducing the risks of nonstructural earthquake damage*, ATC-69 Project Report*, Washington, DC. 2008.
3. Taghavi S, Miranda E, Response assessment of nonstructural building elements. *Report No. PEER 2003-05*, *Pacific Earthquake Engineering Research Center*, University of California, Berkeley, CA. 2003.
4. Foo S, Cheung M. Seismic risk reduction of operational and functional component of buildings: Standards Development. *13th World Conference of Earthquake Engineering*, Vancouver, B.C., 2004.
5. Comerio M.C, Stallmeyer J.C. Laboratory equipment: estimating losses and mitigation costs. *Earthquake Spectra* 2003; **19**(4):779–797.
6. Konstantinidis D, Makris N. Experimental and analytical studies on the seismic response of freestanding and anchored laboratory equipment. *Report No. PEER 2005-07*, *Pacific Earthquake Engineering Research Center*, University of California, Berkeley, CA. 2005.
7. Housner G.W. The behavior of inverted pendulum structures during earthquakes. *Bulletin of the Seismological Society of America* 1963; **53**:403–417.
8. Kamil A, Tung C. Energy balance equation for estimating overturning potential of an unanchored rocking body subjected to earthquake excitation. *Earthquake Spectra* 2001; **17**(2):209–220.
9. Makris M, Zhang J. Rocking response and overturning of anchored equipment under seismic excitation. *Report No. PEER* 1999-06, *Pacific Earthquake Engineering Research Center*, University of California, Berkeley, CA. 1999.
10. Yim C, Chopra A, Penzien J. Rocking response of rigid blocks to earthquakes. *Earthquake Engineering and Structural Dynamics* 1980; **8**:565–587.
11. Dimentberg M, Lin Y, Zhang R. Toppling of computer-type equipment under base excitation. *Journal of Engineering Mechanics, ASCE* 1993; **119**(1): 145–160.

12. Shi B, Anooshehpoor A, Zeng Y, Brune J. Rocking and overturning of precariously balanced rocks by earthquake. *Bulletin of the Seismological Soc. of America* 1996; **86**(5): 1364–71.
13. McKenna F, Fenves G.L, Scott M.H. Open system for earthquake engineering simulation (OpenSees). Accessed 2015.
14. USGS. U.S. Seismic Design Maps, *U.S. Geologic Survey*, Reston, VA, 2014.
15. American Society of Civil Engineers (ASCE). Minimum design loads for buildings and other structures*, ASCE 7-10*, Reston, VA, 2010.
16. ANSI/AISC 360-10. *Specification for structural steel buildings*. Chicago, IL: American Institute of Steel Construction; 2010.
17. Khatib I, Mahin S, Pister K. Seismic behavior of concentrically braced steel frames. *Report UCB/EERC 1988-01, Earthquake Engineering Research Center*, University of California, Berkeley, CA, 1988.
18. D'Aniello M, Costanzo S, Landolfo R. The influence of beam stiffness on seismic response of chevron concentric bracings. *Journal of Constructional Steel Research* 2015; **112**:305–324.
19. Kim J, Cho C, Lee K, Lee C. Design of zipper column in inverted V braced steel frames. *Proceedings of the 14th World Conference on Earthquake Engineering*, Beijing, China, October 2008.
20. Nikfar F, Konstantinidis D. Shake table investigation on the seismic performance of hospital equipment supported on wheels/casters. *Earthquake Engineering and Structural Dynamics* 2016 [in press].
21. Hsiao P-C, Lehman D, Roeder C. Improved analytical model for special concentrically braced frames. *Journal of Constructional Steel Research* 2012; **73**: 80–94.
22. Zhang W, Cai C, Pan F. Finite element modeling of bridges with equivalent orthotropic material method for multi-scale dynamic loads. *Engineering Structures* 2013; **54**(9): 82–93.

23. American National Standards Institute/Steel Deck Institute (ANSI/SDI). Composite steel floor deck-slabs. *SDI-C-2011*, 2011.
24. Huang Z, Burgess L, Plank R. Nonlinear analysis of reinforced concrete slabs subjected to fire, *ACI Structural Journal* 1999; **96** (1): 127–136.
25. Park R, Gamble W, *Reinforced Concrete Slabs, 2nd Ed*. John Wiley and Sons, 2000.
26. Vecchio F, Tata M. Approximate analyses of reinforced concrete slabs. *Structural Engineering and Mechanics* 1999; 8(1): 1–18.
27. Baker J, Lin T, Shahi S, Jayaram N. New ground motion selection procedures and selected motions for the PEER transportation research program. *Report No. PEER* 2011-03*, Pacific Earthquake Engineering Research Center*, University of California, Berkeley, CA. 2011.
28. Boore D, Atkinson G. Ground-motion prediction equations for the average horizontal component of PGA, PGV, and 5%-damped PSA at spectral periods between 0.01 s and 10.0 s. *Earthquake Spectra* 2008; **24**(1), 99–138.
29. USGS. Seismic hazard analysis tools – Interactive disaggregation. *U.S. Geologic Survey*, Reston, VA. 2008.
30. Furukawa S, Sato E, Shi Y, Becker T, Nakashima M. Full-scale shaking table test of a base-isolated medical facility subjected to vertical motions. *Earthquake Engineering and Structural Dynamics* 2013; **42**(13): 1931–1949.
31. Konstantinidis D, Makris N. Experimental and analytical studies on the seismic response of freestanding and anchored laboratory equipment. *Report No. PEER 2005/07*, Pacific Earthquake Engineering Research Center, University of California, Berkeley, CA. 2005.
32. Makris N, Konstantinidis D. The rocking spectrum and the limitations of practical design methodologies. *Earthquake Engineering and Structural Dynamics* 2003; **32**(2): 265–289.
33. MATLAB. Version R2009a. *The Language of Technical Computing*. The Mathworks, Inc.: Natick, MA, 2009.

34. Makris N, Konstantinidis D. The rocking spectrum and the shortcomings of design guidelines. *Report No. PEER 2001-07*, *Pacific Earthquake Engineering Research Center*, University of California, Berkeley, CA, 2001.
35. Dimitrakopoulos E, Paraskeva T. Dimensionless fragility curves for rocking response to near-fault excitations. *Earthquake Engineering and Structural Dynamics* 2015; **44**(12): 2015–2033.
36. Makris N, Black C. Uplifting and overturning of equipment anchored to a base foundation. *Earthquake Spectra* 2002; **18**(4): 631–661.
37. Sorrentino L, Msiani R, Decanini L. Overturning of rocking rigid bodies under transient ground motions. *Structural Engineering and Mechanics* 2006; **22**: 293–310.
38. Dimitrakopoulos E, DeJong M. Overturning of retrofitted rocking structures under pulse-type excitations. *Journal of Engineering Mechanics, ASCE* 2012; **138**: 963–972.
39. Zhang J, Makris N. Rocking response of free-standing blocks under cycloidal pulses. *Journal of Engineering Mechanics, ASCE* 2001; **127**(5):473–483.
40. Baker J. Efficient analytical fragility function fitting using dynamic structural analysis. *Earthquake Spectra* 2015; **31**(1): 579–599.

Chapter 3: The Effectiveness of Base Isolation as a Strategy to Protect Freestanding Slender Building Contents against Rocking and Overturning

Summary

During an earthquake event, freestanding slender building contents can uplift and overturn resulting in injury and economic loss. However, little research has focused on this topic to date. This paper examines the rocking response of rigid slender contents in fixed-base (FB) and base-isolated (BI) buildings. Models of hospitals in Los Angeles were created for both types of buildings in OpenSees. Lead-plug (LP) and triple-friction-pendulum (TFP) isolation systems were designed with a range of effective period and damping values. The rocking response was calculated for contents with different size and slenderness for each floor acceleration time history. Overall, base isolation was very effective both at limiting the number of contents that experienced uplift and, for those contents that uplifted, at reducing the rocking response. This was due to the lower floor accelerations in spite of the long period BI floor motions, which were postulated to produce overturning at lower intensities. In general, contents in the LP systems had higher rocking response than contents in the corresponding TFP systems. Also, the content rocking response in buildings with isolation systems with longer effective periods was lower than for systems with shorter periods due to lower floor accelerations and velocities. The effective damping had less of an impact on the rocking response than the period, although higher damped systems tended to have slightly lower floor accelerations and therefore rocking responses. The variance in the rocking response up the height of the structure was less defined in the BI building than the FB building, but the highest responses were located at the roof and base due to second mode effects. Finally, the paper presents fragility curves for the BI buildings with 2.5 s effective periods for use in design.

3.1 Introduction

It is a well-known fact that the damage and failure attributed to nonstructural components during an earthquake can cause widespread destruction resulting in large economic losses,

extended downtimes for critical facilities, and even loss of life [1, 2]. Nonstructural components and contents make up 80 - 90% of the value of a commercial building, and more in buildings such as hospitals and museums [3]. In a previous publication the authors examined the rocking response of contents in a FB building [4]. Slender contents throughout this building were found to be highly susceptible to rocking and overturning. One way to protect these contents is through base isolation of the building, although floor isolation and component isolation are also potential protection strategies. Base isolation decouples the building from the horizontal ground motion during an earthquake through the introduction of horizontally flexible isolators between the foundation and the building. Structural engineers have accepted that base isolation significantly reduces structural demands, such as story drifts and accelerations, making it an effective way to protect nonstructural components whose response is affected by these parameters [5, 6]. The demand quantification on nonstructural components, however, has not received as much attention as that on the isolation system or structure. The effect of different seismic isolation systems on the performance of attached equipment that behave like viscously damped linear oscillators has been studied at various levels in [7-9]. Recently, shake-table testing has been conducted on full-scale BI building models to investigate the behavior of a wide variety of nonstructural components [10-12]. The seismic response of unattached stocky contents, which are prone to sliding, has been studied in [13].

The primary mode of response of slender freestanding contents, such as hospital equipment, statues, filing cabinets, and bookshelves, during an earthquake is rocking. Rocking is one of the most destructive response modes that contents can experience during an earthquake because it causes extremely high accelerations during contact and can lead to overturning. Base isolation is very effective at reducing the amplitude of the floor accelerations, and therefore decreasing the chance of uplift, i.e., the initiation of rocking. However, the floor acceleration time histories in BI buildings have much longer periods, which can have the effect of acting as a ‘static’ force should the block start to rock. Several studies have pointed out that rigid blocks can be toppled from an input pulse with a lower amplitude and longer period than a shorter period pulse of higher amplitude

[14, 15]. This suggests that freestanding slender blocks in an isolated building (where floor accelerations are decreased, compared to a FB building, but vibration period is increased) may result in overturning of rigid blocks under motions which would not have overturned the same object in a FB building. A limited number of studies have also been done using isolated bases as a way of protecting individual objects, mainly for invaluable art pieces [16-18]. Roussis and Odysseos examined rigid blocks on an isolated base under pulse-type motions and concluded that isolation is able to increase the slenderness ratio needed for uplift and generally reduce overturning [19]. Vassiliou and Makris [15] studied freestanding rigid blocks on an isolated base and concluded that isolation only improves the stability of small blocks. They found that isolation also removes inherent rocking properties of a rigid block including the scale effect and stability under high frequency content so that large blocks are less stable when isolated. They also confirmed that isolation does increase the peak ground acceleration necessary to uplift an artifact.

The main objective of this study is to determine the effectiveness of base isolation in reducing the rocking response of slender rigid contents and under what conditions isolation may actually amplify the response. To do this, OpenSees models of FB and BI hospitals were created and subjected to 20 ground motions. The same superstructure was used along with both lead plug (LP) rubber bearings and triple friction pendulum (TFP) bearings for a variety of different effective periods and damping. The floor accelerations recorded in these buildings were used to determine the rocking response of contents with different sizes and slendernesses. The rocking results from the conventional and BI buildings were compared and base isolation was found to be effective at reducing the rocking response. The rocking results for the different isolation systems and designs are also compared. Finally, fragility curves are created for use by designers to estimate the rocking response of contents within a building.

3.2 Overview of the building designs

The FB and BI hospitals were designed as essential facilities in Los Angeles (34.02197˚N, 118.28587˚W) on site class C soil with an S_{DS} and S_{D1} of 1.23 and 0.56, respectively [20]. The gravity loading for both buildings was consistent with a dead load

of 4.0 kPa, live load of 2.5 kPa, and a 0.96 kPa cladding load. Both buildings had 4.5 m story heights and a footprint of four 8 m bays by six 7 m bays with bracing located in the center two bays of the exterior frames. The FB building was designed as a special concentrically braced frame (SCBF) in compliance with ASCE 7-10 using chevron bracing and zipper columns with a force reduction factor of 6 and drift limit of 2.5% [21]. Additional detail on the design and modeling of this building can be found in [4]. The isolated superstructure was designed as an ordinary concentrically braced frame (OCBF) with a force reduction factor of 1 and a 1.5% drift limit. The designs of both the FB and BI buildings were force controlled. Elevation views of the structures are shown in Figure 3-1. The steel members were designed in accordance with AISC 360-10 and the selected members are shown in Table 3-1[22].

Table 3-1. Structural steel member schedule

	Both		Fixed-Base			Base-Isolated	
Story	Column	Girder	Braced Column	Brace	Zipper Column	Braced Column	Brace
1	W14X68	W14X68	W14X233	HSS12X12X5/8	W14X48	W14X145	HSS12X12X5/8
2	W14X68	W14X68	W14X233	HSS10X10X5/8	W14X48	W14X145	HSS10X10X5/8
3	W14X48	W14X68	W14X68	HSS9X9X5/8	W14X48	W14X68	HSS10X10X5/8
4	W14X48	W14X68	W14X68	HSS7X7X5/8	W14X48	W14X68	HSS10X10X5/8

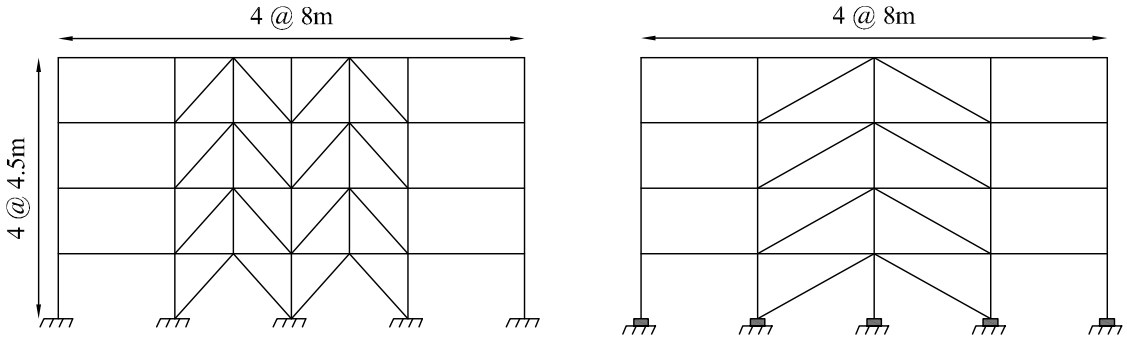

Figure 3-1. Left: Elevation view of FB SCBF. Right: BI OCBF.

3.3 Isolation system design

The BI buildings were isolated using LP or TFP bearings. For each type of isolation system, the effective period and damping at the DBE level varied as shown in Table 3-2, for a total of 8 isolated buildings. The design of the LP and TFP bearings to meet these

criteria is detailed in the following sections. All the isolation systems were investigated using the same superstructure.

Table 3-2. Effective period and damping used for both the LP and TFP isolators

System	Name	Effective Period at DBE, T_D (s)	Effective Damping at DBE, $\zeta_{eff,D}$ (%)
1	T25D15	2.5	15
2	T25D25	2.5	25
3	T35D15	3.5	15
4	T35D25	3.5	25

3.3.1 Lead plug rubber bearings

LP systems can be accurately modeled using a bilinear hysteresis [23, 24]. Three parameters are needed to define the bilinear force-displacement backbone curve. The parameters set in this study are the effective stiffness and damping at the design displacement, and η, the ratio of the post-yield stiffness, k_2, to initial stiffness, k_1. This ratio was taken as $\eta = 0.1$, which is typical for LP bearings [25, 26]. Equations (3.1) and (3.2) from ASCE 7-10 are used to determine the isolation system design displacement, D_D, and period, T_D [13].

$$D_D = \frac{gS_{D1}T_D}{4\pi^2 B_D} \tag{3.1}$$

$$T_D = 2\pi\sqrt{\frac{W}{k_{eff}g}} \tag{3.2}$$

Here B_D is a damping coefficient based on the effective damping at the DBE level displacement, W is the weight of the superstructure and basemat, and k_{eff} is the effective stiffness at the DBE level. The unique parameters of the hysteresis can be fully determined using the effective stiffness at the design displacement, determined from Equations (3.1) and (3.2), along with the previous assumptions of η and ζ_{eff}. The equivalent damping for a bilinear isolation system is based on the area contained by a hysteresis loop and is given by [27],

$$\zeta_{eff} = \frac{4Q\left(D_D - D_y\right)}{2\pi k_{eff} D_D^2} \tag{3.3}$$

where Q is the characteristic strength, D_y is the yield displacement, and

$$k_{eff} = k_2 + \frac{Q}{D_D} \tag{3.4}$$

$$k_2 = \eta k_1 \tag{3.5}$$

$$D_y = \frac{Q}{k_1 - k_2} \tag{3.6}$$

By substituting these equations into Equation (3.3) and rearranging, the yield displacement can be expressed as

$$D_y = \frac{1}{2} D_D \left(1 - \frac{1}{2}\zeta_{eff}\pi - \sqrt{\left(1 - \frac{1}{2}\zeta_{eff}\pi\right)^2 - 2\pi\zeta_{eff}\frac{\eta}{1-\eta}} \right) \tag{3.7}$$

3.3.2 Triple friction pendulum bearings

The behaviour of TFP bearings is governed through sliding on the four surfaces shown in Figure 3-2 (left). The seismic performance of the bearings can be optimized by designing the effective radius and size of the surfaces along with their coefficients of friction [28]. The TFP systems were designed to match the LP systems' design displacement, effective damping, and effective period at the DBE level. The bearings considered in this paper are vertically symmetric so that the dimensions and properties of the surfaces on the inner puck are the same as well as the outer surfaces of the articulated slider. The backbone curve of such a bearing is shown in Figure 3-2 (right) [29]. It is stiff under small displacements to keep the building near motionless under a small earthquake or wind loading but relatively flexible under design level displacements to reduce forces transferred to the superstructure. Under large displacements the system stiffens again to prevent very large displacements under MCE level excitation and limit the size of the seismic gap. The yield displacement and the coefficient of friction of the inner puck were held constant for all the systems at D_y = 0.5 mm and μ_1 = 0.02.

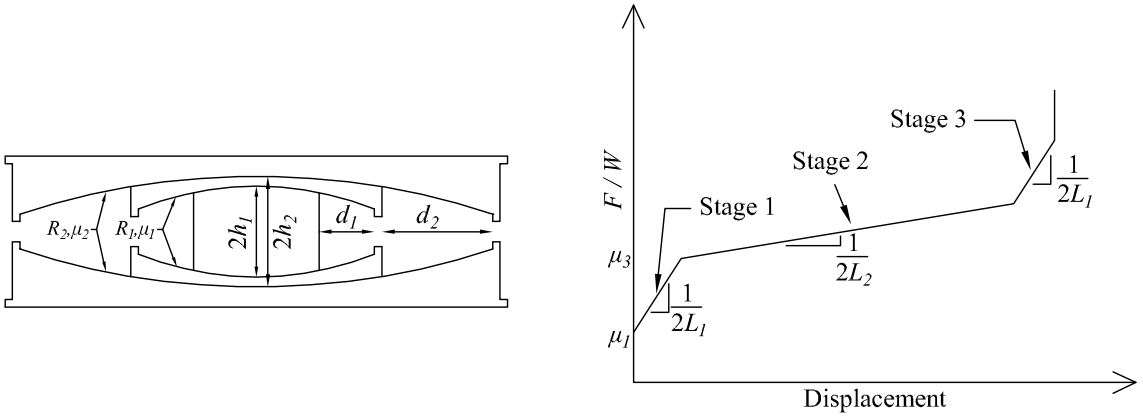

Figure 3-2. Left: Schematic of TFP bearing. Right: TFP backbone curve

The effective radius, L_2, was determined by setting the post-yield stiffness, k_2, of the equivalent bilinear elastomeric system equal to the stiffness of the TFP at stage 2. The remaining two parameters that define the first two stages of the TFP, L_1 and μ_2, were determined by setting the effective period and damping to the objective design values for each system at the design displacement as shown in Equations (3.8) – (3.10) [28].

$$T_{eff,D} = 2\pi\sqrt{\frac{W}{gk_{eff,D}}} \tag{3.8}$$

$$k_{eff,D} = \left(\mu_2 + \frac{1}{2L_2}\left(D_D - \left(\mu_2 - \mu_1\right)\left(L_1 + L_2\right)\right)\right)\frac{W}{D_D} \tag{3.9}$$

$$\zeta_{eff,D} = \frac{2W\left\{\left(\mu_2 - \frac{1}{2L_2}\left(\mu_2 - \mu_1\right)\left(L_1 + L_2\right)\right)D_D - \left(\frac{L_2 - L_1}{2L_1L_2}\right)\left(\mu_2 - \mu_1\right)^2\left(L_1 + L_2\right)^2 - \left(\frac{\mu_1}{D_y} - \frac{1}{2L_1}\right)D_y^2\right\}}{\pi k_{eff,D} D_D} \tag{3.10}$$

The displacement capacity of the inner pendulum, d_1, was held constant at 4 cm for each system while the outer displacement capacity, d_2, was set to so that the MCE level design displacement was located at the transition from stage 2 to 3 as determined by Equation (3.11). When designed this way, the effective period and damping of the LP and TFP systems are also equal at the MCE level. Table 3-3 shows the design parameters for both the LP and TFP bearings for each system.

$$d_2 = \frac{1}{2}\left\{D_M - 2L_1\left(\mu_2 - \mu_1\right)\right\} \tag{3.11}$$

The design base shear coefficient, C_S, is defined as the ratio of the design base shear, V_S, to the weight of the building as given in Equation (3.12) [21]. The design base shear is taken as the maximum shear force of the isolators at the design level displacement divided by the force reduction factor, R_I, as shown in Equation (3.13). The force reduction factor for the superstructure of the isolated building was taken as unity, which is typical for BI structures to avoid large story drifts.

$$C_S = \frac{V_S}{W} \tag{3.12}$$

$$V_S = \frac{k_{eff} D_D}{R_I} \tag{3.13}$$

Table 3-3. Properties of the LP and TFP isolators

			T25D15	**T25D25**	**T35D15**	**T35D25**
Effective Period at DBE	T_D	(s)	2.5	2.5	3.5	3.5
Effective Damping	$\zeta_{eff,D}$	(%)	15	25	15	25
Design Disp. at DBE	D_D	(cm)	25.5	21.5	35.7	30.2
Yield Displacement	$D_{y,LP}$	(cm)	0.9	1.8	1.3	2.5
Inner Effective Radius	L_1	(cm)	30.9	27.3	109.6	73.0
Outer Effective Radius	L_2	(cm)	120.8	135.8	201.4	266.3
Inner Friction Coef.	μ_1	-	0.02	0.02	0.02	0.02
Outer Friction Coef.	μ_2	-	0.049	0.069	0.039	0.051
Inner Disp. Capacity	d_1	(cm)	4.0	4.0	4.0	4.0
Outer Disp. Capacity	d_2	(cm)	22.1	18.3	30.0	25.3
Base Shear Coefficient	C_S	-	0.16	0.14	0.12	0.10

The superstructure used for all isolation systems was designed for a base shear coefficient of C_s = 0.16. The hysteresis for all the LP and TFP isolation systems at the DBE level design displacements are shown in Figure 3-3.

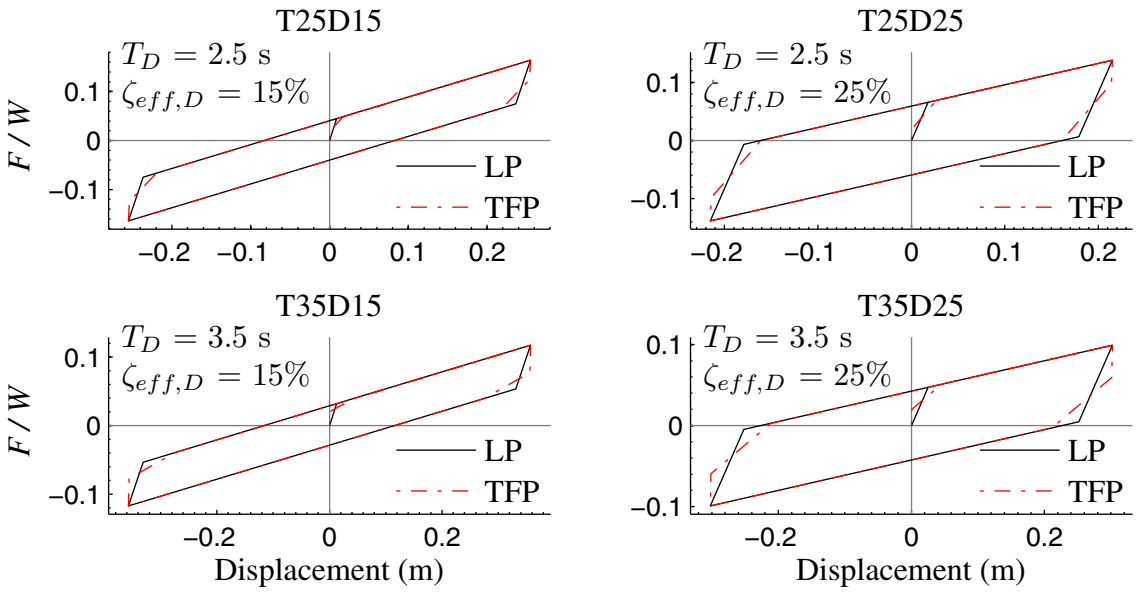

Figure 3-3. Isolation system hysteresis

3.4 Modeling overview

2D models of the braced frames as shown in Figure 3-1 were created in OpenSees for both the FB and BI buildings [30]. The vertical accelerations, which may vary throughout the floor plan, have an insignificant effect on the rocking response which makes a 2D model sufficient in this regards [4]. The effective seismic weight of 9430 kN per story was based on the full dead and live load as in [29]. Half the mass of the building was applied to the modeled braced frames and assigned in the horizontal direction at the story nodes. The vertical mass tributary to half a baywidth was also applied at each story node. The models were then subjected to the twenty ground motions to obtain horizontal and vertical floor acceleration time histories at each story level.

3.4.1 Fixed base building

Structural W-sections were used for both the columns and girders. These members were modeled using an expected steel yield strength of $f_{y,e}$ = 379 MPa with 3% strain-hardening. The columns were fully fixed at the base, while the girders were allowed to rotate at the columns. Different HSS sections were used for the braces at each story. The braces were made of 6 elements aligned along a sinusoidal curve with an initial camber of

L_b/500 at the center to enable buckling. The braces were translationally fixed to the column nodes while zero-length gusset plate members controlled the in-plane rotation and were designed according to the method proposed in Hsiao et al. [31]. The gravity loads were applied as point loads to each column node according to its tributary vertical mass. A leaning column with high axial stiffness and very low flexural stiffness was also modeled and rigidly attached to the center of the frame. The gravity load for the rest of the building tributary to the modeled frame was applied at each story of the leaning column to account for P-delta effects. A 2% stiffness-proportional damping was applied at the first mode frequency as in [32].

3.4.2 Base isolated superstructure

The superstructure was modeled with the same general assumptions as the FB building. The braces, however, were modeled with an initial center offset of L_b/500 = 18 mm using only two elements to reduce computation time because minimal buckling was expected in the superstructure. A leaning column was also modeled for the superstructure to account for P-delta effects of the gravity loads for half the building not directly tributary to the braced frame. The leaning column was fixed in the vertical direction at its base at the height of the top of the isolation level but allowed to laterally displace freely with the base mat. The nodes at each story were rigidly attached to the center of the braced frame. Stiffness-proportional damping of 2% was applied in the superstructure at the post-yield isolator frequency, as Rayleigh damping can cause unrealistic damping forces [33].

3.4.3 Lead plug rubber bearings

The isolation system was designed for an isolator under each of the 35 columns. Therefore, because only the exterior braced frame was modeled, the isolators modeled under these columns represent the isolators for half the building. Accordingly, they were modeled with 3.5 times the lateral stiffness of a single isolator. The isolators were modeled using three elements: a column element, a horizontal spring, and a vertical spring, as shown in Figure 3-4 (left) [29, 32]. The column provided the post yield stiffness of the isolators in shear but negligible vertical stiffness. The horizontal spring provided the initial stiffness of the isolators as well as the hysteretic damping. This was

done using a zero-length element with an elastic perfectly plastic uniaxial material. The vertical spring was modeled using a truss element with a multilinear elastic uniaxial material. The ratio of the compression stiffness over the post yield lateral stiffness was $k_c/k_2 = 1000$. The yield strain of the bearings in tension was taken as $\varepsilon_y = 0.03$ and the tensile-to-compressive stiffness ratio was taken as $k_t/k_c = 0.06$, as recommended in Yang et al. [34]. The rotation at the top of the isolator was fixed. The full weight of the superstructure and basemat minus the loads already applied on the superstructure tributary to each isolator were applied at the top of the individual isolators to ensure correct vertical load and P-delta effects in the isolators.

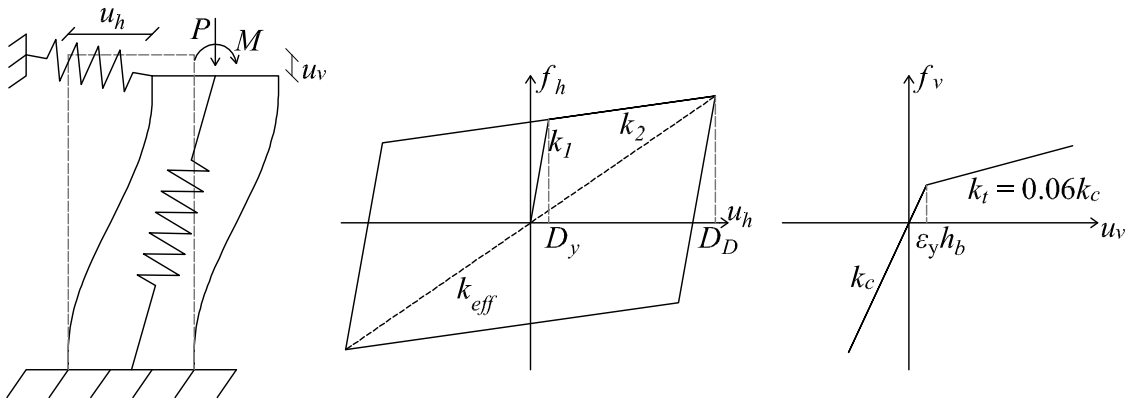

Figure 3-4. Left: Modeled isolator with one column element and two spring elements. Center: Lateral force-deformation. Right: Vertical force-deformation

3.4.4 Triple friction pendulum bearings

The triple friction pendulum OpenSees element developed by Dao [35] was used to model the TFP isolators. Since this is only a 3D element the entire 2D frame was modeled in 3D and constrained to the plane of the frame. The compressive vertical stiffness was taken as 10,000 times the initial stiffness of the equivalent bilinear system, or 10 times the vertical stiffness of the elastomeric bearings [36]. In actuality there is no tensile stiffness but it was taken as 100 N/m for the sake of numerical continuity and to ensure convergence during the time history analysis as suggested by OpenSees [37]. Coulomb friction was used for the friction model, which assumes that the coefficient of friction is constant and is independent of velocity and pressure. The analysis was run using a timestep of 0.0005 s to accurately capture the high frequency components of the

horizontal and vertical coupling of the TFPs as recommended by OpenSees and to obtain convergence [37].

3.5 Building periods

The first three periods of the buildings as determined via elastic eigenvalue analysis are shown in Table 3-4. The periods of the BI buildings were found using a linear elastic spring at the isolation level with the effective stiffness of the isolators at the DBE level design displacement. The equivalent LP and TFP isolation systems have the same effective stiffness at the design displacement and thus the same periods. The period of the superstructure used in the BI buildings was 0.76 s. The fact that the fundamental mode of the BI structures is only moderately larger than the period of the isolation systems suggests that most of the displacement occurs in the isolators even though the superstructure is relatively flexible. The second mode of the BI buildings is very similar for all the isolation systems and consists of the isolation system displacing in one direction and the superstructure in the other, creating a center of rotation at around the second story.

Table 3-4. Periods of the frames

Mode	**FB**	**BI**			
		T25D15	T25D25	T35D15	T35D25
1	0.47 s	2.59 s	2.59 s	3.57 s	3.57 s
2	0.18 s	0.46 s	0.45 s	0.46 s	0.46 s
3	0.12 s	0.22 s	0.22 s	0.22 s	0.22 s

3.6 Ground motion selection and scaling

Twenty ground motions were selected from Baker's suite set 1a for the time history analysis [38]. The 40 earthquakes in this suite have shear wave velocities of 200 – 400 m/s and were selected to match the Boore Atkinson ground motion prediction spectrum of magnitude 7 and at a distance of 10 km [39]. A disaggregation of the site hazard shows this to be an appropriate suite to select motions from [40]. All the individual motions' spectra were then scaled to match the DBE level design spectrum at both the FB period as well as the BI building periods. This was done by scaling each of the 80 horizontal

ground acceleration records to the design spectrum between the periods of 0 and 4 s and minimizing the sum of the square of the differences between them [13]. The twenty motions with the least error were selected although no two components from the same record were selected. The vertical components of the records were then scaled using the same factor as applied to the corresponding horizontal record. The horizontal ground response spectra and their mean are shown in Figure 3-5 along with the design spectrum.

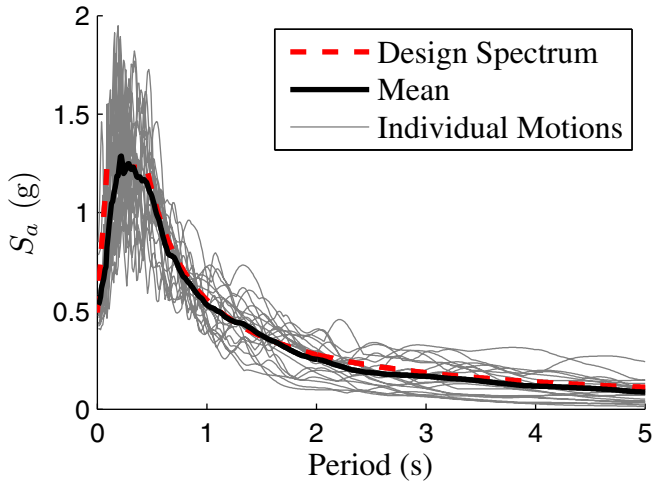

Figure 3-5. Selected ground motion response spectra

3.7 Structural response

The ground motion suite was used as input for the nonlinear time history analysis of the FB and BI buildings. The resulting median isolation system displacement is shown in Table 3-5 for the different systems.

Table 3-5. Design and actual isolator displacements

Displacement		T25D15	T25D25	T35D15	T35D25
Design (D_D)	(cm)	25.5	21.5	35.7	30.2
Median LP	(cm)	21.1	19.1	26.5	22.8
Median TFP	(cm)	20.4	19.1	24.6	21.5

For all systems, the median isolation displacement is smaller than the design displacement. This is due to the fact that the equivalent linear isolator model assumed by ASCE 7-10 overestimates the isolator displacements when compared to bilinear isolation models [41-43]. The corresponding LP and TFP systems had similar displacements,

although the TFP displacements were slightly smaller for each system. None of the TFP isolators reached the fourth (stiffening) stage.

The isolation systems performed well in reducing the story drifts, *PFV*s, and *PFA*s at each story, compared to the FB case. The mean values of the various peak structural responses across the height of the building are shown in Figure 3-6. The *PFV*s and *PFA*s in the BI buildings remained fairly constant over the height of the superstructure suggesting that the buildings reacted mostly in the first mode with the lateral displacement concentrated in the isolators. The *PFV* increased subtly up the building, while the *PFA*s were the highest at the base and roof and lowest at mid height of the building. This is due to the second mode response of the building with the center of rotation near the second story as previously explained.

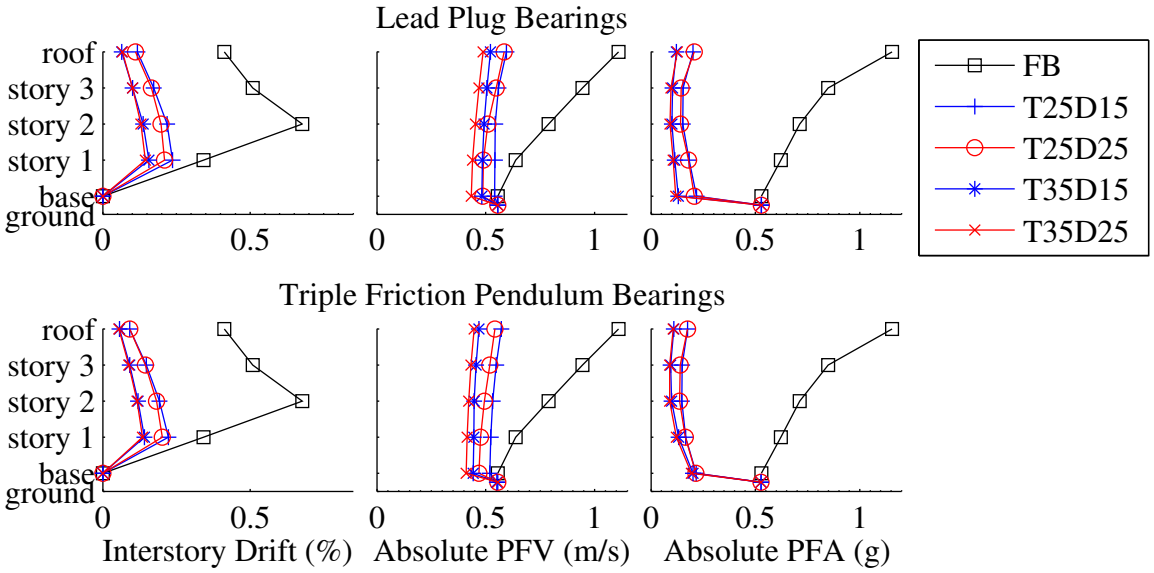

Figure 3-6. Mean peak building responses for the FB and BI buildings. Left: Peak story drift. Center: Absolute peak floor velocities. Right: Absolute peak floor accelerations

The *PFA*s at the roof were reduced by between 87 and 93%, and the absolute *PFV*s by between 46 and 60% depending on the system. The superstructures in the BI buildings remained essentially elastic in accordance with the design objective of using a force reduction factor of 1. The second story braces buckled first in the FB building for the

majority of the earthquakes and had the highest mean peak story drift. The second story drift was reduced by between 70 and 84% for the isolated buildings.

For each of the peak responses shown in Figure 3-6, the buildings with isolation systems with an effective period of 3.5 s had lower responses than the buildings with 2.5 s effective period. The same was true for isolation systems with higher effective damping, i.e. 25% v. 15%. These results were expected as per previous literature [41, 44]. The base shear coefficients shown in Table 3-3 also increase in this order. A higher base shear coefficient transfers greater forces to the superstructure and thus larger story drifts, relative floor velocities, and accelerations are expected.

The response spectra at the base of the superstructure are shown in Figure 3-7 for all four systems. The LP isolated building's spectra had two distiguishable peaks. The first peak is at the second mode of the isolated superstructure which is 0.46 s for all the systems. The spectral accelerations at this mode are highest for the base and roof and lowest for the second story, near the center of rotation.

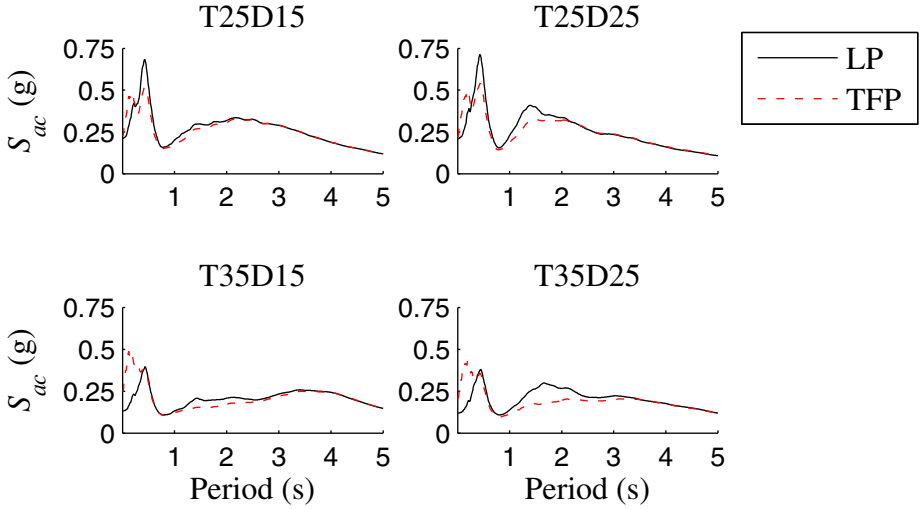

Figure 3-7. Floor response spectra at the base for the BI and FB buildings

The longer period peak was at the effective period of the isolation system and was wider and less defined. This is because the effective period is dependant on the displacement. The long period peaks of the 15% effective damping systems were closer to the design period than the 25% damped peaks both because the mean displacement of the lower

damped systems was closer to the design displacements and the isolator spent more time at the post yield stiffness due to the smaller yield displacement. The TFP spectra had similar peaks at the effective first and second modes of the isolated building. However, the longer period peak was closer to the effective period due to the small yield displacement. The TFP spectra also had another peak at the third mode of the building. This was only evident in the TFP isolated structure because the very high initial stiffness allows the transmission of high frequency content into the superstructure [41].

3.8 Review of the dynamics of a rocking object

Slender unanchored building contents respond primarily through rocking about their edges during an earthquake as shown in Figure 3-8.

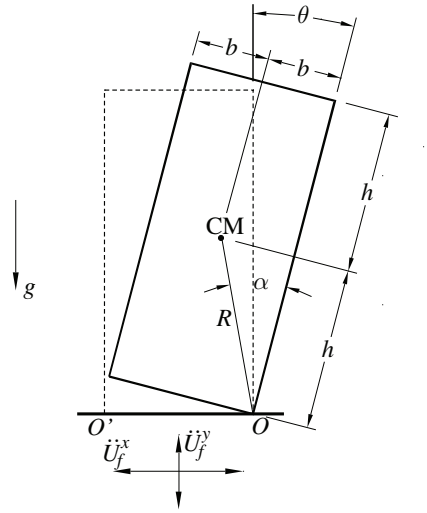

Figure 3-8. Rocking block

Although this motion may be combined with sliding or other responses, only pure planar rocking is considered in this study. Rocking is initiated when the floor acceleration exceeds the threshold, Equation (3.14), based solely on the slenderness of the block, α, [45].

$$\left|\ddot{U}_f^x\right| \geq \left(g + \ddot{U}_f^y\right)\tan(\alpha) \tag{3.14}$$

A sufficient coefficient of friction between the edge of the rocking object and the floor is necessary for sustained rocking and is assumed present for the analysis in this paper. The

equation of motion for a rocking rigid block under both horizontal and vertical excitation at its base is [46, 47]

$$\ddot{\theta} = -p^2 \left\{ \left(\frac{\ddot{U}_f^y}{g} + 1 \right) \sin\left(\mathrm{sgn}(\theta)\alpha - \theta \right) + \frac{\ddot{U}_f^x}{g} \cos\left(\mathrm{sgn}(\theta)\alpha - \theta \right) \right\} \tag{3.15}$$

In order to rotate smoothly from one edge to the other, the angular momentum of the block must be conserved during an impact. For this to be observed, the block must lose energy every time it makes contact with the floor. The energy is removed from the system using a coefficient of restitution, *e*, which is the ratio of the angular velocities immediately before and after impact, $e = \dot{\theta}_2 / \dot{\theta}_1$ .The maximum coefficient of restitution for which a block of slenderness α will undergo smooth rocking is

$$e = 1 - \frac{3}{2}\sin^2\alpha \tag{3.16}$$

Notably, stockier blocks require a smaller coefficient of restitution in order to observe rocking motion and thus experience higher damping. In fact, blocks with α = 55° are perfectly plastic and will hypothetically not undergo sustained rocking even if the coefficient of friction and base acceleration are great enough [48].

3.9 Effectiveness of seismic isolation in reducing uplift occurrences

The main objective of base isolation is to reduce the story drifts and accelerations experienced by the superstructure in order to protect it and its contents. In the case of slender contents it is most effective by reducing the floor accelerations below the threshold necessary to induce uplift and initiate rocking. Figure 3-9 shows the ratio of the 20 ground motions that cause uplift at the base (left) and roof (right) for a range of slender objects. All the records produced uplift in the FB building up to the highest slenderness considered, α = 20°. All the isolation systems considered were effective in reducing the *PFA*s significantly and therefore protected higher slenderness blocks against rocking. While the FB building is able to induce rocking in stockier blocks up the height of the building, the BI buildings have fairly uniform *PFA*s and therefore the maximum slenderness of blocks that will rock is similar for all stories.

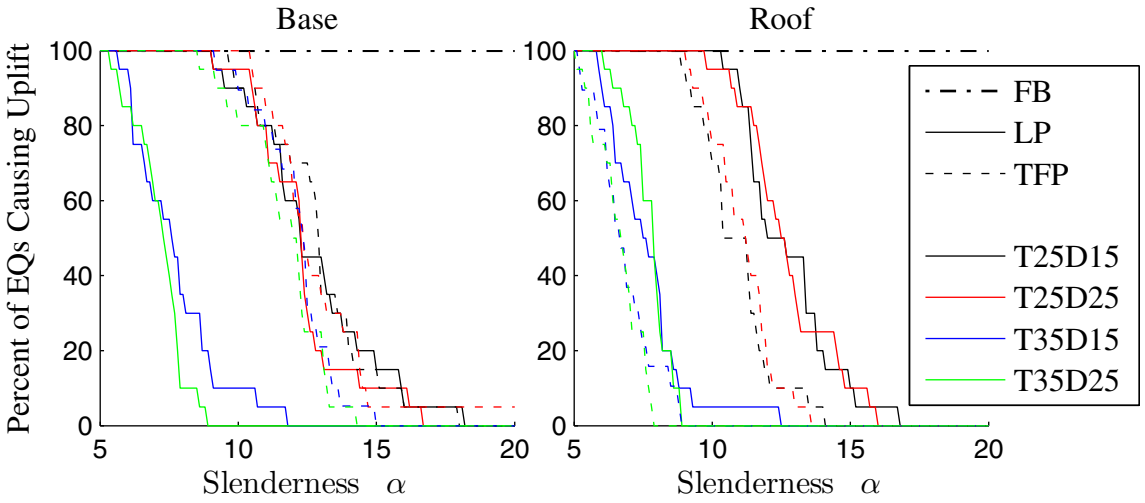

Figure 3-9. Percent of earthquakes that initiate uplift at different slenderness

The 2.5 s LP systems were effective at eliminating the rocking of any block with greater than 17° slenderness while the 3.5 s systems further reduced this to nearly 12°. For the LP isolation systems, the systems with a 2.5 s effective period had about a 5° higher maximum slenderness that experienced rocking than the 3.5 s systems. Systems that had 25% effective damping compared to 15% damping typically had fewer of the records produce rocking at the base for a given slenderness, but the difference was marginal. At the base, all the TFP systems were similar with the higher effective period and damping systems showing marginally more protection. At the roof, the TFP systems had a lower uplifting slendernesses than the equivalent LP systems by about 1 - 2°. At the base, the 2.5 s effective period systems are similar for LP and TFP, but for the 3.5 s systems the TFP isolated buildings had higher slenderness blocks uplifting.

3.10 Effectiveness of base isolation for reducing rocking responses

The previous section showed that isolation is effective at preventing uplift in stockier objects, which would normally respond in rocking. One of the concerns with isolation is that, although it decreases floor accelerations, it elongates the vibration period; the long period floor motion could act as a static force and possibly overturn objects that might not experience overturning in a FB building. To examine this, the peak rocking responses of contents with α = 7.5, 10, 12.5 and 15° and various sizes (expressed through the ratio

$2\pi / p = 4\pi\sqrt{R/3g}$, where R is shown in Figure 3-8), placed on different levels within the FB and BI buildings were computed. These slenderness values were chosen for contents that are expected to uplift in the BI buildings. The peak responses are presented herein through *rocking spectra* [49], which are analogous to response spectra but for rocking blocks, showing the peak rotation, normalized by α, vs $2\pi/p$ for a fixed value of α.

Figure 3-10 shows the average rocking spectra of the 20 motions at these slenderness values for the FB building and the LP isolated building with a 2.5 s effective period and 15% damping. It is evident that the base isolation reduces the rocking response significantly.

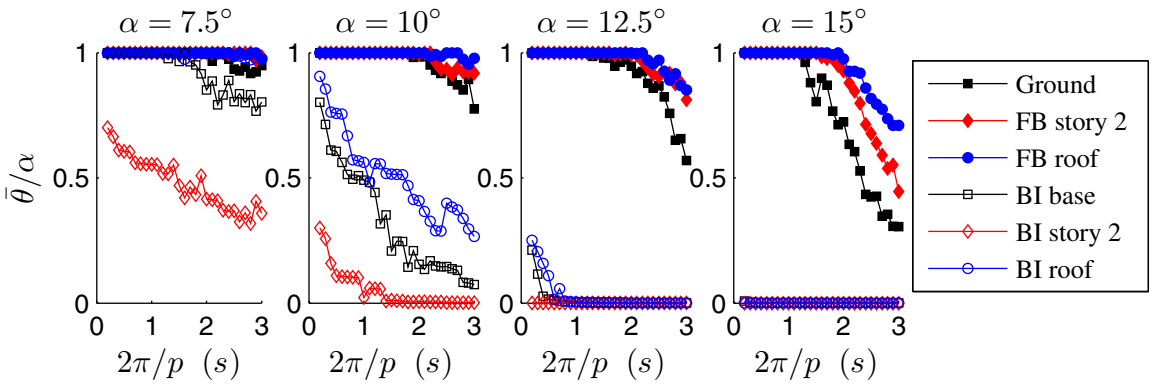

Figure 3-10. Rocking Spectra for LP isolated building with 2.5 s period, 15% damping and the FB building.

The BI building nearly eliminates rocking altogether for all but very slender contents. For the 15° contents, isolation is able to completely eliminate rocking at every floor. In the FB building, contents of this slenderness all overturned up to a size of about $2\pi/p$ = 1.7 s (R < 54 cm) at the roof and even the larger contents experienced significant rocking.

The BI building's contents with 10° slenderness began to experience rocking as well. Contents of all sizes safely rocked at the base and the roof, but on the middle floors only the smaller contents uplifted. The responses were still significantly lower than the results in the FB building where all block sizes examined underwent severe rocking or overturning. Almost all of the very slender contents (7.5° slenderness) in the FB building overturned. The contents in the BI building also had significant rocking with contents at

the roof experiencing the same level of rocking as in the FB building. Contents at the other levels still experienced lower levels of rocking than the corresponding contents in the FB building. These very slender blocks (7.5°) were the only situation where base isolation did not significantly reduce the rocking response. The only time that the average rocking response in the isolated building was larger than in the FB building was for the rare case of large ($2\pi/p$ > 2.5 s, R > 1.2 m) objects of this slenderness at the roof.

The fact that base isolation was able to effectively reduce the rocking response corroborates the work of Vassiliou and Makris [15]. They concluded that isolating individual contents is only effective for smaller objects up to a limit of $\omega_{pulse}/p < 6$ for pulse-type motions. Using the effective period of the isolated buildings as the pulse frequency; the building contents in this study fall below that size limit and thus these results agree with their findings.

Since some of the contents do not uplift for each record the rocking spectra may give a biased representation of the effect of long period floor motion. Figure 3-11 shows the rocking spectra for the 15% damped LP isolated buildings at the roof. However, only records that induced uplift are included. The number of records (out of 20) that initiate uplift for each scenario is shown on the figure beside the corresponding line.

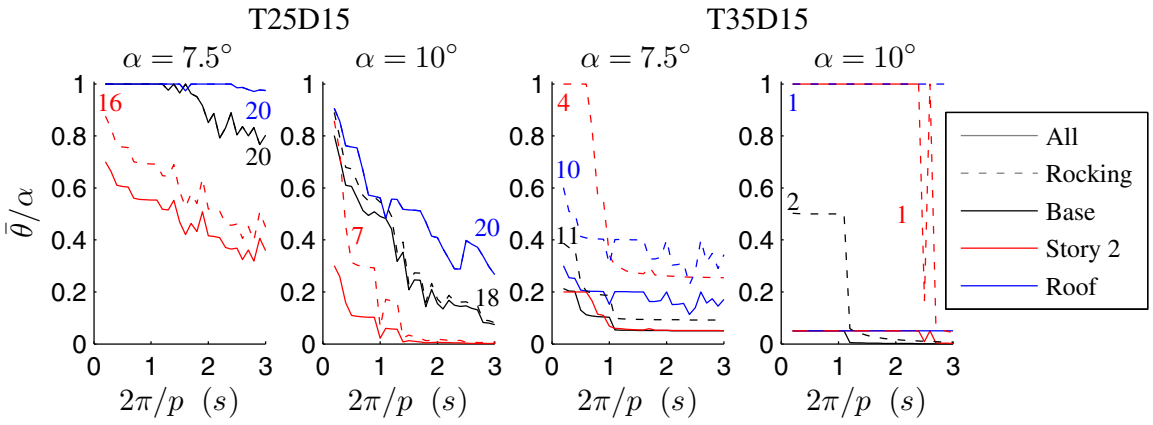

Figure 3-11. Average rocking spectra for earthquakes that induced rocking for LP systems with 15% damping for α = 7.5 and 10°

The spectra in the 2.5 s effective period isolated building do not change appreciably, compared to Figure 3-10, because most or all of the blocks uplifted; however, the second

story spectra increased slightly. The stories responses stayed in the same order within the building suggesting that not only were the lower floor accelerations responsible for the lower number of blocks uplifting, they also produced smaller rotations. The spectra in the 3.5 s period building had larger increases confirming that contents subjected to longer period excitation are more prone to overturn once uplifted. In general, the increase between spectra was also larger for smaller blocks. Even when considering only the blocks that uplifted, the spectra are still lower than those of the comparable FB building.

3.11 Comparison of the rocking response contents in buildings with different isolation systems

One of the objectives of this study was to investigate the effect of the isolation system design on the rocking of contents inside the superstructure. To do this, the rocking responses of contents with various size and slenderness, that were expected to uplift, were determined for each isolation system. Figure 3-12 shows the rocking spectra at the roof of the building for all 8 of the isolation designs considered.

In general the LP systems had higher rocking responses than the TFP systems. The largest reduction between them occurred at the roof for the systems with 2.5 s periods and 25% damping. The main reason for this can be attributed to the fact that the LP system had an 18 % higher average *PFA* and 8% higher *PFV*. For the 2.5 s period systems, the difference between the LP and TFP increased with size for the 25% damped systems but remained more constant for 15% effective damping. Interestingly for blocks with 10° slenderness, the 2.5 s period systems with 15% damping had higher responses than those with 25% damping for both types of systems (except for the LP systems with 15% damping for $2\pi/p > 1.8$ s), but for very slender objects ($\alpha = 7.5°$) the opposite was true. The 3.5 s period systems of both types were by far the most effective at reducing the rocking response. The LP system responses were typically greater for the long period systems as well, although the differences between them were reduced because of the smaller rocking responses. However, the base of the TFP 3.5 s systems had a stronger response than the LP systems due to their higher floor accelerations. The 15% damped

systems for the 3.5 s systems had higher responses for both the LP and TFP systems at all slenderness values that uplifted.

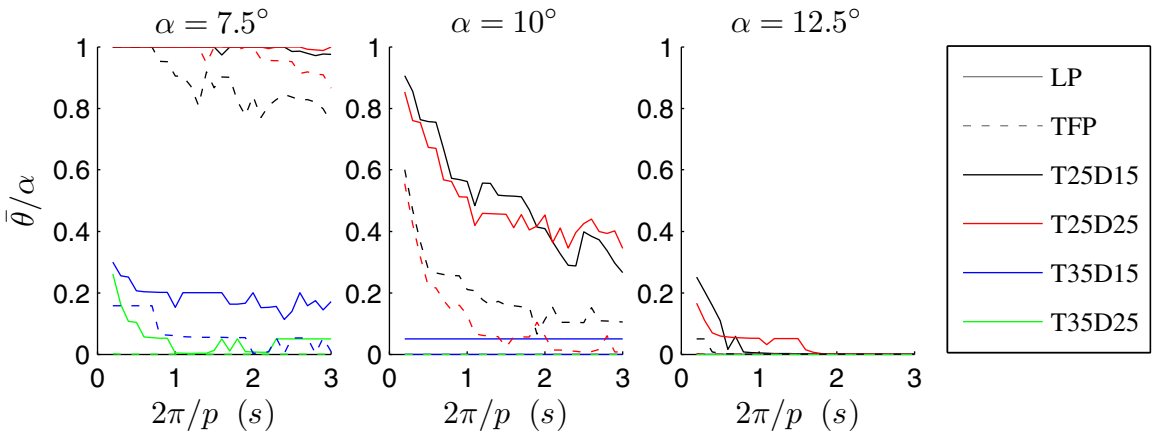

Figure 3-12. Rocking response of contents at the roof of different systems

The rocking response of an array of contents for a given acceleration record can also be shown using a boundary map. Boundary maps show the normalized rocking angle (θ/α) for each combination over a range of slenderness and size. The boundary maps for the rocking response at the base of the different LP isolation buildings are shown in Figure 3-13. The ranges shown encompass the typical size and slenderness of contents found in a building. Although α = 5° and R = 5 m are not usual, they are shown as extreme limits. Blue is indicative of overturning and dark red is no rocking.

Each square shows the average response due to the 20 ground motions. The systems with 3.5 s periods show superior protection over the 2.5 s period systems. The dark red band shifts to the left, indicating that more of the slender blocks do not uplift. This slenderness is very distinct for the system with a 3.5 s period and 25% damping at 7°. While the occurrence of uplift does not depend on size, it appears that way on some of the boundary maps because larger blocks tend to rock less and the average is close to 0. The 15% and 25% damped systems had similar rocking responses for the 2.5 s period systems, while for the the 3.5 s systems the rocking responses were larger in the 15% damped building. Overall, the higher period systems had the lower rocking responses in the typical range of building contents. Although these results are just shown for the LP system similar trends exist at in the TFP systems.

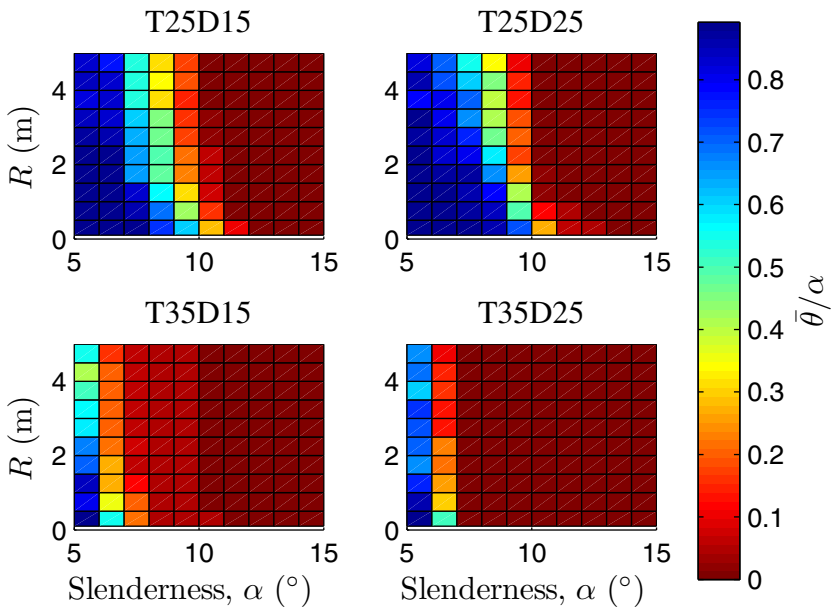

Figure 3-13. Boundary map of rocking responses at the base of the LP systems.

3.12 Variation in rocking response with floor height

Figure 3-14 shows the transition of the average rocking response up the height of the superstructure for two contents in the LP and TFP isolated buildings. The horizontal axis shows θ/α and the vertical axis is the height of the building. The two contents that are shown have sizes of p = 0.9 rad/s (R ≅15 cm) and p = 3.14 rad/s (R ≅ 75 cm) and a slenderness of 10°. The responses in the superstructure are significantly less than at the ground, which once again emphasizes the effectiveness of all the isolation systems.

The highest responses in the superstructures are located at the roof for all the systems. The second highest responses are typically located at the base of the superstructure, with a decrease at the middle of the building. This follows the general shape of the *PFA*s up the height of the building as shown in Figure 3-6. The systems with 2.5 s effective periods showed larger responses and variation across the height of the building. The rocking responses in 3.5 s effective period systems were more consistent over the height of the building although only a few of the twenty records produced uplift. This trend continues for 7.5° slenderness contents as well though, for which a greater percentage of the blocks

experience uplift. Contents in the TFP buildings generally had lower rocking responses and variation across the whole height of the building.

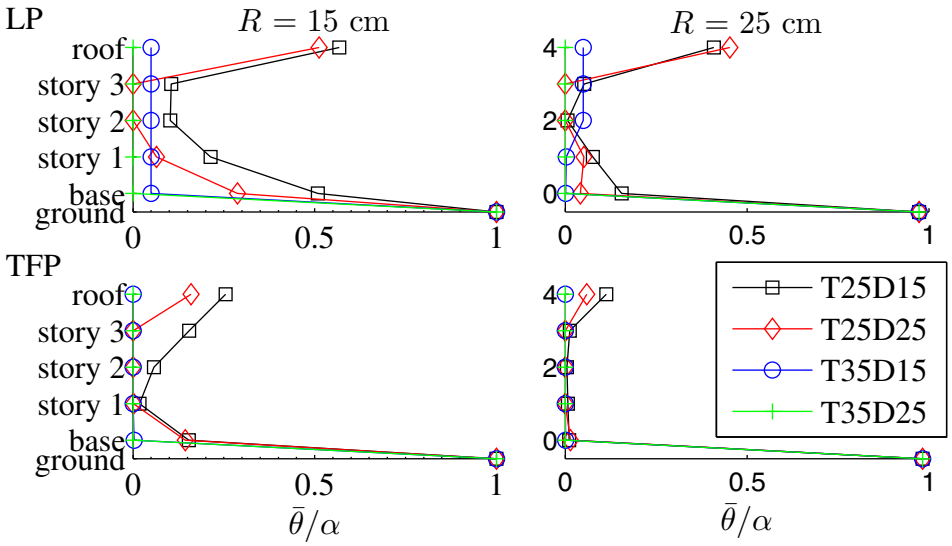

Figure 3-14. The rocking response v. height in building for two contents with $\alpha = 10°$. Top: LP buildings. Bottom: TFP buildings. Left: $R = 15$ cm, Right: $R = 75$ cm.

3.13 Fragility analysis

Another objective of this study was to equip practicing engineers with a tool to make better decisions regarding the design or performance assessment of slender nonstructural components. A tool that enables engineers to estimate the seismic response of contents in probabilistic terms is the fragility curve. Fragility curves are graphs that provide the probability of a demand parameter (*DP*) exceeding a certain damage state for a given ground motion intensity measure (*IM*). In the case of building contents, the *IM* often reflects the intensity of the floor motion, rather than the ground. Using estimates of the floor motion intensity the engineer will be able to determine the likelihood that a building content uplifts or overturns and make more informed decisions, like whether an item needs to be anchored or not.

3.13.1 Demand parameter

The *DP* is a metric used to measure the magnitude of the seismic response. For rocking this is usually taken as the absolute peak rocking rotation normalized by the slenderness,

$DP = |\theta| / \alpha$ [e.g. 50]. This dimensionless parameter is easy to understand with values of 0 indicating no rocking and values of 1 representative of overturning. Values between 0 and 1 indicate safe rocking results. This simple *DP* also lends itself to meaningful damage state values and capacity limits, *c*. This paper looks exclusively at the two extreme limit states (LS), uplift ($c = 0$) and overturning ($c = 1$), for simplicity and because these are of the most interest during design.

3.13.2 Univariate intensity measure analysis

A main concern in the development of fragility curves is the selection of an appropriate *IM*. Dimitrakopoulos and Paraskeva [50] examined various *IM*s and found the following two to be the most proficient for the rocking problem:

$$IM_1 = \frac{pPFV}{g\tan(\alpha)},\ IM_2 = \frac{PFA}{g\tan(\alpha)} \tag{3.17}$$

These *IM*s allow normalized fragility curves by encompassing blocks of all slenderness. The limit state values investigated can be classified as categorical response variables since the block either uplifts (or overturns) or it does not. Thus, a binary parameter, *z*, suffices to describe the response, with a value of 0 for no uplift (or no overturning) and 1 for uplift (or overturning).

The fragility parameters were calculated using a maximum likelihood estimation approach [51, 52]. The likelihood function for fragility parameters μ and β is given by

$$\mathrm{L}(\mu,\beta) = \prod_{j=1}^{n} \Phi\left(\frac{\ln(d_j)-\mu}{\beta}\right)^{z_j} \left(1-\Phi\left(\frac{\ln(d_j)-\mu}{\beta}\right)^{1-z_j}\right) \tag{3.18}$$

where μ and β are the mean and standard deviation of the natural logarithm of the *IM*, and *d* is a vector of the *IM* [53]. This function is then maximized in Matlab to obtain the parameters, $\hat{\mu}$ and $\hat{\beta}$, that define the statistical distribution with the highest likelihood of producing the observed data. The probability that the demand, *D*, will exceed the capacity, *C*, for a given limit state, *c*, is

$$P\left(D > C = c \,|\, IM\right) = \Phi\left(\frac{\ln(IM)-\hat{\mu}}{\hat{\beta}}\right) \tag{3.19}$$

where Φ is the cumulative distribution function of a standard normal variable. The performance of the *IM* can be directly measured by the standard deviation. The lower the standard deviation the lower the dispersion and the more efficient the *IM* is at predicting the categorical response [54]. Another performance objective, the practicality, is the slope of the linear regression of the safe rocking results on a log-log plot, γ, in

$$\ln(DP) = \ln(\rho) + \gamma \ln(IM) \tag{3.20}$$

The higher γ, the greater the correlation between the demand and the intensity and the more practical the *IM* measure is [54]. The proficiency, also known as the modified dispersion, $\xi = \beta / \gamma$, is a combination of the practicality and efficiency of the *IM*. The lower ξ, the more proficient the *IM* is [54]. The average standard deviations and proficiencies of the two *IM*s examined for both systems for uplift and overturning are shown in Table 3-6. The second *IM*, based on the *PFA*, scored low dispersions and proficiencies, while the first had relatively high values. The uplift of a block depends solely on the floor accelerations and thus a low dispersion and proficiency were expected for IM_2 for this limit. The fact that there was some dispersion at all is due to the inclusion of vertical acceleration in the rocking analysis while the *IM* only considers the horizontal excitation.

Table 3-6. Fragility parameters for uplift and overturning

		***c* = 0**				***c* = 1**			
		LP		**TFP**		**LP**		**TFP**	
$\zeta_{eff,D}$		15%	25%	15%	25%	15%	25%	15%	25%
IM_1	μ	1.52	1.81	2.41	2.65	4.20	5.09	5.88	7.38
	β	2.32	2.48	2.11	2.42	1.40	1.61	1.36	1.62
	ξ	2.33	2.52	1.74	2.71	1.41	1.64	1.12	1.81
IM_2	μ	0.93	0.93	0.96	0.94	1.24	1.21	1.29	1.26
	β	0.07	0.10	0.08	0.09	0.18	0.13	0.18	0.16
	ξ	0.00	0.01	0.01	0.01	0.01	0.01	0.01	0.02
$\widehat{IM}$	μ	0.93	0.94	0.96	0.95	1.25	1.22	1.30	1.26
	β	0.07	0.10	0.08	0.09	0.11	0.09	0.12	0.11
	λ	188	154	95.7	56.4	7.61	10.28	7.66	8.80

Interestingly, however, the acceleration-based *IM* also was more proficient than the velocity-based *IM* for the overturning limit state as well. While velocity characteristics

have traditionally been used when deriving overturning criterion [e.g. 55], Dimitrakopoulos and Paraskeva recently pointed out that rocking responses follow different scale laws for high and low intensity base excitations and that for the low level motions rocking is much more sensitive to changes in input motion characteristics [50]. They used a bi-planar distribution to fit the observed rocking data of a piece of electrical equipment under ground level pulse-type motions supplemented with high frequency content to two *IM*s; $PFA/pPFV$ and IM_2. The transition between the two planes was at a constant acceleration boundary of $PGA = 1.3g\tan(\alpha)$ with the records below this threshold dominated by IM_2. Since the majority of the analyses in the BI superstructures fall below this boundary, due to their relatively low *PFA*s, it makes sense that IM_2 provides a better fit than IM_1.

The fragility curves calculated using IM_2 are shown in Figure 3-15 for all the buildings with 2.5 s effective periods. The dashed and solid lines show the probability of uplift and overturning respectively. Unfortunately the buildings with 3.5 s effective periods did not have enough overturning responses to calculate the fragility in an unbiased and statistically significant manner.

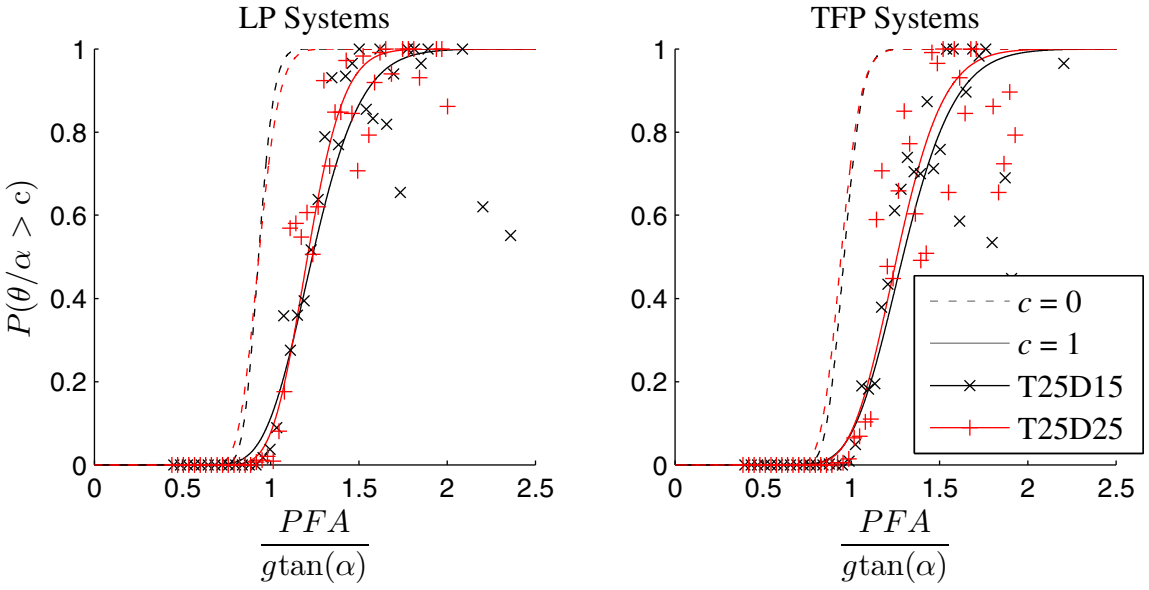

Figure 3-15. Fragility curves for superstructures with 2.5 s periods. Left: LP systems. Right: TFP systems.

Referring to μ and β for IM_2 in Table 3-6, it is evident that all the systems had similar fragility curves. This suggests the possibility of future 'universal' curves applicable to many buildings. The TFP systems had slightly lower rocking fragilities than the LP systems and the 25% damped systems had higher fragilities than the 15% damped ones for both types of isolators, although the difference was quite insignificant. This was expected from the PFAs and rocking spectra. The empirical probability of overturning was determined as the observed fraction of overturning analyses within an interval of IMs. These points are only shown for the overturning LS. The lack of close agreement of these points, shown in Figure 3-15, with the fragility curve fitted to them suggests that the univariate IM is unable to provide a strong correlation with the response.

3.13.3 Bivariate intensity measure analysis

Traditional *IM*s that work well for regular seismic demands may not work well with rocking due to the negative stiffness characteristic of rocking blocks and the lack of resonance [50]. Undoubtedly, some of the dispersion in the univariate fragility analysis is also due to the effect of block size not being taken into account. The importance of block size in the rocking problem has been noted in previous studies [14, 45]. Dimitrakopoulos and Paraskeva [50] pointed out that a more accurate statistical distribution can be achieved through the use of the bivariate intensity measure, $\widehat{IM}$,

$$\widehat{IM} = \left(\frac{PFA}{g\tan\alpha}\right)^{a_1}\left(\frac{p\,PFV}{PFA}\right)^{a_2} \tag{3.21}$$

where $a_1 = \frac{\lambda}{1+\lambda}, a_2 = \frac{1}{1+\lambda}$, and λ is an additional fragility parameter that defines the proportions of the univariate *IM*s in $\widehat{IM}$. This intensity measure is a linear combination in logarithmic space of the best slenderness-based and frequency-ratio-based dimensionless intensity measures that they investigated

$$\ln\left(\widehat{IM}\right) = \frac{\lambda}{1+\lambda}\ln\left(\frac{PFA}{g\tan\alpha}\right) + \frac{1}{1+\lambda}\ln\left(\frac{pPFV}{PFA}\right) \tag{3.22}$$

The bivariate intensity measure is also assumed to be lognormally distributed so that the probability of exceedance of a limit state is described by the cumulative distribution function

$$P\left(D > C = c \,|\widehat{IM}\right) = \Phi\left(\frac{\ln\left(\widehat{IM}\right) - \hat{\mu}}{\hat{\beta}}\right) \tag{3.23}$$

The maximum likelihood estimation method is again employed to find the parameters ($\hat{\mu}$, $\hat{\beta}$, λ) that maximize the probability of the statistical distribution producing the actual results. Table 3-6 also lists the average of the standard deviations of the fragility curves derived using the bivariate $\widehat{IM}$ for each system. As expected, supplementing the slenderness-based IM (i.e., $PFA/\left(g\tan\alpha\right)$) with a frequency-ratio-based IM ($pPFV/PFA$) reduced the standard deviation for the overturning LS. The standard deviation for the uplift LS remained constant because it is deterministic on IM_2 which for the bivariate $\widehat{IM}$ is characterized by very high λ. For both types of isolators the 15% damped systems had a higher λ, i.e., a stronger dependence on the frequency-based IM ($pPFV/PFA$). The bivariate fragility curves for all the 2.5 second systems are shown in Figure 3-16.

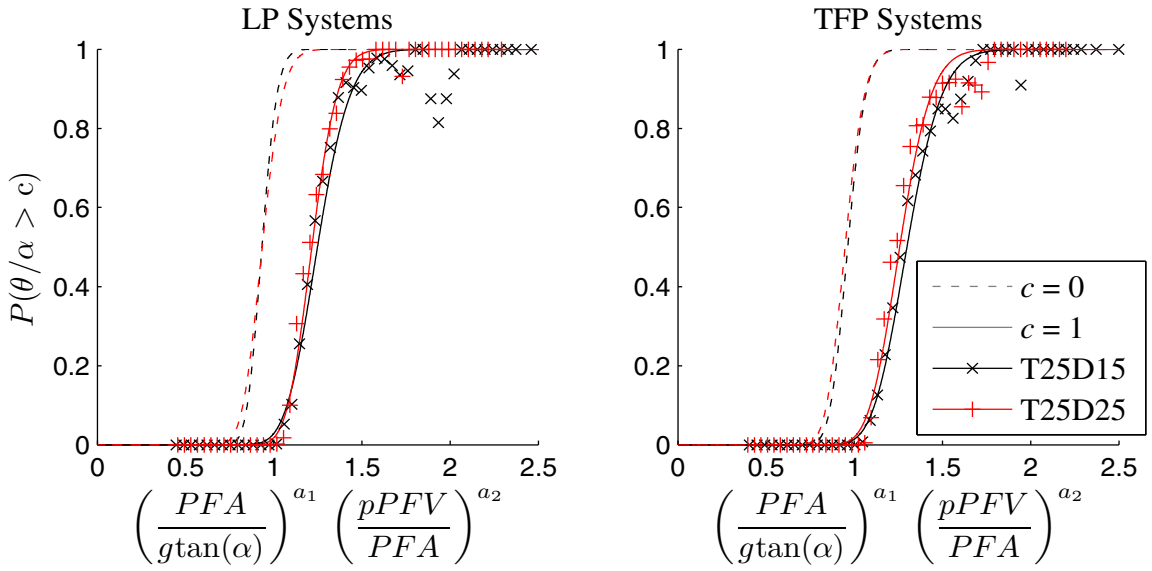

Figure 3-16. Bivariate fragility curves. Left: LP systems. Right: TFP systems.

The data points representing the percentage of the analysis overturning for a specific interval strip of *IM*s are again shown. The fragility function fits the observed cases better in the case of the bivariate $\widehat{IM}$ (Figure 3-16) than univariate (Figure 3-15) as a result of more ordered results and lower standard deviations. In general, the bivariate $\widehat{IM}$ was able to create fragilities which offer superior predictions of the rocking responses.

3.14 Conclusions

The main objective of this study was to investigate the effectiveness of base isolation in protecting slender freestanding building contents from uplift and overturning. Models of a FB building and a variety of BI buildings were created in OpenSees and subsequently subjected to nonlinear time-history analyses to obtain floor acceleration records. These were then used as input to determine the rocking response of contents with a wide range of size and slenderness at different levels in the buildings. Various LP and TFP isolation systems were studied, and the rocking response of contents in the different superstructures was contrasted. All of the base isolation systems were very effective at reducing the *PFA*s. Consequently, base isolation greatly increases the threshold content slenderness that will not rock, thereby protecting stockier blocks that would otherwise uplift in the FB building. For the slender contents that did uplift in the BI buildings, the peak rotation was significantly lower than in the FB building. The base isolation systems with higher effective periods had considerably lower rocking responses. The systems with higher effective damping also tended to have lower rocking responses, although the difference was not as significant. The rocking responses in the TFP isolated superstructures were usually somewhat lower when compared to the equivalent LP ones depending on the story. Fragility curves for uplift and overturning were created using a bivariate *IM* which was shown to produce superior results than the univariate *IM*s investigated.

Unfortunately, this study also has limitations that restrict the applicability of its results. One of the main limitations is the simplification to two dimensions. In an actual earthquake scenario, both the building and its contents will exhibit complex 3D motions, whereas in this paper the analysis is restricted to planar motion for both the buildings and

their contents. Also, only one superstructure was investigated for all isolation systems, although it is possible that the results may be affected by the various design characteristics of the superstructure. Limitations on the actual rocking analysis include the assumption of rigidness of the block and the floor, and the assumption that there is pure rocking, i.e., no sliding. Also, the analyses were only completed using the maximum coefficient of restitution, whereas the actual value is dependent on the material properties of the floor and content and a lower coefficient will alter the rocking response. The results here can be viewed as generally conservative in this regards.

3.15 References

1. Kircher C.A. It makes dollars and sense to improve nonstructural system performance. *Proceedings of ATC 29-2 Seminar of Seismic Design, Performance, and Retrofit of Nonstructural Components in Critical Facilities*, Newport Beach, CA, 2003; 109–120
2. Fierro E.A, Miranda E, Perry C.L, Lynn A.C, Reitherman R. Behavior of nonstructural components in recent earthquakes. *Proceedings of the Architectural Engineering National Conference*, Oakland, CA, 2011.
3. Taghavi S, Miranda E. Response assessment of nonstructural building elements. *Pacific Earthquake Engineering Research Center, University of California*, Berkeley, 2003.
4. Linde S, Konstantinidis K, Tait M. Rocking response of unanchored building contents. To be submitted to *Earthquake Engineering and Structural Dynamics,* August 2016.
5. Sankaranarayanan, R. Seismic response of acceleration sensitive non-structural components mounted on moment resisting frame structures. Ph.D. University of Maryland, 2007.
6. John D, Gillengerten, S.E. *"Design of nonstructural systems and components" in The Seismic Design Handbook, Second Edition*. Boston: Kluwer Academic Publishers, 2001. Chpt 13.
7. Becker T.C, Mahin S.A. Approximating peak responses in seismically isolated buildings using generalized modal analysis. *Earthquake Engineering and Structural Dynamics* 2013; **42**(12):1807–1825.
8. Wolff E.D, Ipek C, Constantinou M.C, Tapan M. Effect of viscous damping devices on the response of seismically isolated structures. *Earthquake Engineering and Structural Dynamics* 2015; **44**(2):185–198.
9. Van Engelen N.C, Konstantinidis D, Tait M.J. Structural and nonstructural performance of a seismically isolated building using stable unbonded fiber-reinforced

elastomeric isolators. *Earthquake Engineering and Structural Dynamics* 2016; **45**(3):421–439.

10. Shi Y, Kurata M, Nakashima M. Disorder and damage of base-isolated medical facilities when subjected to near-fault and long-period ground motions. *Earthquake Engineering and Structural Dynamics* 2014; **43**(11):1683–1701.
11. Soroushian S, Maragakis E.M, Ryan K.L, Sato E, Sasaki T, Okazaki T, Mosqueda G. Seismic simulation of an integrated ceiling-partition wall-piping system at E-Defense. II: Evaluation of nonstructural damage and fragilities. *Journal of Structural Engineering* 2016; **142**(2).
12. Pantoli E, Chen M.C, Hutchinson T.C, Astroza R, Conte J.P, Ebrahimian H, Restrepo J.I, Wang X. Landmark dataset from the building nonstructural components and systems (BNCS) project. *Earthquake Spectra* 2016; **32**(2):1239–1259.
13. Konstantinidis D, Nikfar F. Seismic response of sliding equipment and contents in base-isolated buildings subjected to broadband ground motions. *Earthquake Engineering and Structural Dynamics* 2015; **44** (6), 865–887.
14. Housner G.W. The behavior of inverted pendulum structures during earthquakes. *Bulletin of the Seismological Society of America* 1963; **53**: 403–417.
15. Vassiliou M.F, Makris N. Analysis of the rocking response of rigid blocks standing free on a seismically isolated base. *Earthquake Engineering and Structural Dynamics* 2012; **41**(**2**): 177–196.
16. Contento A, Di Egidio A. Investigations into the benefits of base isolation for non-symmetric rigid blocks. *Earthquake Engineering and Structural Dynamics* 2009; **38** (**7**) : 849 –866.
17. Cali`o I, Marletta M. Passive control of the seismic response of art objects. *Engineering Structures* 2003; **25**:1009–1018.
18. Vestroni F, Di Cinto S. Base isolation for seismic protection of statues. *Twelfth World Conference on Earthquake Engineering*, New Zealand, 2000.

19. Roussis P.C, Odysseos S. Dynamic response of seismically isolated rigid blocks under near-fault ground motions. *Proceedings of the 15th World Conference on Earthquake Engineering*, Lisboa, 2012.
20. USGS 2014, U.S. Seismic design maps, U.S. Geologic Survey, Reston, VA
21. American Society of Civil Engineers (ASCE). Minimum design loads for buildings and other structures, ASCE7-10, Reston, VA, 2010.
22. ANSI/AISC 360-10. *Specification for structural steel buildings*. Chicago, IL: American Institute of Steel Construction; 2010.
23. Higashino M. *Response Control and Seismic Isolation of Buildings*. Taylor and Francis Group, 2006.
24. RobinsonW.H. Lead rubber hysteretic bearings suitable for protecting structures during earthquakes. *Earthquake Engineering and Structural Dynamics*, **10** (4) (1982), pp. 593–604
25. Sun W. Performance assessment and design of lead rubber seismic isolators using a bilinear spectrum method. MaSc. McMaster University. 2011.
26. Skinner R.I, Robinson W.H, McVerry G.H. *An introduction to seismic isolation*. Wiley: Chichester, 1993.
27. Naiem F, Kelly J. *Design of Seismic Isolated Structures: From Theory to Practice*. John Wiley and Sons Inc. 1999.
28. Becker T. Advanced modeling of the performance of structures supported on triple friction pendulum bearings. PhD. University of California. 2011.
29. Nikfar F, Konstantinidis D. Shake table investigation on the seismic performance of hospital equipment supported on wheels/casters. *Earthquake Engineering and Structural Dynamics* 2016 [in press].
30. McKenna F, Fenves G.L, Scott M.H. Open system for earthquake engineering simulation (OpenSees). Accessed 2015.
31. Hsiao P-C, Lehman, D.E, Roeder C.W. Improved analytical model for special concentrically braced frames. *Journal of Constructional Steel Research* 2012; **73**: 80–94.

32. Erduran E, Dao N, Ryan K. Comparative response assessment of minimally compliant low-rise conventional and base-isolated steel frames. *Earthquake Engineering and Structural Dynamics* 2011; **40**:1123–1141.
33. Hall J.F. Problems encountered from the use (or misuse) of Rayleigh damping. *Earthquake Engineering and Structural Dynamics* 2006; **35**(5):525–540.
34. Yang Q.R, Liu W.G, He W.F, Feng D.M. Tensile stiffness and deformation model of rubber isolators in tension and tension-shear states. *Journal of Engineering Mechanics (ASCE)*.2010; **136**(4):429–437.
35. Dao N.D, Ryan K.L, Sato E, Sasaki T. Predicting the displacement of triple pendulum bearings in a full-scale shaking experiment using a three-dimensional element. *Earthquake Engineering and Structural Dynamics*, 2013; **42**(11): 1677–1695.
36. Earthquake Protection Systems. Technical characteristics of friction pendulum systems. 2005.
37. Dao N. Triple friction pendulum element. *OpenSees*. Accessed March 9, 2015.
38. Baker J, Lin T, Shahi S, Jayaram N. New ground motion selection procedures and selected motions for the PEER transportation research program. *Report No. PEER* 2011-03*, Pacific Earthquake Engineering Research Center*, University of California, Berkeley, CA. 2011.
39. Boore D.M, Atkinson G.M. Ground-motion prediction equations for the average horizontal component of PGA, PGV, and 5%-damped PSA at spectral periods between 0.01 s and 10.0 s. *Earthquake Spectra*, 2008; **24**(1), 99–138.
40. USGS, 2008. Seismic hazard analysis tools – Interactive disaggregation. U.S. Geologic Survey, Reston ,VA.
41. Vasant A, Matsagar, Jangid R.S. Influence of isolator characteristics on the response of base-isolated structures. *Engineering Structures* 2004; **26**(12): 1735–1749.
42. Soleimanloo H.S. A survey study on design procedure of seismic base isolation systems. *Journal of Applied Sciences and Environmental Management* 2012; **16**(4)299–307.

43. Mavronicola E, Komodromos P. Assessing the suitability of equivalent linear elastic analysis of seismically isolated multi-storey buildings. *Computers and Structures* 2011; **89**(21):1920–1931.
44. Tolani S, Sharma A. Effectiveness of base isolation technique and influence of isolator characteristics on response of a base isolated building. *American Journal of Engineering Research* 2016; **5**(5):198–209.
45. Yim C, Chopra A.K, Penzien J. Rocking response of rigid blocks to earthquakes, *Earthquake Engineering and Structural Dynamics* 1980; **8**: 565–587.
46. Dimentberg M.F, Lin Y.K, Zhang R. Toppling of computer-type equipment under base excitation. *Journal of Engineering Mechanics, ASCE*, 1993; **119**(1), 145–160.
47. Shi B, Anooshehpoor A, Zeng Y, Brune J. Rocking and overturning of precariously balanced rocks by earthquake. *Bulletin of the Seismological Society of America* 1996; **86**(5): 1364–1371.
48. Konstantinidis D. Experimental and analytical studies on the seismic response of freestanding and anchored building contents. PhD. University of California, Berkeley. 2008.
49. Makris N, Konstantinidis D. The rocking spectrum and the limitations of practical design methodologies. *Earthquake Engineering and Structural Dynamics* 2003; **32**(2):265–289.
50. Dimitrakopoulos E.G, Paraskeva T.S. Dimensionless fragility curves for rocking response to near-fault excitations. *Earthquake Engineering and Structural Dynamics* 2015, **44**(12); 2015–2033.
51. Shinozuka M, Feng M.Q, Lee J, Naganuma T. Statistical analysis of fragility curves. *Journal of Engineering Mechanics* 2000; **126**(12):1224–1231.
52. Mandal T.K, Pujari N, Ghosh S. A comparative study of seismic fragility estimates using different numerical methods. *In 4th ECCOMAS Thematic Conference on Computational Methods in Structural Dynamics and Earthquake Engineering (COMPDYN)*, Kos Island, Greece. 2013.

53. Baker J. Efficient analytical fragility function fitting using dynamic structural analysis. *Earthquake Spectra,* 2013; **31**(1): 579–599.
54. Padgett J.E, Nielson B.G, DesRoches R. Selection of optimal intensity measures in probabilistic seismic demand models of highway bridge portfolios. *Earthquake Engineering and Structural Dynamics* 2008; **37**(5):711–725.
55. Makris N, Roussos Y. Rocking response and overturning of equipment under horizontal pulse-type motions *Rep. No. PEER-98/05*, Pacific Earthquake Engineering Research Center., University of California, Berkeley, California. 1998.

Chapter 4: Conclusions and Recommendations

4.1 Summary

The continued operability of critical facilities such as hospitals, fire stations, and government buildings succeeding an earthquake is fundamental to the goal of creating robust communities. Often the reason for these critical facilities experiencing downtime after an earthquake is due to the failure and damage of nonstructural components. However, the focus of earthquake engineering research and design is vastly lopsided toward the structural response, with the seismic response of nonstructural contents receiving significantly less attention. Part of the reason for this is the difficulty associated with not only predicting their response, but also implementing the knowledge of it as it contributes towards performance driven design. Wide information gaps exist in literature regarding the response of building contents. Rigid slender contents and equipment respond primarily in rocking during an earthquake. Rocking is one of the most adverse modes of response an object can experience during an earthquake due to the intense acceleration spikes at impact and the danger and damage associated with overturning. This study evaluated the rocking response of building contents in fixed and BI buildings.

Base isolation is a well-studied technique that is used to protect both structural and nonstructural building components. In North America it is typically used in high seismicity regions for critical facilities or where the contents vastly out-value the structure, as in museums. However, this thesis is among the first to examine the rocking response of freestanding equipment and contents in isolated buildings. It has showed the overall effectiveness of base isolation as a rocking mitigation technique.

The main objective of this thesis was to create a better understanding of the rocking vulnerability of building contents with the goal of minimizing potential risks. The new knowledge presented will allow designers to estimate the rocking response of contents in similar structures and determine the need for protection systems like anchoring. This benefits designers because it allows them the freedom to avoid anchoring where possible when it is not an ideal solution due to cost and mobility restrictions. Anchoring can also lead to higher accelerations in contents that would respond in either sliding or rocking. In

addition to the actual quantification of rocking responses, this thesis has presented general trends that may hold true for more than just the buildings examined. These trends may be useful during decisions regarding content placement or for selecting dimensions while designing the contents themselves. This thesis also furthers the advancement of performance based earthquake engineering because it facilitates assessments of probable damage and therefore replacement costs.

4.2 Rocking response of FB building contents

In Chapter 2 the rocking response of contents within a FB SCBF hospital located in Los Angeles was examined. The four story hospital was designed according to ASCE 7-10 using chevron braces with zipper columns. A 3D OpenSees model of one bay width of the hospital was created and used to run time history analysis. The model included all the structural elements as well as the floor slab. The slab was included to capture the vertical accelerations at locations other than the columns. A suite of twenty broadband strong ground motions with both horizontal and vertical components was selected to match the target spectrum and scaled to the DBE level. The floor accelerations at five locations throughout one bay at each floor level were recorded. The horizontal accelerations increased toward the top of the structure and were dominated by the first mode. The vertical accelerations were lowest at the column and increased towards the center of the bay. These excitations were then used as input to determine the rocking response of contents. The rocking time histories were obtained by solving the equation of motion using ODE solvers in Matlab. The response of many different size and slenderness objects were determined in this method. The peak rocking responses from all these analyses were then used to create rocking spectra. These spectra were used to compare and contrast rocking in different locations throughout the building as well as the effects of size and slenderness.

It was demonstrated that the inclusion of the vertical component of the ground acceleration had little effect on the rocking response of contents within the building. This held true even for contents located near the center of the slab at the top of the building where the vertical accelerations were at a maximum. The result of the vertical

accelerations having no significant effect is that contents at different floor locations all had similar responses. The noteworthy conclusion from this is that the placement of a given item on a floor level is inconsequential to its rocking response. However, the inclusion of the vertical motion also enabled the object to lift off the floor. This was monitored by tracking the normal force at the toe of the block during rocking. Intuitively, jumping was more prevalent in areas of higher vertical accelerations; i.e. nearer the roof and towards the center of the slab. In this regard the placement of the item on a given floor mattered as no objects placed near the column jumped. Neither the size nor slenderness of the content significantly affected its likelihood to jump.

The effect of content height within the building was also examined. As expected for stocky blocks ($\alpha = 20°$) the rocking response increased up the height of the building. The differences in responses between adjacent floors decreased towards the roof. For mid-slenderness blocks ($\alpha = 15°$) the responses also increased up the building although there was less difference between the stories than for the stocky blocks. Interestingly, the rocking spectra for slender blocks ($\alpha = 10°$) was similar at all of the stories. The implication of this is that for slender contents the placement within a building has little discernible effect on its rocking response. The same result held true when the slender blocks were investigated with a coefficient of restitution corresponding to the maximum for the stocky blocks. Another conclusion from the rocking spectra is that the response of stockier objects is more sensitive to the size of the block. The smaller stocky contents experienced the largest increases in responses up the building.

The data was then used to create fragility curves for use by designers. The demand parameter was taken as the peak rocking angle normalized by the slenderness. The dimensionless intensity measure used was a function of both the size and slenderness of the block as well as the peak floor velocity. Fragility curves were created using linear regression and maximum likelihood estimation for three limit states corresponding to minor rocking, the inflection point in the period of free rocking, and overturning. The significance of these curves is that they allow a designer or retrofitter to estimate the

probability of a content or piece of equipment to exceed one of the limit states given that they know its dimensions and can estimate a peak floor velocity.

4.3 Rocking response of BI building contents

Chapter 3 follows the same format as chapter 2 except that the focus is on the rocking response of contents in BI buildings. A BI superstructure was designed for Los Angeles and modeled in OpenSees. Because of the conclusions regarding the negligible influence of vertical motion it was only modeled in 2D. Two types of isolators were used to isolate the superstructure, triple friction pendulum bearings (TFPs) and elastomeric lead plug bearings (LPs). The two types of isolators were designed with equivalent design displacements and effective damping so that a fair comparison could be made. Four different designs were considered for each type of isolator with varying effective periods and damping. The same superstructure was used for all 8 buildings and was designed for the isolation system with the highest corresponding base shear coefficient. The same ground excitations were used as in chapter 2. They were scaled to the design spectra for a range of periods encompassing the expected periods of the FB and BI buildings so that an unbiased comparison could be made. The floor accelerations were recorded at each story and remained fairly uniform across the height of the BI superstructures with the dominant frequencies corresponding to the initial stiffness and effective design stiffness. The roof and base experienced slightly larger floor responses due to second mode effects. The rocking response of various size and slenderness contents was then determined for all the superstructures.

In general base isolation was very effective at reducing the rocking response of building contents. All the isolation systems were able to significantly lower the maximum slenderness of contents that would uplift when compared to the FB buildings. This was due to the reduction in peak floor accelerations. The longer period systems were more effective in this regard for the same reason. Rocking spectra for the BI buildings' were compared to the rocking spectra from the FB building for contents with slendernesses that were expected to uplift given the previous results. Even when only considering blocks that uplifted the isolation systems were still found to significantly reduce rocking despite

the long period motion that was expected to act as a static force and overturn blocks once they started to rock. The only instance in which the isolation systems amplified the response was for very slender (α = 7.5°) large contents at the roof of the building.

Another objective of this chapter was to compare the effectiveness of the different isolation system types and designs at minimizing the rocking response. The TFP systems had slightly lower mean peak floor accelerations and velocities than the equivalent LP systems which resulted in lower rocking responses as well. However, the TFP isolated superstructures with 3.5 second effective periods had higher responses at the base. The systems with longer effective periods had significantly lower responses. The effective damping had less of an effect on the rocking responses than the isolation system period. For most of the systems, the higher damped systems had marginally lower responses. However, for the shorter period systems for some of the slendernesses the lower damped systems had slightly lower rocking spectra. Compared to the FB building the rocking response of a given object in the isolated building is fairly consistent up the height of the building. The largest responses occur at the roof and base in keeping with the distribution of *PFA*s up the height of the superstructure.

Fragility curves were also created for the BI buildings with isolation systems with 2.5 s effective periods. Unfortunately the longer period systems did not produce enough rocking data to be able to create statistically significant fragility curves. Two dimensionless univariate *IM*s based on *PFA* and *PFV* that were investigated. Contrary to the FB case, the *PFA* based *IM* produced much better performance. This is because rocking scales differently for low and high intensity motion. The floor accelerations in the BI buildings for rocking blocks were typically only marginally greater than the acceleration needed for uplift and the results corresponded with the *PFA*. A bivariate *IM* that combined two *IM*s that included both *PFA* and *PFV* was also used to provide superior fragility curves.

4.4 Recommendations and future study

The main recommendation of this study is to consider the seismic response of building contents during the design of the building. The fragility curves presented in this thesis and

future research can be used to determine the vulnerability of contents to uplift or rocking and consequently make informed decisions. This will allow simple mitigation techniques like anchoring or isolation for individual objects to be employed where necessary to reduce injury and economic loss resulting from an earthquake. Another general recommendation is to control the *PFV*s during the design of FB buildings as they were found to drive overturning. Also, expensive objects should be located near columns or on lower stories to reduce the risk of jumping.

For buildings where the protection of building contents is a primary objective during the design phase, such as in hospitals and museums where the contents far out-value the structure, base isolation is a valuable and effective technology. The lowest rocking responses were in the superstructures with the lowest *PFA*s which for this study occurred in the TFP isolated buildings. The longer period systems are more effective despite the pulse-type motion which was only detrimental in very rare cases. The downside of these systems is that they have higher displacements and a larger moat is needed. Some of this displacement can be controlled through damping as this study found that the effective damping of otherwise similar isolation systems had little effect on the rocking responses in the superstructures.

This thesis was one of the first pieces of literature to study the rocking response of building contents using the floor motions as input. More work is definitely needed in this area because of the highly nonlinear nature of both the buildings behaviour under seismic loading and the rocking response. One area that this work should focus on is using a wider variety of buildings with different heights and lateral force resisting systems to obtain floor motions. An interesting study would be to examine the effects of including the floor rotations in the equations of motion. Floor rotational motion can be produced by the flexure of floor slabs excited by vertical motion or the deflection of beams in moment resisting frame. Including these rotations while solving the rocking motion may increase the likelihood of uplift and overturning. Another ongoing valuable area of research is expanding the response model to encompass more than just pure rocking. Currently there are accurate 2D slide-rock models that predict the response of objects in either or both of

these responses. However, the response of building contents is fundamentally a 3D problem. Models should continue to be developed so that eventually solving the response time history of any object in 3D is attainable. This involves a lot of complexity as it greatly increases the possible number of response modes to include 3D motions like twisting. However, the benefit of such a model is that it would predict the actual response of an object with greater certainty and lead to better designs.

Appendix A

Derivation of coefficients of friction

There are two pertinent coefficients of friction governing the rocking motion; the first is the coefficient of friction required at the moment rocking initiates and the second is the coefficient necessary for rocking to continue without sliding at each timestep. They are both derived below.

Sustained Rocking

The condition to prevent sliding can be written at any given time step during the rocking analysis as

$$\left|f_x\right| \le \left|f_y\right| \mu_s \tag{A.1}$$

Or conversely

$$\mu_s \ge \left|\frac{f_x}{f_y}\right| \tag{A.2}$$

Where

μ_s = Static coefficient of friction

f_x = Horizontal friction force

f_y = Normal force

The following two equations for can be written for f_x and f_y by applying dynamic equilibrium on the block.

$$f_x = m\left(\ddot{\bar{x}} + \ddot{U}_f^x\right) \tag{A.3}$$

$$f_y = m\left(\ddot{\bar{y}} + \ddot{U}_f^y + g\right) \tag{A.4}$$

Let

$$\delta = \alpha - \left|\theta\right| \tag{A.5}$$

Then the position of the center of mass can be written as

$$\bar{x} = \mathrm{sgn}\left(\theta\right)\left\{b - R\sin\left(\delta\right)\right\} \tag{A.6}$$

$$\overline{y} = R\cos(\delta) \tag{A.7}$$

The relative acceleration of the center of mass with respect to the rocking corner is obtained by twice differentiating these equations and is given by

$$\ddot{\overline{x}} = R\ddot{\theta}\cos(\delta) + \text{sgn}(\theta) R\dot{\theta}^2 \sin(\delta) \tag{A.7}$$

$$\ddot{\overline{y}} = R\,\text{sgn}(\theta)\ddot{\theta}\sin(\delta) - R\dot{\theta}^2\cos(\delta) \tag{A.8}$$

Sub Equations (A.7) and (A.8) into Equations (A.3) and (A.4) and then into Equation (A.2) to get

$$\mu_s \geq \left| \frac{R\ddot{\theta}\cos(\delta) + \text{sgn}(\theta) R\dot{\theta}^2 \sin(\delta) + \ddot{U}_f^x}{R\,\text{sgn}(\theta)\ddot{\theta}\sin(\delta) - R\dot{\theta}^2\cos(\delta) + \ddot{U}_f^y + g} \right|; \tag{A.9}$$

Then sub the equation of motion given in Equation (A.10) into Equation (A.9) to get Equation (A.11)

$$\ddot{\theta} = -p^2 \left\{ \left(1 + \frac{\ddot{U}_f^y}{g} \right) \text{sgn}(\theta)\sin(\delta) + \frac{\ddot{U}_f^x}{g}\cos(\delta) \right\} \tag{A.10}$$

$$\mu_s \geq \left| \frac{-p^2 R \left\{ \left(1 + \frac{\ddot{U}_f^y}{g} \right) \text{sgn}(\theta)\sin(\delta) + \frac{\ddot{U}_f^x}{g}\cos(\delta) \right\} \cos(\delta) + \text{sgn}(\theta) R\dot{\theta}^2 \sin(\delta) + \ddot{U}_f^x}{-p^2 R\,\text{sgn}(\theta) \left\{ \left(1 + \frac{\ddot{U}_f^y}{g} \right) \text{sgn}(\theta)\sin(\delta) + \frac{\ddot{U}_f^x}{g}\cos(\delta) \right\} \sin(\delta) - R\dot{\theta}^2\cos(\delta) + \ddot{U}_f^y + g} \right| \tag{A.11}$$

Rearrange to get

$$\mu_s \geq \left| \frac{-\left(1 + \frac{\ddot{U}_f^y}{g} \right) \text{sgn}(\theta)\sin(\delta)\cos(\delta) - \frac{\ddot{U}_f^x}{g}\cos^2(\delta) + \text{sgn}(\theta)\frac{\dot{\theta}^2}{p^2}\sin(\delta) + \frac{4\ddot{U}_f^x}{3g}}{-\left(1 + \frac{\ddot{U}_f^y}{g} \right)\sin^2(\delta) - \text{sgn}(\theta)\frac{\ddot{U}_f^x}{g}\cos(\delta)\sin(\delta) - \frac{\dot{\theta}^2}{p^2}\cos(\delta) + \frac{4\ddot{U}_f^y}{3g} + \frac{4}{3}} \right| \tag{A.12}$$

Sub Equations (A.13) into Equation (A.12) and remember the trigonometric identities given in Equation (A.14) – (A.16) to get Equation (A.17)

$$p^2 = \frac{3g}{4R} \tag{A.13}$$

$$\sin(\alpha)\cos(\alpha) = \frac{1}{2}\sin(2\alpha) \tag{A.14}$$

$$\cos^2(\alpha) = \frac{1}{2}(1+\cos(2\alpha)) \tag{A.15}$$

$$\sin^2(\alpha) = \frac{1}{2}(1-\cos(2\alpha)) \tag{A.16}$$

$$\mu_s \geq \left| \frac{-\frac{1}{2}\left(I+\frac{\ddot{U}_f^y}{g}\right)\mathrm{sgn}(\theta)\sin(2\delta) - \frac{\ddot{U}_f^x}{2g}(1+cos(2\delta)) + \mathrm{sgn}(\theta)\frac{\dot{\theta}^2}{p^2}\sin(\delta) + \frac{4\ddot{U}_f^x}{3g}}{-\frac{1}{2}\left(1+\frac{\ddot{U}_f^y}{g}\right)(1-\cos(2\delta)) - \mathrm{sgn}(\theta)\frac{\ddot{U}_f^x}{2g}\sin(2\delta) - \frac{\dot{\theta}^2}{p^2}\cos(\delta) + \frac{4\ddot{U}_f^y}{3g} + \frac{4}{3}} \right| \tag{A.17}$$

Rearrange

$$\mu_s \geq \left| \frac{\ddot{U}_f^x(5-3\cos(2\delta)) - 3\mathrm{sgn}(\theta)(\ddot{U}_f^y+g)\sin(2\delta) + 8\mathrm{sgn}(\theta)R\dot{\theta}^2\sin(\delta)}{3(\ddot{U}_f^y+g)(\cos(2\delta)-1) - 3\mathrm{sgn}(\theta)\ddot{U}_f^x\sin(2\delta) - 8R\dot{\theta}^2\cos(\delta) + 8\ddot{U}_f^y + 8g} \right| \tag{A.18}$$

Sub Equation (A.5) back into Equation (A.18) to obtain the coefficient of friction needed in order to prevent sliding throughout the duration of rocking.

$$\mu_s \geq \left| \frac{\ddot{U}_f^x(5-3\cos(2(\alpha-|\theta|))) - 3\mathrm{sgn}(\theta)(\ddot{U}_f^y+g)\sin(2(\alpha-|\theta|)) + 8\mathrm{sgn}(\theta)R\dot{\theta}^2\sin(\alpha-|\theta|)}{3(\ddot{U}_f^y+g)(\cos(2(\alpha-|\theta|))-1) - 3\mathrm{sgn}(\theta)\ddot{U}_f^x\sin(2(\alpha-|\theta|)) - 8R\dot{\theta}^2\cos(\alpha-|\theta|) + 8\ddot{U}_f^y + 8g} \right| \tag{A.19}$$

Initiation of Rocking

The coefficient of friction needed for the initiation of rocking can be determined from Equation (A.19) by solving it for the moment of uplift.

At uplift, for $\ddot{U}_f^x > 0$

$$\theta = 0^- \tag{A.20}$$

$$\dot{\theta} = 0 \tag{A.21}$$

$$\ddot{\theta} < 0 \tag{A.22}$$

Sub Equations (A.20) – (A.22) into Equation (A.19) to get

$$\mu_s \geq \left| \frac{\left|\ddot{U}_f^x\right|\left(5-3\cos\left(2\alpha\right)\right)+3\left(\ddot{U}_f^y+g\right)\sin\left(2\alpha\right)}{3\left(\ddot{U}_f^y+g\right)\left(\cos\left(2\alpha\right)-1\right)+3\left|\ddot{U}_f^x\right|\sin\left(2\alpha\right)+8\ddot{U}_f^y+8g} \right| \tag{A.23}$$

For $\ddot{U}_f^x < 0$

$$\theta = 0^+ \tag{A.24}$$

$$\dot{\theta} = 0 \tag{A.25}$$

$$\ddot{\theta} > 0 \tag{A.26}$$

Sub Equations (A.24) – (A.26) into Equation (A.19) to get

$$\mu_s \geq \left| \frac{-\left|\ddot{U}_f^x\right|\left(5-3\cos\left(2\alpha\right)\right)-3\left(\ddot{U}_f^y+g\right)\sin\left(2\alpha\right)}{3\left(\ddot{U}_f^y+g\right)\left(\cos\left(2\alpha\right)-1\right)+3\left|\ddot{U}_f^x\right|\sin\left(2\alpha\right)+8\ddot{U}_f^y+8g} \right| \tag{A.27}$$

Equations (A.23) and (A.27) can be combined to give the coefficient of friction needed for rocking to initiate as shown in Equation (A.28)

$$\mu_s \geq \left| \frac{\left|\ddot{U}_f^x\right|\left(5-3\cos\left(2\alpha\right)\right)+3\left(\ddot{U}_f^y+g\right)\sin\left(2\alpha\right)}{3\left(\ddot{U}_f^y+g\right)\left(\cos\left(2\alpha\right)-1\right)+3\left|\ddot{U}_f^x\right|\sin\left(2\alpha\right)+8\ddot{U}_f^y+8g} \right| \tag{A.28}$$

If there are no vertical accelerations, Equations (A.19) and (A.28) reduce to Equations (A.29) and (A.30) respectively.

$$\mu_s \geq \left| \frac{\frac{\ddot{U}_f^x}{g}\left(5-3\cos\left(2\left(\alpha-\left|\theta\right|\right)\right)\right)-3\operatorname{sgn}\left(\theta\right)\sin\left(2\left(\alpha-\left|\theta\right|\right)\right)+\frac{6\dot{\theta}^2}{p^2}\operatorname{sgn}\left(\theta\right)\sin\left(\alpha-\left|\theta\right|\right)}{5+3\cos\left(2\left(\alpha-\left|\theta\right|\right)\right)-\frac{3\ddot{U}_f^x}{g}\operatorname{sgn}\left(\theta\right)\sin\left(2\left(\alpha-\left|\theta\right|\right)\right)-\frac{6\dot{\theta}^2}{p^2}\cos\left(\alpha-\left|\theta\right|\right)} \right| \tag{A.29}$$

$$\mu_s \geq \left| \frac{\frac{\left|\ddot{U}_f^x\right|}{g}-\frac{3}{4}\cos\left(\alpha\right)\sin\left(\alpha\right)\left(\frac{\left|\ddot{U}_f^x\right|}{g\tan\left(\alpha\right)}-1\right)}{1+\frac{3}{4}\sin^2\left(\alpha\right)\left(\frac{\left|\ddot{U}_f^x\right|}{g\tan\left(\alpha\right)}-1\right)} \right| \tag{A.30}$$

Derivation of vertical reaction force on rocking block

Equation (A.31) can be attained by applying dynamic equilibrium to the rocking block in the vertical direction.

$$F_y = m\left(\ddot{\bar{y}} + \ddot{U}_f^y + g\right) \tag{A.31}$$

The vertical position of the center of mass with respect to the rocking toe is given in Equation (A.32) and can be twice differentiated to obtain Equation (A.33).

$$\bar{y} = R\cos\left(\alpha - |\theta|\right) \tag{A.32}$$

$$\ddot{\bar{y}} = R\,\mathrm{sgn}(\theta)\ddot{\theta}\sin\left(\alpha - |\theta|\right) - R\dot{\theta}^2\cos\left(\alpha - |\theta|\right) \tag{A.33}$$

Equation (A.33) can be subbed into Equation (A.31) to get the normal reaction force that acts on the rocking edge of the block as given in Equation (A.34).

$$F_y = m\left\{\mathrm{sgn}(\theta)R\ddot{\theta}\sin\left(\alpha - |\theta|\right) - R\dot{\theta}^2\cos\left(\alpha - |\theta|\right) + \ddot{U}_f^y + g\right\} \tag{A.34}$$

Appendix B

Member sizes

Table A-1. Fixed-base building member sizes

Story	Column	Girder	Braced Column	Braced Girder	Brace	Zipper Column
1	W14X68	W14X68	W14X233	W36X393	HSS12X12X5/8	W14X48
2	W14X68	W14X68	W14X233	W36X393	HSS10X10X5/8	W14X48
3	W14X48	W14X68	W14X68	W36X393	HSS9X9X5/8	W14X48
4	W14X48	W14X68	W14X68	W36X393	HSS7X7X5/8	W14X48

Table A-2. Base-isolated superstructure member sizes

Story	Column	Girder	Braced Column	Brace
1	W14X68	W14X68	W14X145	HSS12X12X5/8
2	W14X68	W14X68	W14X145	HSS10X10X5/8
3	W14X48	W14X68	W14X68	HSS10X10X5/8
4	W14X48	W14X68	W14X68	HSS10X10X5/8

Appendix C

Ground motions

Table A-1. Ground motions selected for time history analysis

#	Record	Earthquake	Station	Date	Magnitude
1	FP-1	Mammoth Lakes	Long Valley Dam UPRL	5/25/1980	6.0
2	FN-3	Cape Mendocino	Rio Dell Overpass FF	4/25/1992	7.2
3	FN-4	Imperial Valley	Delta	10/15/1979	6.4
4	FP-6	Imperial Valley	Calipatria Fire Sta.	10/15/1979	6.4
5	FP-8	Chi-Chi	NST	9/20/1999	7.3
6	FP-11	Spitak, Armenia	Gukasian	12/7/1988	6.8
7	FN-12	Loma Prieta	Gilroy Array #4	10/18/1989	6.9
8	FN-13	Chi-Chi	TCU-060	9/20/1999	7.3
9	FN-15	Loma Prieta	Fremont Emerson Crt.	10/18/1989	6.9
10	FN-16	Chalfant Valley	Zach Brothers Ranch	7/21/1986	6.4
11	FP-19	Imperial Valley	El Centro Array #4	10/15/1979	6.4
12	FP-21	Landers	Yermo Fire Station	6/28/1992	7.3
13	FP-23	San Fernanado	LA Hollywood Stor Lot	2/9/1971	6.5
14	FN-26	Chi-Chi	TCU-055	9/20/1999	7.3
15	FP-28	Imperial Valley	Brawley Airport	10/15/1979	6.4
16	FP-29	Chi-Chi	CHY088	9/20/1999	7.3
17	FP-32	Loma Prieta	Saratoga Aloha Ave.	10/18/1989	6.9
18	FP-35	Northridge	Sylmar,Jenson Slt Plt	1/17/1994	6.7
19	FP-37	Loma Prieta	Salinas John and Work	10/18/1989	6.9
20	FP-38	Loma Prieta	Coyote Lake Dam	10/18/1989	6.9

Table A-2. Peak responses of selected ground motions

#	Horiz. PGA (g)	Horiz. PGV (m/s)	Horiz. PGD (m)	Vert. PGA (g)	Vert. PGV (m/s)	Vert. PGD (m)	Scaling Factor
1	0.45	0.25	0.08	0.12	0.08	0.02	1.84
2	0.42	0.40	0.24	0.20	0.11	0.07	1.28
3	0.24	0.26	0.13	0.15	0.15	0.09	1.78
4	0.08	0.12	0.07	0.06	0.04	0.03	6.27
5	0.43	0.33	0.23	0.11	0.18	0.12	1.81
6	0.19	0.21	0.08	0.12	0.09	0.04	3.00
7	0.35	0.36	0.12	0.16	0.15	0.05	1.48
8	0.21	0.34	0.49	0.09	0.27	0.25	2.61
9	0.13	0.11	0.06	0.07	0.09	0.06	4.17
10	0.38	0.39	0.07	0.32	0.12	0.03	1.12
11	0.47	0.40	0.21	0.25	0.16	0.11	1.23
12	0.22	0.25	0.17	0.14	0.13	0.06	2.18
13	0.21	0.18	0.12	0.14	0.04	0.01	2.21
14	0.25	0.31	0.12	0.17	0.44	0.40	1.65
15	0.21	0.36	0.15	0.15	0.08	0.03	2.26
16	0.22	0.21	0.13	0.04	0.07	0.05	2.12
17	0.38	0.43	0.16	0.39	0.27	0.15	1.59
18	1.07	0.64	0.21	0.82	0.32	0.15	0.54
19	0.09	0.13	0.08	0.10	0.07	0.02	4.96
20	0.19	0.23	0.14	0.09	0.10	0.04	2.28